Università degli Studi di Ferrara

DOTTORATO DI RICERCA IN
"SCIENZE DELL'INGEGNERIA"

CICLO XXIX

COORDINATORE Prof. Stefano Trillo

Numerical Evaluation of Adhesively Bonded Repair in Composite Structures

Settore Scientifico Disciplinare ING-IND/14

Dottorando
Dott. Barile Giacomo

_____
(firma)

Tutore
Prof. Tovo Roberto

_____
(firma)

CoTutore
Prof. Francesco Mollica

_____
(firma)

Anni 2014/2016

“You are never too old to set another goal

or to dream a new dream.”

C. S. Lewis

ACKNOWLEDGEMENTS

It has been a pleasure and an honour to be a PhD Student of Engineering Department in Ferrara.

First of all, my sincere gratitude goes to my CoTutor Ing. Francesco Mollica and to my guide over the three years, Ing. Valentina Mazzanti, who were very patient and always helped and attended me in all my needs, I also want to thank the members of the Engineering Department of the University of Ferrara as a whole, for providing me with all the necessary facilities for the research.

I would like to thanks Ing. Enrico Troiani of the Aerospace Engineering of the University of Bologna, without which my PhD research was not made possible, for the support of my PhD study and relative research.

Furthermore, my deepest thanks go to my wife, Eliana, who has been so patient and supported me in times of distress, favouring my life choices.

But above all, I would like to dedicate this thesis to my parents, wherever they are, to making me the man I am today.

Thanks with all my heart all of you!

Ferrara, 2017 Giacomo Barile

TABLE OF CONTENTS

Page

INTRODUCTION

In the normal life of an aircraft, damages due to accident (unintended contact between an aircraft and any other aircraft, vehicle, ground equipment or ground object, bird strikes, etc.…) are events that occur commonly.

Although composites have been used for decades in aircraft structures, the use of composite in large primary structures is a new phenomenon. The extensive and increasing application of composite primary structures in the aviation and non-aviation sector like automotive or aerospace, now comes close to 50% for new aircraft structures such as the Boeing 787 (Fig. 1, 4) and Airbus 350 (Fig. 2, 3) or the newest VEGA launcher (Fig. 5). These composite structures also require a repair solution. For minor damage that does not result in complete replacement of the structure, a patched repair is typically applied. The current solution allowed under the regulations is a bolted or riveted repair. These repairs have shown their usefulness on metal aircraft and can also be applied to composite aircraft. Unfortunately, the bolted or riveted repair is not ideal for a composite structure as holes and composites together is not a happy marriage. This is due to the strain sensitivity of composites and to the fact that manufacturing acceptable holes in a composite is an extremely difficult job.

Fig. 1: Boeing 787 [1]

A bonded repair overcomes both problems: there is no need to make holes and therefore the strain concentration is limited. In addition, a bonded repair will allow a higher smoothness

(roughness) of the repaired patch (several microns) and therefore a laminar flow at the wing can be maintained (aerodynamic flushness) leading to a higher fuel efficiency. For these reasons, a bonded repair is preferred.

Fig. 2: Airbus 350 [2]

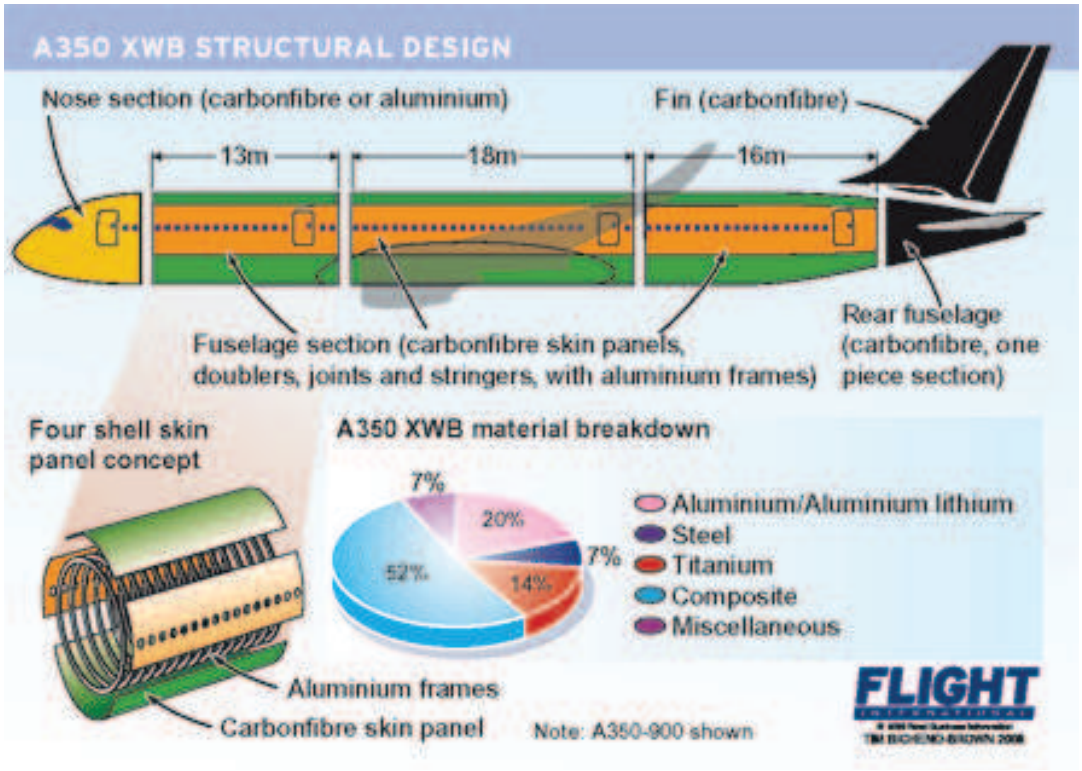

Fig. 3: A350 XWB Structural Design [3]

This will ask new repair knowledge, procedures, technologies and policies to adapt traditional repair methods. Bolted repair technology, as used for metallic structures, is currently the only approved and certified repair technique for aerospace composite structures

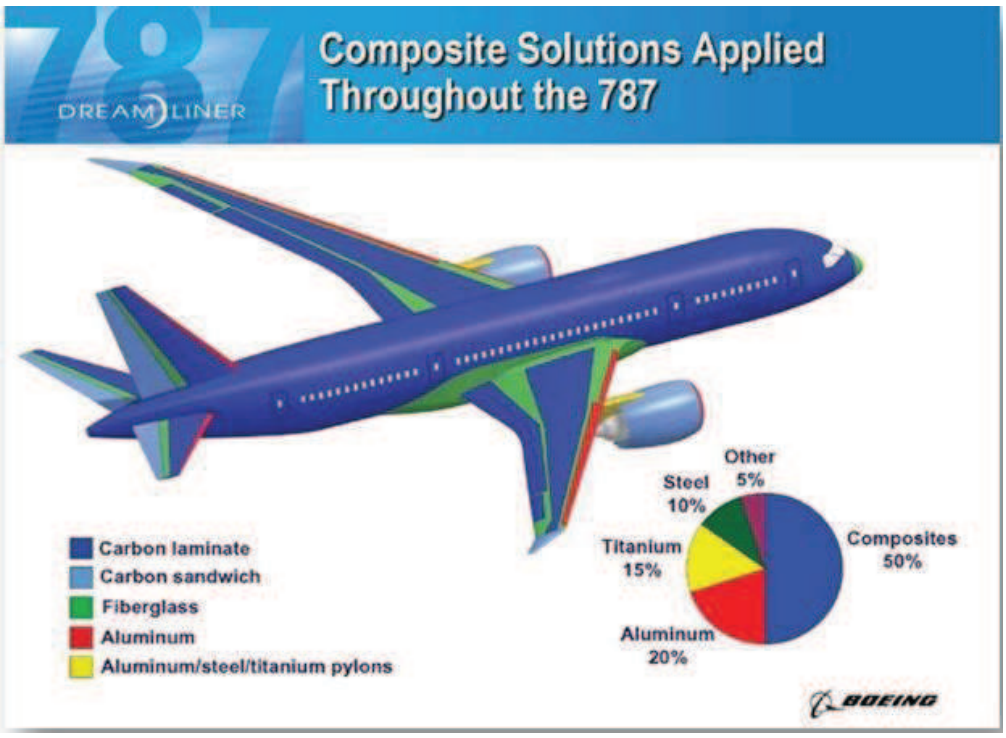

Fig. 4: B787 Dreamliner composite solutions [8]

(Regulation AMC 20-29/AC 20-107B: "Composite Aircraft Structure") [4, 5]. However, for large repairs and the refurbishment of a complete primary structure, bonded repair is preferred due to the obvious advantages in weight (reduction), improved sustainability in terms of fuel efficiency due to reduced drag, no disruption of structural integrity by hole drilling, better load transfer capability and the reduction of waste. In instances where bolted repair cannot be applied today, a bonded repair can even prevent the replacement of a part. Further in the future the validation of bonded repair will also allow further advances in aircraft design by reducing design restrictions. There are significant constraints related to the introduction of bonded repairs in primary structures. A "damage tolerance" validation process must be supported by advanced inspection techniques that can characterize the repair bond line. Also a much better understanding of the scientific and technical elements of a composite repair design is needed to provide the proper substantiation for later EASA certification [6].

The main challenges of this work are:

1. a better understanding of the physical behaviour at the bond-line;
2. correlate a perfect bond with a weak bond by means of numerical simulations;
3. validate a model of an innovative bonded repair.

The proposed thesis is based on the philosophy that the regulatory agencies such as EASA will take 20 years or more to develop sufficient validated data to allow full certification of

bonded repairs of primary structures. Of course some (test) data is already available, but the use of this data is predominately the prerogative of the OEM‟s (Original Equipment Manufacturer) such as Boeing and Airbus, and very much related to the unique material selection by these OEM‟s. This data is however not accessible to the broader aviation community including EASA, while at the same time MRO (Maintenance, Repair & Overhaul) organizations need to prepare themselves for the handling of large composite parts and structures such as in the A350 or B787 in the near future. Of course one could fall back on the existing approved bolted and riveted repair method, but as mentioned above, this is not the preferred technical and performance solution.

Fig. 5: Vega Launcher [7]

The development work wants to reduce the anticipated 20 years' validation period and providing a transparent certification process and repair technology available and accessible

to all stakeholders in the aviation industry. A study conducted by Delft University of Technology [9], NLR (Nationaal Lucht en Ruimtevaart Laboratorium) [10] and Sergem Engineering [11] demonstrates that a significant amount of scientific and technical data was lacking and, consequently, it was estimated that the (R&D) state-of-the-art for a fully industrialized bonded repair technology (for primary structures) was only at TRL (Technology Readiness Level) stage 2.

EASA documentation indicated that an eventual certification of a bonded repair technology for primary structures could only materialize by a combination of:

1. Improved repair technologies;
2. Better understanding of the physical behaviour at the bond-line;
3. New inspection technologies;
4. "Damage tolerance" validation;
5. Human factors and training/educational programs;
6. Approval by EASA/FAA authorities [6, 8].

Obviously, for a matter of time, this work analyses only the second step and is organized as follow:

- in Chapter 1 the composite primary structures of modern aircraft as Airbus 350 WXB will be described, with emphasis on materials, technologies and material properties used to build these structures;
- Chapter 2 introduces some mathematical and physical concepts beyond the CFRP (Carbon Fiber Reinforced Polymer) discussed in Chapter 1;
- in Chapter 3 a brief description of the FEM software – ABAQUS® 6.13 will be presented;
- in Chapter 4 the CZM technique (Cohesive Zone Model) will be discussed;
- for the comprehension of all above cited, many applications and simulations are made to fully understand Abaqus® and its parameters; Chapter 5 and 6 are a compendium of all the achieved benchmarking, from Traction and Bending Laminate Tests to Some Applications of the CZM;
- Chapter 7 introduces an innovative model of a bonded repair, implemented with Abaqus/standard and results will be analyzed and compared with literature experimental data;
- Chapter 8 discusses some concluding remarks and proposal for future works.

CHAP. 1: CARBON FIBER REINFORCED POLYMER

1.1 Carbon-fiber-reinforced polymer

Carbon-fiber-reinforced polymer (CFRP) is a very strong and light fiber-reinforced polymer that contains carbon fiber.

Carbon-fiber-reinforced polymers are composite materials. They consist of two elements: a matrix and reinforcement. In CFRPs, the reinforcement is the carbon fiber and the matrix is usually a polymer resin. The material properties depend on these two elements.

In carbon-fiber-reinforced polymers, the polymer is most often epoxy, but other polymers, such as polyester, vinyl ester or nylon, are sometimes used to bind the reinforcements together. The composite may contain other fibers such as Kevlar, aluminum, or glass fibers as well as carbon fiber, which provides the strength. The reinforcement gives CFRP its strength and rigidity.

The properties of CFRPs depend on the layouts of the carbon fiber and the proportion of the carbon fibers relative to the polymer. The properties of the final CFRPs product can also be affected by the type of additives introduced to the binding matrix (the resin). The most frequent additive is silica, but other additives such as rubber and carbon nanotubes can be used.

Carbon-fiber-reinforced polymer has the best strength-to-weight ratio of all construction materials (Table 1.1). It is an improvement on glass-fiber-reinforced plastic, although much more expensive. Even though they can be expensive to produce, CFRPs are commonly used wherever high strength-to-weight ratio and rigidity are required, such as:

- Aerospace
- Automotive
- Civil engineering
- Sports goods
- An increasing number of other consumer and technical applications

Despite its high initial strength-to-weight ratio, one structural limitation of CFRP is its lack of a fatigue endurance limit. As a result, when utilizing CFRPs for critical cyclic-loading applications, engineers may need to employ considerable strength safety margins to provide suitable component reliability over a sufficiently long service life [12].

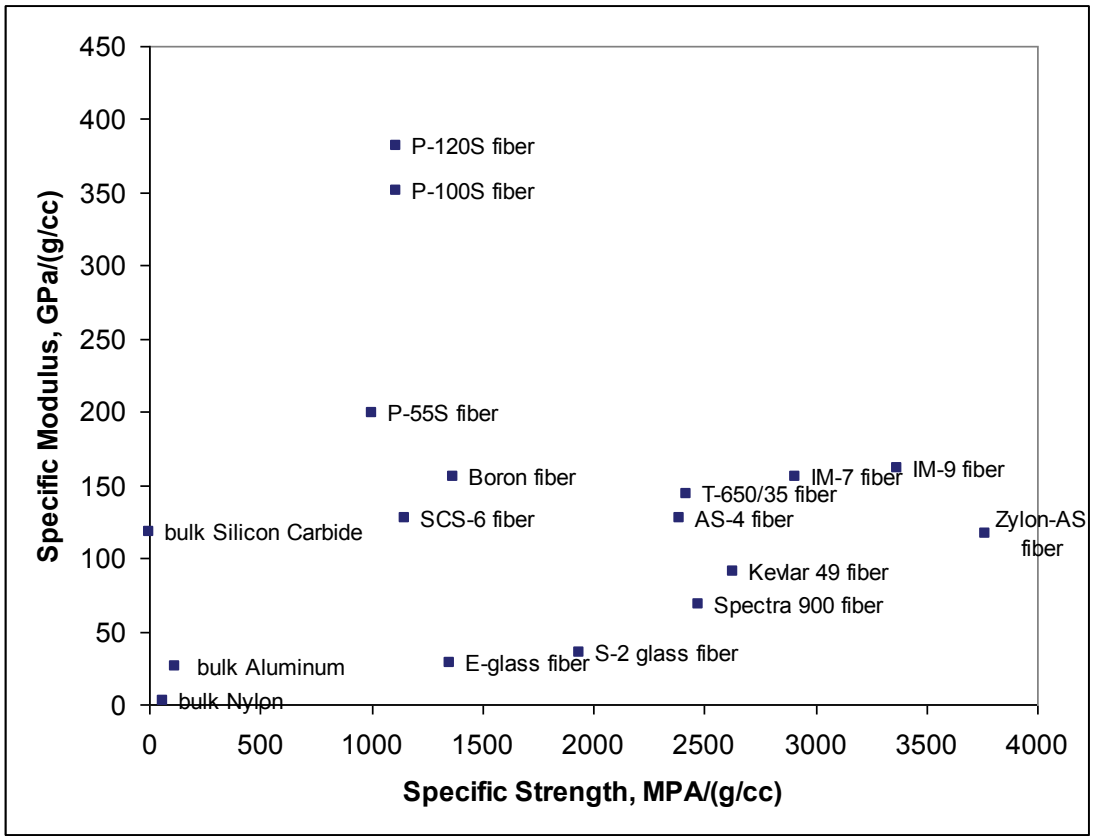

Table 1.1: Selected properties of bulk and fibrous materials [Gibson, 2012]

1.2 Aircraft Structures

When designing an aircraft, we have to find the optimal proportion of the weight of the vehicle and payload. It needs to be strong and stiff enough to withstand the exceptional circumstances in which it has to operate. Durability is an important factor. In addition, if a part fails, it does not necessarily result in failure of the whole aircraft.

The main sections of an aircraft, the fuselage, tail and wing, determine its external shape. The loadbearing members of these main sections, those subjected to major forces, are called the airframe.

The airframe is what remains if all equipment and systems are stripped away. Old aircrafts had skin made from impregnated linen that could hardly transmit any force at all. In most modern aircrafts, the skin plays an important role in carrying loads. Sheet metals can usually only support tension. But if the sheet is folded, it suddenly does have the ability to carry compressive loads. Stiffeners are used for that. A section of skin, combined with stiffeners, called stringers, is termed a thin-walled structure.

A very good way of using sheet metal skin is in a thin-walled cylinder, called a monocoque structure.

A cylinder with holes, for doors and such, is called a semi-monocoque structure.

An extruded stiffener is manufactured by squeezing hot, viscous material through an opening of a certain shape. It can usually be recognized by the fact that the thickness is not consistent, especially in the corners. This is relatively expensive, compared to stiffeners made from sheet metal. From sheet metal it is not possible to make complicated stiffeners. Thin sheet metal can be rolled or drawn.

Usually stiffeners are attached to the skin. In an integral structure, the skin and stiffeners have been manufactured from one solid block of material. It is also possible to make some kind of a sandwich structure, in which the skin has a high stiffness due to its spatial structure.

1.3 Primary aircraft structures: a definition

A Primary aircraft structure is a critical load-bearing structure on an aircraft. If this structure is severely damaged, the aircraft cannot fly anymore.

Secondary aircraft structures are structural elements mainly to provide enhanced aerodynamics. Fairings, for instance, are found where the wing meets the body or at various locations on the leading or trailing edge of the wing. In fig. 1.1 and 1.2, we can see primary structures – fuselage, wings, tail, elevators – and some secondary structures – spoilers, ailerons, radome, winglets, flaps, on an A350XWB and on a B787 respectively.

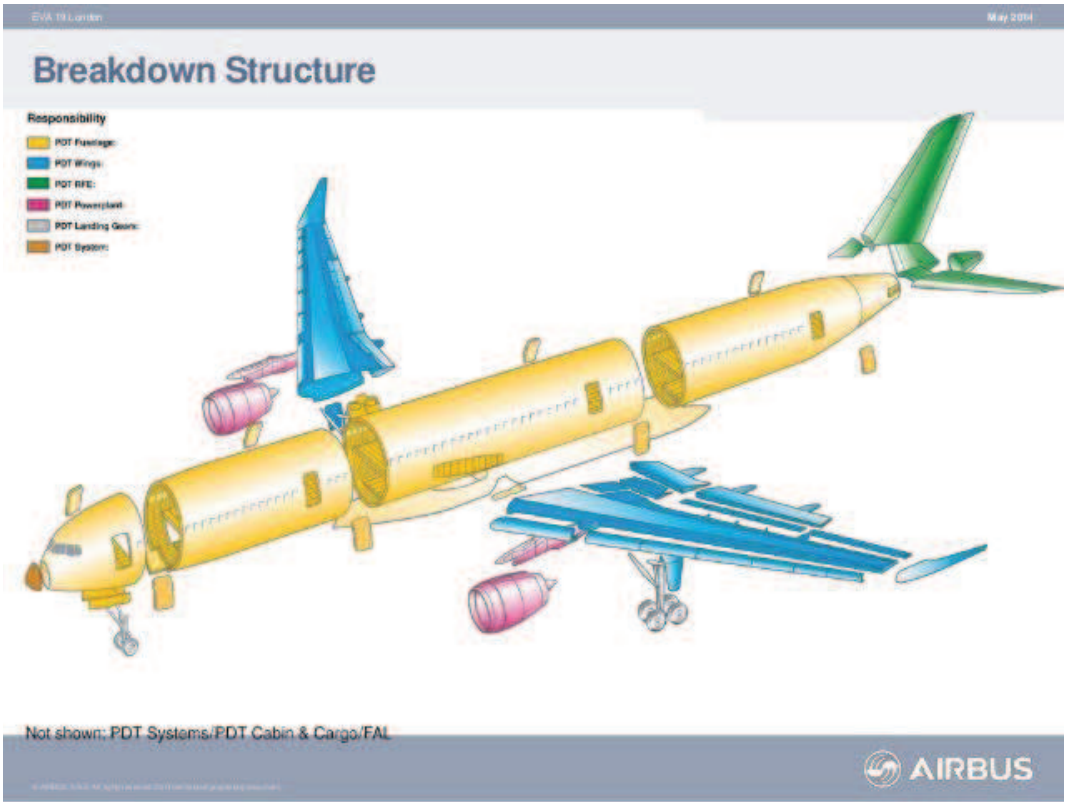

Fig. 1.1: Primary and secondary aircraft structures on A350 XWB [13].

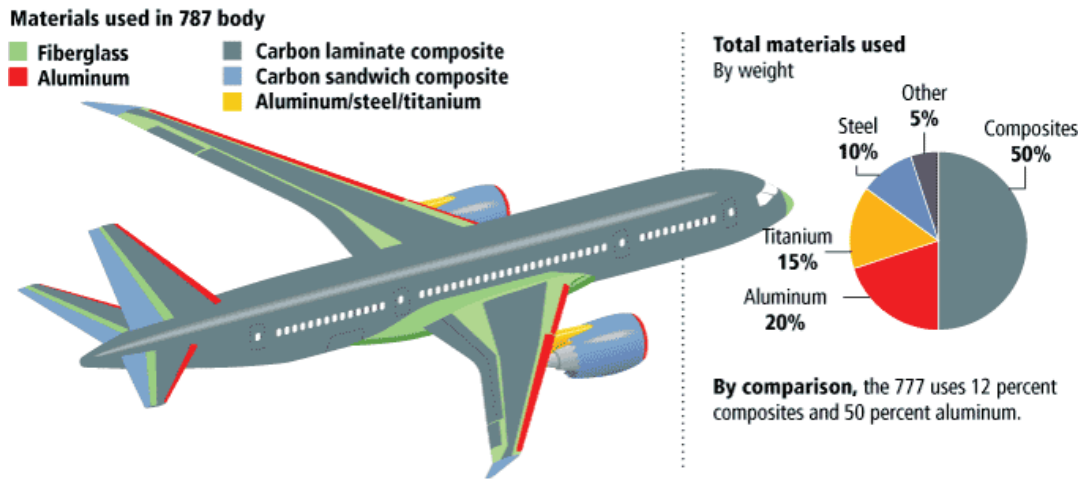

Fig. 1.2: Primary and secondary aircraft structures on a B787 [14].

1.4 Certification of bonded primary aircraft structures

Composites have flown on commercial aircraft secondary structures for more than 30 years, but only recently, they conquered the fuselage, wingbox and wings, most notably on the Boeing Co.'s (Chicago, Ill.) 787 Dreamliner and the A350 XWB from Airbus (Toulouse, France). These carbon-fiber-reinforced plastic (CFRP) structures, however, still require assembly with thousands of mechanical fasteners. Why? Because it is the easiest and least expensive way to meet current certification requirements, which mandate proof that each and every adhesively bonded joint will not separate and because of structural failure should it reach its critical design load. However, many in the industry argue that the full cost and weight savings of composites cannot be realized until bonded joints can be certified without fasteners.

The development of technologies to address this need has steadily progressed, from programs in the late 1990's such as the U.S. Department of Defense (DoD) Composites Affordability Initiative (CAI) [16] to more recent initiatives, including the European Union (EU)-funded Boltless Assembling Of Primary Aerospace Composite Structures (BOPACS) project [17]. Current efforts are made to build a certification regime for bonded primary structures on aircraft. Boeing [1], Airbus [2] and Lockheed Martin Aeronautics [Palmdale, Calif.] [18] have mounted independent efforts toward that end. Their research offers the hope of building reliability into the bonding process, and of gauging final bond strength via a coordinated certification system that includes design, process control and quality assurance (QA).

1.5 Why bolt and why bond?

Fasteners are used in composite primary structures today due to certification requirements. These were outlined in a 2013 SAMPE (May 6-9, Long Beach, Calif.) presentation titled "Efficient Certification of Bonded Primary Structures," by Kay Blohowiak, a technical fellow working in Composite Bonding Processes for Boeing Research & Technology (Seattle, Wash.), and her co-authors. For composite structures on commercial aircraft, the most often cited of these documents is AC 20-107B "Composite Aircraft Structure" [4, 5] issued jointly by the Federal Aviation Administration (FAA, Washington D.C.) [8] and the European Aviation Safety Agency (EASA, Cologne, Germany) [6]. It describes three options for certifying damage tolerance of structures with bonded joints. (These options are listed, with explanatory comments, in the table at right) [Blohowiak, K. et al., 2013].

Blohowiak et al., noted that, to date, no method of nondestructive testing/inspection (NDI/NDT) has demonstrated the capability to quantify the long-term strength and durability of bonded joints. They also noted that proof testing of each critical bonded joint on every new aircraft (application of the limit design load to verify that the bond does not fail) would be prohibitively expensive. Today, that effectively eliminates from consideration two of the three. That leaves one option: "prevention by design features." Historically, mechanical fasteners through the bondline thickness (a/k/a "chicken rivets") have been the design feature of choice.

However, Blohowiak and her co-authors point out that bonded joints without fasteners offer advantages beyond eliminating the purchase and installation of hardware. Without fastener holes, component thickness can be reduced, more efficient load paths are possible and thousands of stress concentrations, which can become points of origin for fatigue and related deterioration, are removed. And their removal can lead to significant additional savings in weight and greater airframe structure optimization. As their SAMPE paper asserts, bonded structures are, indeed, one path "to improve efficiency and reduce assembly cost in future advanced composite aircraft." It seems plausible that they may also improve composites' competitiveness vs. future metals technologies, such as high-strength aluminum alloys [15].

1.6 Materials used in Primary aircraft structures

Hexcel's HexPly® M21E [19] epoxy prepreg made with HexTow® IMA [20] intermediate carbon fiber is used to manufacture the A350 XWB's fuselage panels, keel beam, the entire wing (covers, spars and center wing box) and empennage (Figure 1.2).

HexTow IMA [20] provides superior mechanical performance including very high tensile strength (6607 MPa) and tensile modulus (297 GPa).

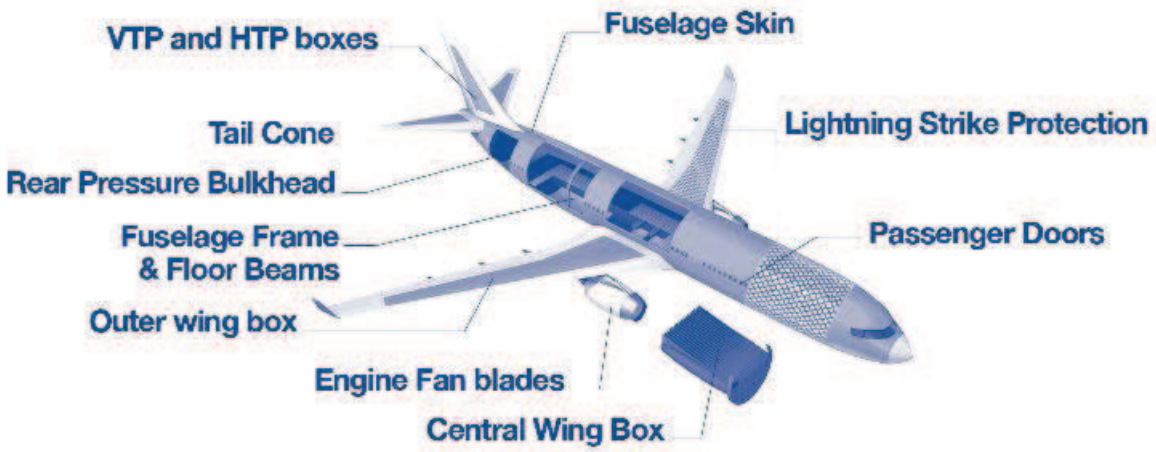

Fig. 1.3: Primary structures on the A350 XWB [23].

Hexcel has a long history of supplying structural prepregs to the aerospace industry. Its HexPly M21E and 8552 systems are widely used at Airbus and are employed on the A380 and A400M programs. Hexcel chemists developed HexPly M21E [19] epoxy resin to provide enhanced toughness and durability, to ensure the properties of the fiber are fully optimized in the cured prepreg laminates.

HexPly® M21E is a high performance, very tough epoxy matrix for use in primary aerospace structures. It exhibits excellent damage tolerance, especially at higher energy impacts. HexPly® M21E is a toughened epoxy resin system supplied with unidirectional or woven carbon or glass fibers. HexPly® M21was developed as a controlled flow system to operate up to 121°C.

Some of its benefits and features are:

- Excellent toughness, in particular at high energy impact
- High residual compression strength after impact
- Effective translation of fiber properties, especially with intermediate modulus carbon fiber
- Good hot-wet properties up to 121°C
- Low exothermal behaviour allowing simple cures of thick structures up to 48 mm
- Good tack life (the time, at room temperature, during which prepreg retains enough tack for easy component lay-up)

Some typical cured Unidirectional Prepreg properties [22]:

	U.S. Units	SI Units
Tensile Strength	442 ksi	3050 MPa
Tensile Modulus	25.8 msi	178 Gpa
Compressive Strength	218 ksi	1500 MPa
Compressive Modulus	21.2 msi	146 GPa
Fiber Density	111.1 lbs. /ft^3	1.78 g/cm^3
Resin Density	79.9 lbs. /ft^3	1.28 g/cm^3
Theoretical Calculated Laminate Density	98.6 lbs. /ft^3	1.58 g/cm^3

HexTow® IMA carbon fiber is a continuous, high performance, intermediate modulus, PAN based fiber available in 12,000 (12K) filament count tows. This fiber has been surface treated and can be sized to improve its interlaminar shear properties, handling characteristics, and structural properties. It is suggested for use in prepregging.

The unique properties of HexTow® IMA fiber, such as higher tensile strength and modulus, as well as good shear strength, allow structural designers to achieve both higher safety margins for both stiffness and strength critical applications.

Here are some typical fiber properties:

	U.S. Units	SI Units
Tensile Strength (12K)	880 Ksi	6,067 MPa
Tensile Modulus (Chord 6000-1000)	43.1 Msi	297 GPa
Ultimate Elongation at Failure (12K)	1.8%	1.8%
Density	0.0648 lb. /in	3 1.79 g/cm3
Weight/Length (12K)	24.9 x 10-6 lb. /in	0.445 g/m
Approximate Yield (12K)	3,345 ft/lb.	2.25 m/g
Tow Cross-Sectional Area (12K)	3.83 x 10-4 in	2 0.25 mm2
Filament Diameter	0.202 mil.	5.1 microns
Carbon Content	95.0%	95.0%
Twist	Never Twisted	Never Twisted

The prepreg is supplied as unidirectional (UD) tape, which can be very finely slit for automated fiber placement (AFP) and automated tape laying (ATL) processes. In addition to the primary structure, Hexcel is supplying a number of other HexPly prepregs for other structures on the A350 XWB (Fig. 1.3). HexPly 8552 woven and UD prepregs, HexPly M65 woven BMI prepreg and HexPly 914/ASC woven prepreg are used in the engines and

nacelles along with Hexcel's engineered core and Acoustic-Cap® broadband noise reducing honeycomb. The belly fairing is made from HexPly M26T and F593 woven carbon prepregs, and HexPly M59XF expanded copper foil prepreg. HexWeb® Engineered Core packages are used extensively in the wing leading and trailing edges and ailerons.

Other Hexcel products used on the aircraft include HexFlow® RTM 6 infusion resin and HexForce® engineered reinforcements for out of autoclave structures, Redux® adhesives and lightning strike protection solutions. [24].

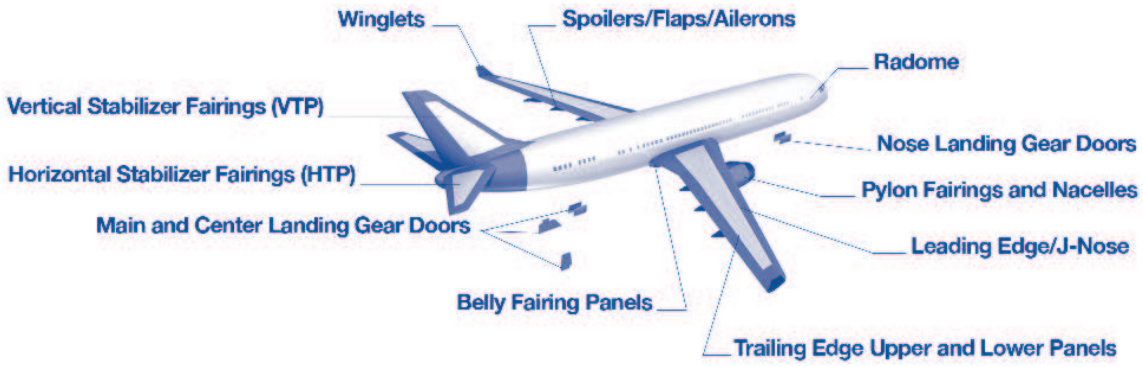

Fig. 1.3: Secondary structures on the A350 XWB [23].

1.7 Primary aircraft structures technologies

Prepreg can be processed in different ways. Some prepreg processing technologies are:

- **Hand Lay-Up**: Manual/non-automated lay-up process of prepreg. Available for all types of fiber reinforced prepregs (glass, carbon, Kevlar) with unidirectional and woven reinforcements and at various widths. Prepreg supplied with polythene and/or paper protectors. Suitable for complex shaped parts, monolithic and sandwich panels, low to medium volume production.
- **Automatic Tape Laying (ATL)**: Automated deposition of unidirectional prepreg tapes and for some other reinforcement materials e.g. glass woven prepregs, wet peel plies and metallic mesh prepregs. Typically, available at 150mm (5.9”) or 300mm (11.8”) widths. Other widths can be considered, dependent on ATL machine design (Fig. 1.4). Prepreg is supplied with a single double-sided release paper. Suitable for large, low to medium curvature monolithic parts. The A350 wing skin, e.g., is tape layed in one piece on a massive tool (Fig. 1.6), using an automated tape layer (ATL) built by MTorres [Torres de Elorz, Spain] [25].

- **Automatic Fiber Placement (AFP)**: Automated deposition of narrow unidirectional prepreg tapes. Typically, available at 3.175mm (1/8”), 6.35mm (1/4”) or 12.7mm (1/2”)

Fig. 1.4: ATL Machine (Photo courtesy of MAG)

width and various bobbin sizes. Prepreg is supplied with a single polythene protector. Suitable for medium to large complex curvature monolithic parts (Fig. 1.5, 1.6).

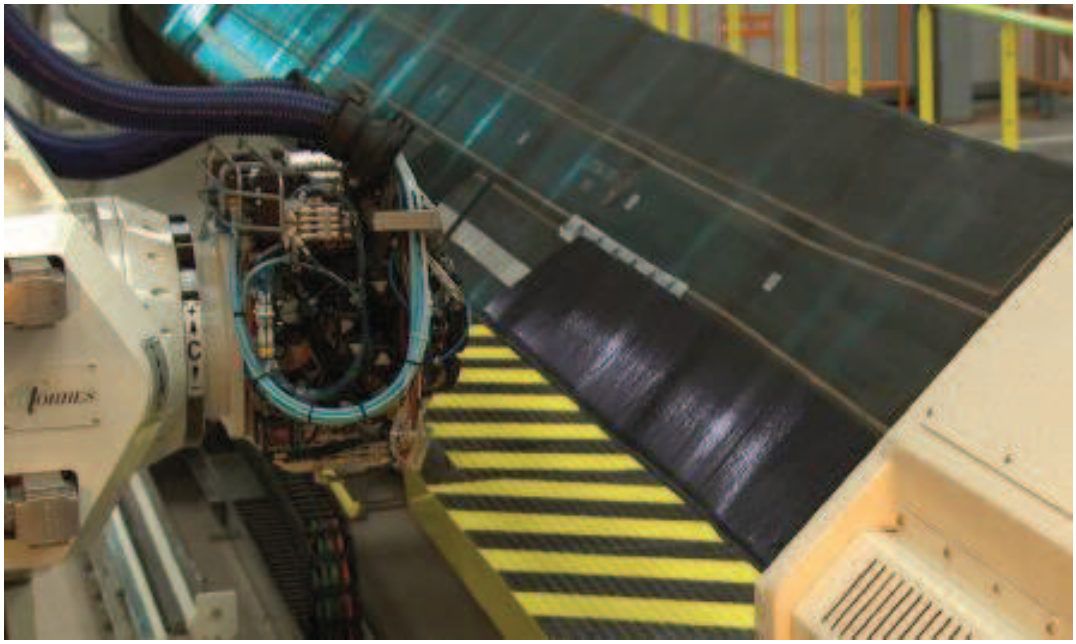

Fig. 1.5: AFP Machine (Photo courtesy of GKN)

1.8 Composite tests

In Fig. 1.7, each group shows the general specimen test configuration and formula. These tests are made on monolithic structures [21].

Fig. 1.6: Manufacture of the A350 XWB lower wing shells (Picture© Airbus S.A.S.)

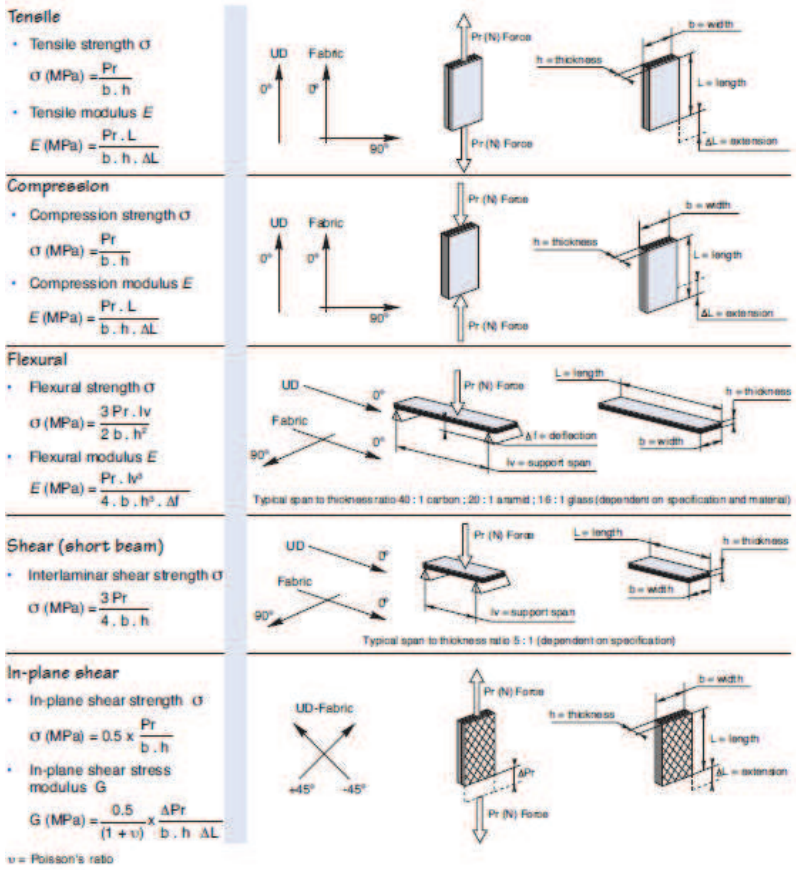

Fig. 1.7: Mechanical tests on monolithic structures [21].

CHAP. 2: MATHEMATICAL AND PHYSICAL CONCEPTS BEYOND THE CFRP [Gibson, 2012]

2.1 Introduction

The lamina is the basic building block of a composite structure. Its configuration consists in one or more unidirectional fiber-reinforced polymer, as seen in chapter one, eventually disposed in different directions. Here we consider the unidirectionally reinforced or unidirectional lamina with an arrangement of parallel, continuous fiber composite laminate as the best starting point. We will discuss the stress-strain relationships for the unidirectional lamina, which is the basis not only for the continuous fiber composite laminate.

Due to heterogeneity, a composite material obviously changes its properties from point to point. If we analyze the stress-strain relationships at a point in the fiber material, of course we will find different properties at a point in the matrix. However, from a macro-mechanical point of view, the stress-strain relationships of the lamina can be expressed in terms of average stresses and strains, as effective properties of an equivalent homogeneous material.

Further, anisotropy is another complication for the properties of the composite. In other words, whilst metallic materials are isotropic since their properties are essentially independent from orientation, the properties of anisotropic materials are orientation-dependent. Fortunately, we can find in each type of composite some materials property symmetries, in order to simplify the general stress-strain relationships. This is the case of the unidirectional lamina, called orthotropic material for this reason.

In this chapter, the symmetries associated with various types of composite laminae and the resulting stress-strain relationships are discussed.

2.2 Stress-strain relationships

As shown in fig. 2.1, at a point in a material, a general 3D state of stress can be described by nine stress component σ_{ij} (where i, j = 1, 2, 3).

As mentioned in [Gibson], here we use the conventional subscript notation, where when $i = j$, the stress component σ_{ij} is a normal stress, and when $i \neq j$, the stress component is a shear stress. The first number of the subscript is referred to the direction of the outward normal to the face on which the stress component acts, and the second subscript number refers to the direction in which the stress component itself acts.

For every stress component there is a strain component ε_{ij} describing the deformation at a point. Similarly to the stress component subscript notation, when $i = j$, the deformation is normal to the x_i direction – extension or contraction per unit length along the x_i direction –

and when $i \neq j$, the component is a shear strain describing the distortional deformations associated with x_i and x_j directions.

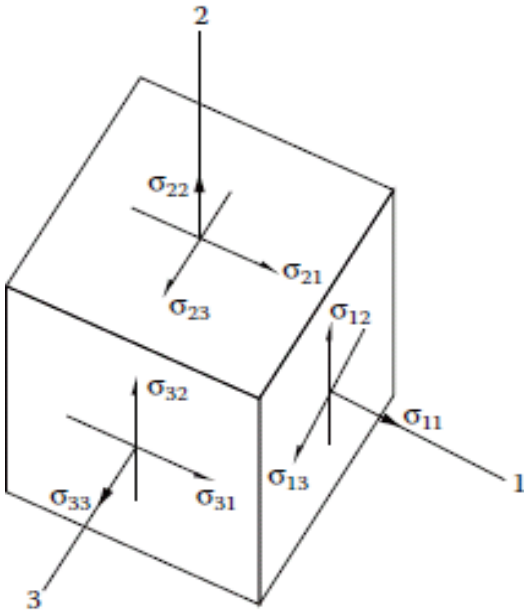

Fig. 2.1: 3D state of stress

It is very important here to note that the "tensor" strain ε_{ij} is different from the "engineering" strain γ_{ij}. As we can see in Fig. 2.2, the relationship between the "tensor" strain ε_{ij} and the "engineering" strain γ_{ij} is a factor ½, that is $\varepsilon_{ij} = \gamma_{ij}/2$. In other words, the tensor shear strain ε_{ij} describes the amount of the rotation whilst the engineering shear strain γ_{ij} the total distortional change in the angle between lines originally parallel to the x_i and x_j axes.

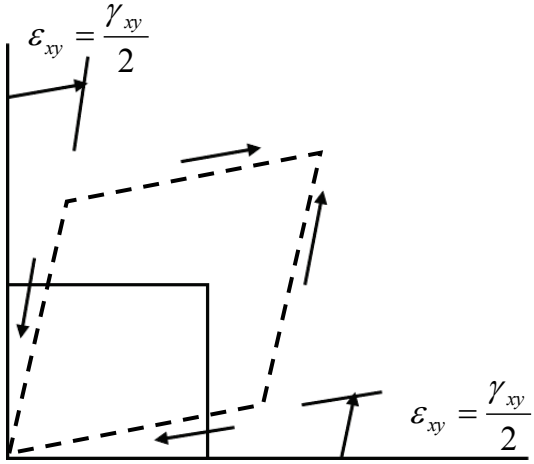

Fig. 2.2: Geometric interpretation of engineering shear strain and tensor shear strain.

The most general stress-strain relationship at a point in an elastic material is an equation of the form:

$$\sigma_{ij} = f_{ij}(\varepsilon_{11}, \varepsilon_{12,}\varepsilon_{12}\varepsilon_{13}, \varepsilon_{21}, \varepsilon_{22}, \varepsilon_{23}, \varepsilon_{31}, \varepsilon_{32}, \varepsilon_{33}) \tag{2.1}$$

where the functions $\boldsymbol{f_{ij}}$ may be nonlinear. At a point in the material, we can write the most general stress-strain relationships by equations 2.2:

$$\begin{Bmatrix} \boldsymbol{\sigma_{11}} \\ \boldsymbol{\sigma_{22}} \\ \boldsymbol{\sigma_{33}} \\ \boldsymbol{\sigma_{23}} \\ \boldsymbol{\sigma_{31}} \\ \boldsymbol{\sigma_{12}} \\ \boldsymbol{\sigma_{32}} \\ \boldsymbol{\sigma_{13}} \\ \boldsymbol{\sigma_{21}} \end{Bmatrix} = \begin{bmatrix} C_{1111}C_{1122}C_{1133}C_{1123}C_{1131}C_{1112} \vdots C_{1132}C_{1113}C_{1121} \\ C_{2211}C_{2222}C_{2233}C_{2223}C_{2231}C_{2212} \vdots C_{2232}C_{2213}C_{2221} \\ C_{3311}C_{3322}C_{3333}C_{3323}C_{3331}C_{3312} \vdots C_{3332}C_{3313}C_{3321} \\ C_{2311}C_{2322}C_{2333}C_{2323}C_{2331}C_{2312} \vdots C_{2332}C_{2313}C_{2321} \\ C_{3111}C_{3122}C_{3133}C_{3123}C_{3131}C_{3112} \vdots C_{3132}C_{3113}C_{3121} \\ C_{1211}C_{1222}C_{1233}C_{1223}C_{1231}C_{1212} \vdots C_{1232}C_{1213}C_{1221} \\ \cdots \quad \cdots \quad \cdots \quad \cdots \quad \cdots \quad \cdots \vdots \cdots \quad \cdots \quad \cdots \\ C_{3211}C_{3222}C_{3233}C_{3223}C_{3231}C_{3212} \vdots C_{3232}C_{3213}C_{3221} \\ C_{1311}C_{1322}C_{1333}C_{1323}C_{1331}C_{1312} \vdots C_{1332}C_{1313}C_{1321} \\ C_{2111}C_{2122}C_{2133}C_{2123}C_{2131}C_{2112} \vdots C_{2132}C_{2113}C_{2121} \end{bmatrix} \begin{Bmatrix} \boldsymbol{\varepsilon_{11}} \\ \boldsymbol{\varepsilon_{22}} \\ \boldsymbol{\varepsilon_{33}} \\ \boldsymbol{\varepsilon_{23}} \\ \boldsymbol{\varepsilon_{31}} \\ \boldsymbol{\varepsilon_{12}} \\ \boldsymbol{\varepsilon_{32}} \\ \boldsymbol{\varepsilon_{13}} \\ \boldsymbol{\varepsilon_{21}} \end{Bmatrix}$$

(2.2)

or written in a contracted form:

$$\{\boldsymbol{\sigma}\} = [\boldsymbol{C}]\{\boldsymbol{\varepsilon}\} \tag{2.3}$$

where [C] is an 81 (9x9) components matrix named stiffnesses matrix or elastic constants matrix or moduli constants matrix. If no restrictions are made on the elastic constants, the material is called anisotropic, and the equations (2.2) are referred to as the Hooke's law for anisotropic materials. Fortunately, we do not have to deal with these equations, because of considerable simplification due to symmetry conditions.

The first and obviously simplification, as cited in all materials book, is the symmetry of both stresses and strains, i.e. $\sigma_{ij} = \sigma_{ji}$ and $\varepsilon_{ij} = \varepsilon_{ji}$. Consequently, the number of independent stress or strain component become six. For the elastic constants, we have:

$$\mathrm{C}_{ijkl} = \mathrm{C}_{jikl} \; and \; \mathrm{C}_{ijkl} = \mathrm{C}_{ijlk}$$

where *i, j, k, l* = 1, 2, 3. Now the elastic constants reduce to 36.
To simplify also the subscripts notation, up to now we consider:

Stresses		**Strains**	
Tensor Notation	Contracted Notation	Tensor Notation	Contracted Notation
σ_{11}	σ_1	ε_{11}	ε_1
σ_{22}	σ_2	ε_{22}	ε_2
σ_{33}	σ_3	ε_{33}	ε_3
$\sigma_{23}=\sigma_{32}$	σ_4	$2\varepsilon_{23}=2\varepsilon_{32}=\gamma_{23}=\gamma_{32}$	ε_4
$\sigma_{13}=\sigma_{31}$	σ_5	$2\varepsilon_{13}=2\varepsilon_{31}=\gamma_{13}=\gamma_{31}$	ε_5
$\sigma_{12}=\sigma_{21}$	σ_6	$2\varepsilon_{12}=2\varepsilon_{21}=\gamma_{12}=\gamma_{21}$	ε_6

Now the generalized Hooke's law can be written:

$$\sigma_i = C_{ij}\varepsilon_j \qquad i,j = 1,2,\dots\dots,6$$

Alternatively, we can relate strains to stresses inverting Hooke's law:

$$\varepsilon_i = S_{ij}\sigma_j \qquad i,j = 1,2,\dots\dots,6$$

where [S] is the compliance matrix, inverse of the stiffness matrix ($[S]=[C]^{-1}$).
It is important to note that the relationships considered until now are valid at a point in the material, i.e. stresses, strains and elastic moduli change as we move from point to point in the composite material, due to its inhomogeneity (matrix mechanical properties are quite different from those of the fiber). In order to analyse the macromechanical behaviour of the composite, we can consider averaged stresses and strains related by an effective moduli of an equivalent homogeneous material. We have only to take the characteristic length dimension, *L*, of the material larger than the characteristic length dimension, *d,* of the

inhomogeneity scale (e.g. *d* could be the diameter of the fiber, and *L* the characteristic lamina dimension). Figure 2.3 shows the concept explained.

If we define the average stresses, $\overline{\sigma_i}$, and the average strains, $\overline{\varepsilon_i}$, (i = 1, 2, 3, …,6), over a volume V, characterized by the dimension L, so that:

$$\overline{\sigma_i} = \text{average stress} = \frac{\int_v \sigma_i dv}{\int_v dv} \qquad \overline{\varepsilon_i} = \text{average strain} = \frac{\int_v \varepsilon_i dv}{\int_v dv}$$

where i = 1, 2, 3, …,6, and σ_i and ε_i are the position-dependent stresses and strains at a point in the material, respectively.

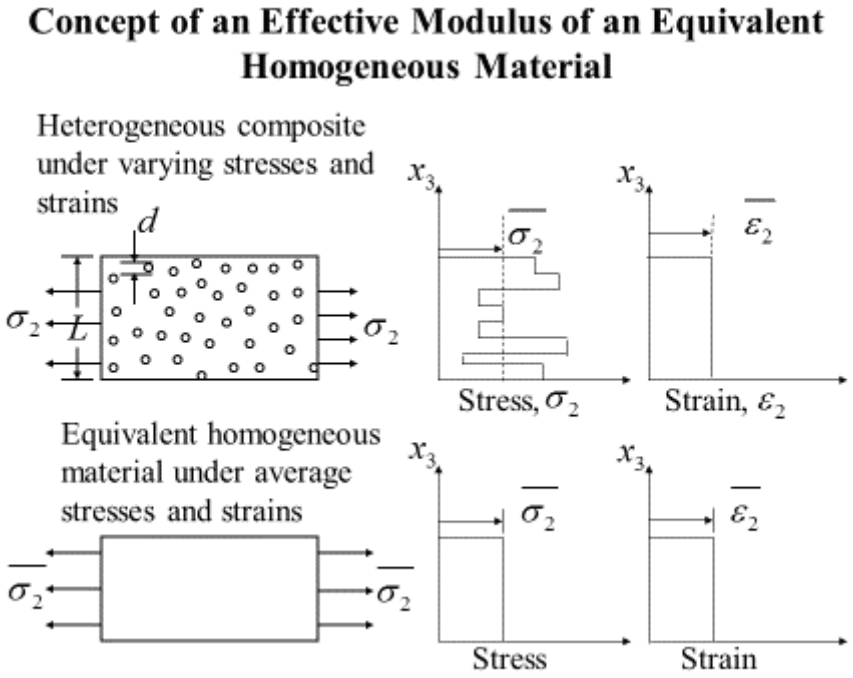

Fig. 2.3: Concept of an effective modulus of an equivalent homogeneous material

Using averaged stresses and strains, the generalized Hooke's law becomes:

$$\overline{\sigma}_i = C_{ij}\overline{\varepsilon}_j i, j = 1,2,...,6$$

and the elastic moduli C_{ij} then become the effective moduli of the equivalent homogeneous material in the volume V. Similarly, the effective compliance S_{ij} is defined as:

$$\overline{\varepsilon}_i = S_{ij}\overline{\sigma}_j i, j = 1,2,...,6$$

2.3 Symmetry in stress-strain relationships

As mentioned above, we have different symmetries in stress-strain relationships that reduce the number of independent elastic moduli of the stiffness matrix. First, only as a result of the existence of a strain energy density function, which has nothing to deal with material symmetry, we can say that the stiffness matrix is symmetric, so only 21 of the 36 anisotropic elastic moduli are independent. Now, the form of the stiffness matrix is:

$$C_{ij} = \begin{bmatrix} C_{11} & C_{12} & C_{13} & C_{14} & C_{15} & C_{16} \\ & C_{22} & C_{23} & C_{24} & C_{25} & C_{26} \\ & & C_{33} & C_{34} & C_{35} & C_{36} \\ & \text{SYM} & & C_{44} & C_{45} & C_{46} \\ & & & & C_{55} & C_{56} \\ & & & & & C_{66} \end{bmatrix}$$

Fig. 2.4: Stiffness matrix

Now, if we consider material symmetries, we can have further simplifications in the stiffness matrix. For example, a monoclinic material, viz. a material with one plane of material property symmetry, has only 13 independent elastic moduli constants, due to its invariance under a transformation of coordinates. But this material is not of practical interest in composite material analysis.

A unidirectional composite lamina has three mutually orthogonal planes of material property symmetry, and is called orthotropic material. The stiffness matrix is still of the form of the figure 2.4. The number of the abovementioned constants reduce to 9, if the coordinates system is referred to principal material coordinates (Figure 2.5), and the material is called a specially orthotropic material. Other form of material symmetries is quoted in table 2.1.

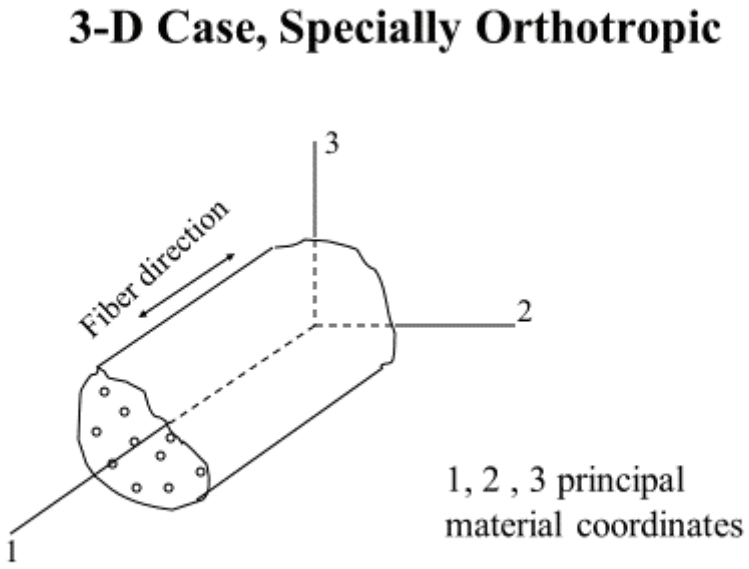

Fig. 2.5: Specially Orthotropic material

Material and coordinate system	Number of nonzero coefficients	Number of independent coefficients
3–D case		
Anisotropic	36	21
Generally Orthotropic (nonprincipal coordinates)	36	9
Specially Orthotropic (Principal coordinates)	12	9
Specially Orthotropic, transversely isotropic	12	5
Isotropic	12	2
2–D case (lamina)		
Anisotropic	9	6
Generally Orthotropic (nonprincipal coordinates)	9	4
Specially Orthotropic (Principal coordinates)	5	4
Balanced orthotropic, or square symmetric	5	3
Isotropic	5	2

Table 2.1: Number of elastic coefficients in the stiffness matrix

2.4 Orthotropic and isotropic engineering constants

When a material has to be characterized experimentally, instead of the C_{ij} or the S_{ij} constants, usually the so-called "engineering constants", i.e. Young's modulus, shear modulus and Poisson's ratio, are widely used.

In order to define lamina engineering constants, consider a 3-D state of stress consisting of all possible normal and shear stress associated with the 123 axes as shown in fig. 2.1 and 2.5. The set of equations derived from this consideration is:

$$\begin{Bmatrix} \varepsilon_1 \\ \varepsilon_2 \\ \varepsilon_3 \\ \gamma_{23} \\ \gamma_{31} \\ \gamma_{12} \end{Bmatrix} = \begin{bmatrix} \frac{1}{E_1} & -\frac{\upsilon_{21}}{E_2} & -\frac{\upsilon_{31}}{E_3} & 0 & 0 & 0 \\ -\frac{\upsilon_{12}}{E_1} & \frac{1}{E_2} & -\frac{\upsilon_{32}}{E_3} & 0 & 0 & 0 \\ -\frac{\upsilon_{13}}{E_1} & -\frac{\upsilon_{23}}{E_2} & \frac{1}{E_3} & 0 & 0 & 0 \\ 0 & 0 & 0 & \frac{1}{G_{23}} & 0 & 0 \\ 0 & 0 & 0 & 0 & \frac{1}{G_{31}} & 0 \\ 0 & 0 & 0 & 0 & 0 & \frac{1}{G_{12}} \end{bmatrix} \begin{Bmatrix} \sigma_1 \\ \sigma_2 \\ \sigma_3 \\ \tau_{23} \\ \tau_{31} \\ \tau_{12} \end{Bmatrix} \tag{2.4}$$

where:

- E_1 is the longitudinal modulus of elasticity associated with the 1 direction;
- E_2 is the transverse modulus of elasticity associated with the 2 direction;
- E_3 is the modulus of elasticity associated with the 3 direction;
- G_{12} is the shear modulus associated with 12 direction;
- G_{31} is the shear modulus associated with 31 direction;
- G_{23} is the shear modulus associated with 23 direction;
- ν_{12} is the Poisson's ratio of the strain in the 2 direction to the strain in the perpendicular 1 direction when the applied stress is in the 1 direction;
- ν_{13} is the Poisson's ratio of the strain in the 3 direction to the strain in the perpendicular 1 direction when the applied stress is in the 1 direction;
- ν_{23} is the Poisson's ratio of the strain in the 3 direction to the strain in the perpendicular 2 direction when the applied stress is in the 2 direction;

Note that, due to the symmetry of the compliance matrix, only 9 of the engineering constants are independent. Furthermore, since $[S] = [C]^{-1}$, the compliance matrix is of the same form of the stiffness matrix for a specially orthotropic material.

If we consider now an applied normal stress σ_x along an arbitrary x axis, the compliance matrix is fully populated, and we say that we have a "shear-coupling effect" between shear strains due to normal stresses and normal strains due to shear stresses. This general 3-D state of stress associated with the arbitrary xyz axes is called a generally orthotropic material. Obviously, if possible, the specially orthotropic material is preferred when experimental characterization is requested, due to its analysis simplification along the principal material directions. We can obtain the generally orthotropic material characterization by transformation equations involving the angle between the principal axes and the arbitrary axes.

In case of specially orthotropic material and transversely isotropic, as shown in fig. 2.5, equations 2.4 are interchangeable, wiz $G_{13} = G_{12}$, $E_2 = E_3$, $\nu_{21} = \nu_{31}$ and $\nu_{23} = \nu_{32}$. In addition, we have:

$$G_{23} = \frac{E_2}{2(1+\nu_{32})}$$

2.5 Specially orthotropic lamina

Assuming that a lamina can be considered as a simple 2-D state of stress (or plane stress), the specially orthotropic stress-strain relationships become:

$$\begin{Bmatrix} \varepsilon_1 \\ \varepsilon_2 \\ \gamma_{12} \end{Bmatrix} = \begin{bmatrix} S_{11} & S_{12} & 0 \\ S_{21} & S_{22} & 0 \\ 0 & 0 & S_{66} \end{bmatrix} \begin{Bmatrix} \sigma_1 \\ \sigma_2 \\ \tau_{12} \end{Bmatrix} \qquad 2.5$$

where:

$$S_{11} = \frac{1}{E_1} \qquad S_{22} = \frac{1}{E_2} \qquad S_{12} = S_{21} = -\frac{\upsilon_{21}}{E_2} = -\frac{\upsilon_{12}}{E_1} \qquad S_{66} = \frac{1}{G_{12}} \qquad 2.6$$

are the relations between the compliances S_{ij} and the engineering constants. Now we have only four nonzero independent compliances. In terms of tensor strains, the lamina stresses are given by:

$$\begin{Bmatrix}\sigma_1\\ \sigma_2\\ \tau_{12}\end{Bmatrix}=\begin{bmatrix}Q_{11} & Q_{12} & 0\\ Q_{21} & Q_{22} & 0\\ 0 & 0 & 2Q_{66}\end{bmatrix}\begin{Bmatrix}\varepsilon_1\\ \varepsilon_2\\ \dfrac{\gamma_{12}}{2}\end{Bmatrix} \qquad 2.7$$

where Q_{ij} are the components of the lamina stiffness matrix. We can easily obtain these components by inverting the compliance matrix. The resulting equations are:

$$Q_{11}=\frac{S_{22}}{S_{11}S_{22}-S_{12}{}^2}=\frac{E_1}{1-\upsilon_{12}\upsilon_{21}} \qquad Q_{12}=-\frac{S_{12}}{S_{11}S_{22}-S_{12}{}^2}=\frac{\upsilon_{12}E_2}{1-\upsilon_{12}\upsilon_{21}}$$

$$Q_{22}=\frac{S_{11}}{S_{11}S_{22}-S_{12}{}^2}=\frac{E_2}{1-\upsilon_{12}\upsilon_{21}} \qquad Q_{66}=\frac{1}{S_{66}}=G_{12}$$

Table 2.2 shows some typical values of lamina engineering constants for several composites.

Material	E_1 [GPa]	E_2 [GPa]	G_{12} [GPa]	ν_{12}
T300/934	131	10.3	6.9	0.22
AS/3501	138	9.0	6.9	0.30
IM7/8551-7	162	8.34	2.07	0.34
Kevlar 49/934	75.8	5.5	2.3	0.34
Boron/5505	204	18.5	5.59	0.23
HexPly® M21	130	9	4.4	0.25

Table 2.2: Typical values of engineering constants for some composites.

2.6 Generally orthotropic lamina

Often, when we build an aeronautical primary structure, we have multiple laminae. In the analysis of laminates, it is then necessary to know the stress-strain relationships in different direction, not only those of the principal axes. We need the relationships for the generally orthotropic lamina in non-principal coordinates. The figure 2.6 shows clearly the principal axes 12 related to an off-axis coordinates xy.

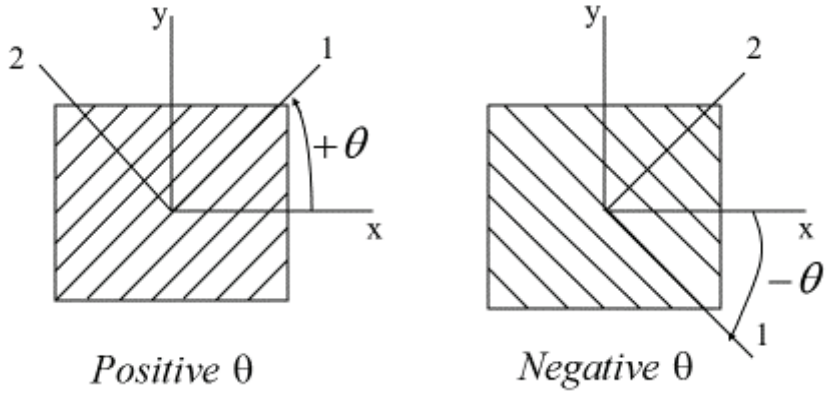

Fig. 2.6: Sign convention for lamina orientation.

To obtain relationships for transformation of stress components between coordinate axes, we have to write the equations of equilibrium for the wedge-shaped differential element. Considering figure 2.7, along the x direction, we have:

$$\sum F_x = \sigma_x dA - \sigma_1 dA cos^2\,\theta - \sigma_2 dA sin^2\theta + 2\tau_{12} dA \sin\theta \cos\theta = 0 \qquad 2.8$$

Dividing by *dA,* we have:

$$\sigma_x = \sigma_1 cos^2\theta + \sigma_2 sin^2\theta - 2\tau_{12} \sin\theta \cos\theta \qquad 2.9$$

If we operate in this manner for the other directions, the complete set of transformation for the stresses in the *xy*-coordinate system can be written as

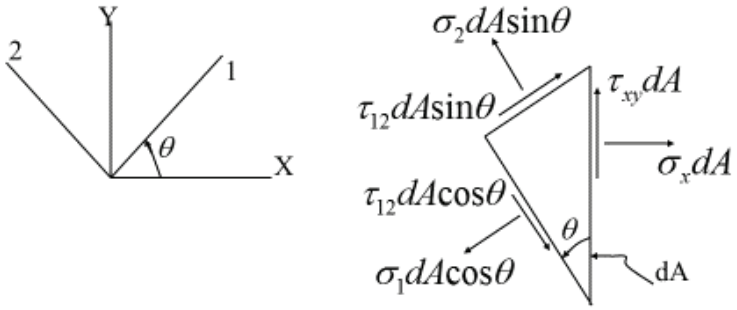

Fig. 2.7: Differential element under static equilibrium with forces in two coordinates systems.

$$\begin{Bmatrix} \sigma_X \\ \sigma_Y \\ \tau_{XY} \end{Bmatrix} = \begin{bmatrix} c^2 & s^2 & -2cs \\ s^2 & c^2 & 2cs \\ cs & -cs & c^2 - s^2 \end{bmatrix} \begin{Bmatrix} \sigma_1 \\ \sigma_2 \\ \tau_{12} \end{Bmatrix} = [T]^{-1} \begin{Bmatrix} \sigma_1 \\ \sigma_2 \\ \tau_{12} \end{Bmatrix} \qquad 2.10$$

Inverting equations 2.7, we can write:

$$\begin{Bmatrix} \sigma_1 \\ \sigma_2 \\ \tau_{12} \end{Bmatrix} = [T] \begin{Bmatrix} \sigma_X \\ \sigma_Y \\ \tau_{XY} \end{Bmatrix} \qquad 2.11$$

where c=cosθ and s=sinθ, and T, the transformation matrix, is defined as:

$$[T] = \begin{bmatrix} c^2 & s^2 & 2cs \\ s^2 & c^2 & -2cs \\ -cs & cs & c^2 - s^2 \end{bmatrix} \qquad 2.12$$

In a similar way, we obtain the tensor strains transform:

$$\begin{Bmatrix} \varepsilon_1 \\ \varepsilon_2 \\ \gamma_{12}/2 \end{Bmatrix} = [T] \begin{Bmatrix} \varepsilon_x \\ \varepsilon_y \\ \gamma_{xy}/2 \end{Bmatrix} \qquad 2.13$$

Combining equations 2.13 and 2.7, and substituting in equation 2.10, we find that:

$$\begin{Bmatrix} \sigma_x \\ \sigma_y \\ \tau_{xy} \end{Bmatrix} = [T]^{-1}[Q][T] \begin{Bmatrix} \varepsilon_x \\ \varepsilon_y \\ \gamma_{xy}/2 \end{Bmatrix} \qquad 2.14$$

Carrying out matrix multiplications and converting back to engineering strains, we have:

$$\begin{Bmatrix} \sigma_x \\ \sigma_y \\ \tau_{xy} \end{Bmatrix} = \begin{bmatrix} \overline{Q}_{11} & \overline{Q}_{12} & \overline{Q}_{16} \\ \overline{Q}_{12} & \overline{Q}_{22} & \overline{Q}_{26} \\ \overline{Q}_{16} & \overline{Q}_{26} & \overline{Q}_{66} \end{bmatrix} \begin{Bmatrix} \varepsilon_x \\ \varepsilon_y \\ \gamma_{xy} \end{Bmatrix} \qquad 2.15$$

Where $\overline{Q}_{ij}$ are the components of the transformed lamina stiffness matrix, defined as follows:

$$
\begin{aligned}
\overline{Q}_{11} &= Q_{11}c^4 + Q_{22}s^4 + 2(Q_{12} + 2Q_{66})s^2c^2 \\
\overline{Q}_{12} &= (Q_{11} + Q_{22} - 4Q_{66})s^2c^2 + Q_{12}(c^4 + s^4) \\
\overline{Q}_{22} &= Q_{11}s^4 + Q_{22}c^4 + 2(Q_{12} + 2Q_{66})s^2c^2 \\
\overline{Q}_{16} &= (Q_{11} - Q_{12} - 2Q_{66})c^3s - (Q_{22} - Q_{12} - 2Q_{66})cs^3 \\
\overline{Q}_{26} &= (Q_{11} - Q_{12} - 2Q_{66})cs^3 - (Q_{22} - Q_{12} - 2Q_{66})c^3s \\
\overline{Q}_{66} &= (Q_{11} + Q_{22} - 2Q_{12} - 2Q_{66})s^2c^2 + Q_{66}(s^4 + c^4)
\end{aligned}
\qquad 2.16
$$

Note that although the transform lamina stiffness matrix has the same form as that of an anisotropic material, only four of the nine components are independent, for the same reason of a specially orthotropic lamina, i.e. the material is always the same, but not recognizable as such in an off-axis coordinates. As mentioned in par. 2.4, it is much easier to work with the principal material coordinates. This is why the relationships are written related to their engineering constants. We can then express the strains in terms of the stresses as:

$$
\begin{Bmatrix} \varepsilon_x \\ \varepsilon_y \\ \gamma_{xy} \end{Bmatrix} = \begin{bmatrix} \overline{S}_{11} & \overline{S}_{12} & \overline{S}_{16} \\ \overline{S}_{12} & \overline{S}_{22} & \overline{S}_{26} \\ \overline{S}_{16} & \overline{S}_{26} & \overline{S}_{66} \end{bmatrix} \begin{Bmatrix} \sigma_x \\ \sigma_y \\ \tau_{xy} \end{Bmatrix} \qquad 2.17
$$

where $\left[\overline{S}\right] = [\overline{Q}]^{-1}$ is the transformed lamina compliance matrix, or in expanded form:

$$
\begin{aligned}
\overline{S}_{11} &= S_{11}c^4 + \left(2S_{12} + S_{66}\right)s^2c^2 + S_{22}s^4 \\
\overline{S}_{12} &= S_{12}\left(s^4 + c^4\right) + \left(S_{11} + S_{22} - S_{66}\right)s^2c^2 \\
\overline{S}_{22} &= S_{11}s^4 + \left(2S_{12} + S_{66}\right)s^2c^2 + S_{22}c^4 \\
\overline{S}_{16} &= \left(2S_{11} - 2S_{12} - S_{66}\right)sc^3 - \left(2S_{22} - 2S_{12} - S_{66}\right)s^3c \\
\overline{S}_{26} &= \left(2S_{11} - 2S_{12} - S_{66}\right)s^3c - \left(2S_{22} - 2S_{12} - S_{66}\right)sc^3 \\
\overline{S}_{66} &= 2\left(2S_{11} + 2S_{22} - 4S_{12} - S_{66}\right)s^2c^2 + S_{66}\left(s^4 + c^4\right)
\end{aligned}
\qquad 2.18
$$

Eventually, we can transform the lamina engineering constants from the principal material axes to the off-axes coordinates. For example, the off-axes longitudinal modulus of elasticity associated with uniaxial loading along the x direction is defined as:

$$E_x = \frac{\sigma_x}{\varepsilon_x} = \frac{\sigma_x}{\bar{S}_{11}\sigma_x} = \frac{1}{\bar{S}_{11}} \qquad 2.19$$

where ε_x has been found substituting the stress conditions $\sigma_x \neq 0, \sigma_y = \tau_{xy} = 0$ in equation 2.17. Combining equations 2.18 and 2.19, using the set of equations 2.6, we have:

$$E_x = \left[\frac{1}{E_1} c^4 + \left(\frac{1}{G_{12}} - \frac{2\upsilon_{12}}{E_1} \right) s^2 c^2 + \frac{1}{E_2} s^4 \right]^{-1}$$

$$E_y = \left[\frac{1}{E_1} s^4 + \left(\frac{1}{G_{12}} - \frac{2\upsilon_{12}}{E_1} \right) s^2 c^2 + \frac{1}{E_2} c^4 \right]^{-1} \qquad 2.20$$

$$G_{xy} = \left[\frac{1}{G_{12}} \left(s^4 + c^4 \right) + 4 \left(\frac{1}{E_1} + \frac{1}{E_2} + \frac{2\upsilon_{12}}{E_1} - \frac{1}{2G_{12}} \right) s^2 c^2 \right]^{-1}$$

$$\upsilon_{xy} = E_x \left[\frac{\upsilon_{12}}{E_1} \left(s^4 + c^4 \right) - \left(\frac{1}{E_1} + \frac{1}{E_2} - \frac{1}{G_{12}} \right) s^2 c^2 \right]$$

E_y, G_{xy} and ν_{xy} can be obtained from similar derivations.

CHAP. 3: THE FINITE ELEMENT ANALYSIS SOFTWARE: ABAQUS®

3.1 Introduction

When scientists or engineers analyze a physical phenomenon in nature, the first thing they do is to create mathematical models. The principal effort is to find a set of equations with the aid of physical or mathematical laws in terms of differential or integral relationships between various variables of interest. This is what we did in chapter two when we find the relationships related with stresses and strains in a carbon fiber lamina. The second step consists to evaluate the mathematical model of a process and estimate its characteristic using a numerical method and a computer. This process is called numerical simulation. The synergy between mathematical models and use of numerical simulations of physical systems leads to computational mechanics.

Why is it so important the use of numerical simulations? The answers are different. For example, sometimes, we don't have analytical solutions of a problem, due to its complicated domains and nonlinearities, and the unique way to find an approximate solution is to use numerical methods. Another reason is to reduce experimental time and to save material resources, a numerical simulation can be run a thousand times in relative few time compared to the multitude of physical experiments needed to obtain the same results. Furthermore, some emerging technologies rely on finite element analysis to simulate complex physical phenomenon using different scale for manufacture and design of hi-tech products. In our case, the nonlinearities due to anisotropic material, as CFRP laminates, is the main reason of the use of the finite element method.

3.2 Basic FEM Procedure [Reddy, 2005]

The finite element method is a numerical method that use the finite difference method or a variational method to solve real-world problems that involve complicated physics, geometry and boundary conditions. The main idea is to divide a given domain in a collection of subdomains, called finite elements, that will be solved easily by an approximate solution. Each solution and its derivative has to be continuous with the neighboring subdomains, in order to have continuity between the subdomain sequential segments.

The procedure to achieve a finite element analysis is implemented by three steps. First, for a given geometrically complex domain Ω of a problem, we have to divide it in a collection of subdomains Ω_e, geometrically simpler and independent, called finite elements; second,

develop a set of algebraic equations over each finite element, using the governing equations of the problem; third, the relationships from all elements are assembled by the use of some interelement relationships. The figure 3.1 explains better the concept beyond.

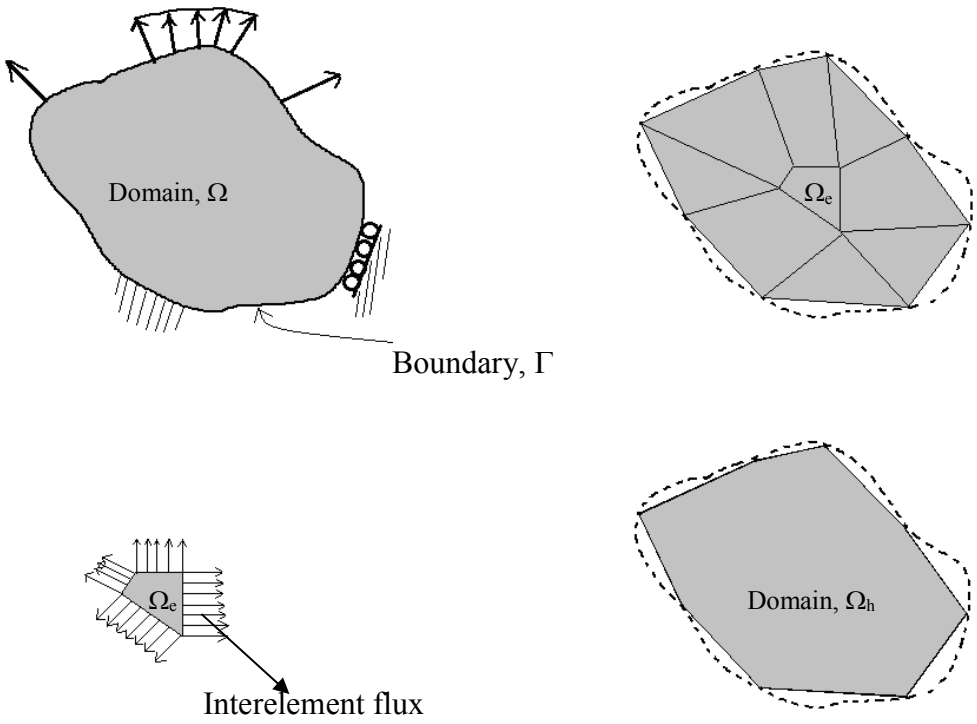

Fig. 3.1: Representation of a two-dimensional domain by a collection of triangles and quadrilaterals.

Note that a numerical simulation enters approximations at several stages! In the first step, when we divide the original domain in subdomains, then when we solve element equations (interpolation functions are derived by interpolation theory), and in the last step, we introduce errors in solving the assembled systems of equations, even though some of these errors could be zero.

Summarizing, the finite element method divides a given domain in subdomains, called finite elements, and develop an approximate solution to the problem for each element. This procedure leads to some advantages, for example, we can allow accurate representation of complex geometry and include different material properties (i.e. composite material), and enables capture of local effects by functions defined within each element, simplifying the total solution of a complex problem.

Other considerations that we can do about finite element method are:

- nowadays, the computers are more powerful than the supercomputers when finite element were discovered, so it is easy to implement simulations before any experiment, surely less expensive;
- it is possible to use more than one type of element into a mesh, so that we can enhance accuracy where requested;
- accuracy of the finite element solution depends on the differential equation, its integral form, and the element used;
- convergence depends also on the number of elements of the mesh;
- continuity at the interelement boundaries is fundamental to obtain a solution (with its derivative for higher-order equations) for the assembly of elements.

3.3 The software Abaqus® 6.13 [Abaqus/CAE User's Guide]

For different engineering purposes, we can find many commercial programs that perform a finite element analysis. They solve a big variety of problems, from simple linear static analysis, i.e. deformations of isotropic material, to nonlinear transient analysis, like high speed impact with anisotropic material, i.e. a composite lamina. Only a few of these programs, such as ANSYS or Abaqus, have special capabilities to analyze composite materials, accepting user-defined constitutive equations and new element formulations. These codes are also called Computer Aided Engineering (CAE) because of providing not only analysis tools, geometric modelling and visualization of results, but also integration with larger design production and product life-cycle process.

Commonly, modern Finite Element Analysis codes are divided into three blocks: the pre-processor, the processor and the post-processor. In the first one, the model is built defining geometry, material properties and element type. Sometimes, also loads and boundary conditions are entered in the pre-processor. The processor, with this information, can compute the stiffness matrix and the force vector. Next, the solution is obtained in the form of displacement values. The last block, the post-processor, derived results such as stress, strain, failure ratio and so on. Next, they are visualized through graphic interface.

Abaqus/CAE® is a complete Abaqus environment that provides a simple, consistent interface for creating, submitting, monitoring, and evaluating results from Abaqus/Standard simulations. Abaqus/CAE is divided into modules, where each module defines a logical aspect of the modeling process; for example, defining the geometry, defining material properties, and generating a mesh. As you move from module to module, you build the model from which Abaqus/CAE generates an input file that is submitted to the Abaqus/Standard or Abaqus/Explicit analysis product. The analysis product performs the analysis, sends

information to Abaqus/CAE to monitor the progress of the job, and generates an output database. Finally, the Visualization module of Abaqus/CAE reads the output database and views the results of analysis.

Abaqus works with a model database (extension: model_name.cae) that stores, models and analyses jobs. A model database can contain more than one model; if we have to work on multiple models simultaneously, they must be stored in one model database. The model database in use is known as the current model database; Abaqus/CAE displays the name of the current model database across the top of the main window, as shown in figure 3.2.

The first requirement of a model is the geometry. Then, materials properties are given for the different parts of the model. Next, boundary conditions and loads are applied on the geometry, then, the geometry is discretized into elements, defined in terms of nodes and element connectivity. Element type are chosen depending on the type of problem to be solved. Now the problem can be solved and derived results are computed and visualized.

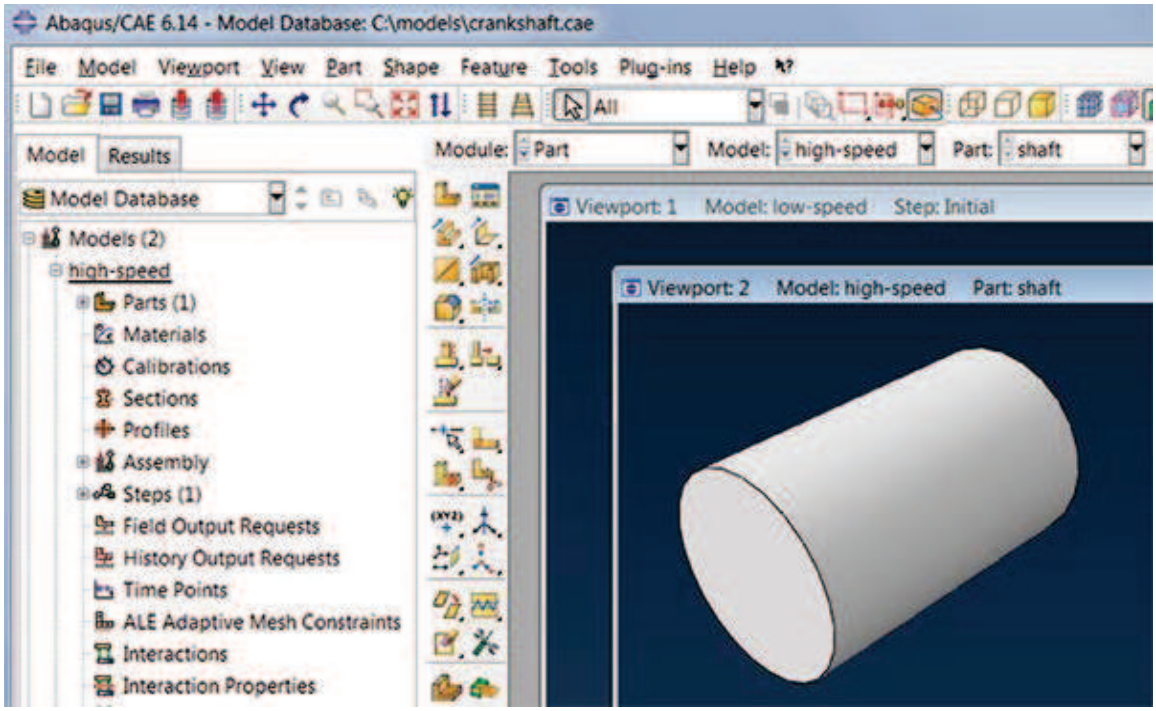

Fig. 3.2: Abaqus/CAE displays the model database name and the model name.

An Abaqus/CAE model contains the following kinds of objects:

- parts
- materials and sections
- assembly
- sets and surfaces
- steps

- loads, boundary conditions, and fields
- interactions and their properties
- meshes

A model database can contain any number of models so that we can keep all models related to a single problem in one database. We can open multiple models from the model database at the same time, and it is possible to work on different models in different viewports. The viewport title bar (if visible) displays the name of the model associated with the viewport. The model associated with the current viewport is called the current model, and there is only one current model. Figure 3.2 shows two viewports displaying two different models (high-speed and low-speed) in the same model database (crankshaft.cae); the current viewport in Figure 3.2 is displaying the high-speed model.

When we start a session and begin defining your model, Abaqus/CAE generates some file, some of which are the following:

- The replay file (abaqus.rpy): the replay file contains Abaqus/CAE commands that record almost every modeling operation performed during a session;
- The model database file (model_database_name.cae): the model database file contains models and analysis jobs;
- The journal file (model_database_name.jnl): the journal file contains the Abaqus/CAE commands that will replicate the model database that was saved to disk.

When a job is submitted for analysis, Abaqus/Standard and Abaqus/Explicit create a set of files, some of which are the following:

- Input files (job_name.inp): Abaqus/CAE generates an input file that is read by Abaqus/Standard or Abaqus/Explicit when you submit a job for analysis;
- Output database files (job_name.odb): Output database files contain the results from your analysis. The Step module's output request managers is used to choose which variables are written to the output database during the analysis and at what rate. An output database is associated with the job you submit from the Job module; for example, if you named your job FrictionLoad, the analysis creates an output database called FrictionLoad.odb.

  When an output database is opened, Abaqus/CAE® loads the Visualization module and allows us to view a graphical representation of the contents. We can also import a part from an output database as a mesh or save X–Y data objects to an output database file if we open the file with write permission; otherwise, it is impossible to modify the contents of the output database once it has been created;
- The output database lock file (job_name.lck): the lock file is written whenever an output

database file is opened with write access, including when an analysis is running and writing output to an output database file. The lock file is created to prevent from having simultaneous write permission to the output database from multiple sources. It is deleted automatically when the output database file is closed or when the analysis that creates it ends;

- The restart file (job_name.res): the restart file is used to continue an analysis that stopped before it was complete;
- The data file (job_name.dat): the data file contains printed output from the analysis input file processor, as well as printed output of selected results written during the analysis. Abaqus/CAE automatically requests that the default printed output for the current analysis procedure be generated at the end of each step;
- The message file (job_name.msg): the message file contains diagnostic or informative messages about the progress of the solution;
- The status file (job_name.sta): the status file contains information about the progress of the analysis;
- The results file (job_name.fil): the results file contains selected results from the analysis in a format that can be read by other applications, such as post-processing programs;

Interactions with Abaqus/CAE are possible through the main window, which changes its appearance through the modeling process. Figure 3.3 shows the components that appear in the main window. The components are:

- Title bar: The title bar indicates the release of Abaqus/CAE and the name of the current model database.
- Menu bar: The menu bar contains all the available menus; the menus give access to all the functionality of the code. Different menus appear in the menu bar depending on which module is selected from the context bar.
- Toolbars: The toolbars provide quick access to items that are also available in the menus.
- Context bar: Abaqus/CAE is divided into a set of modules, where each module works on one aspect of the model; the Module list in the context bar permits to move between these modules.
- Model Tree: The Model Tree provides a graphical overview of the model and the objects that it contains, such as parts, materials, steps, loads, and output requests. In addition, the Model Tree provides a convenient, centralized tool for moving between modules and for managing objects. If your model database contains more than one model, we can use the Model Tree to move between models.

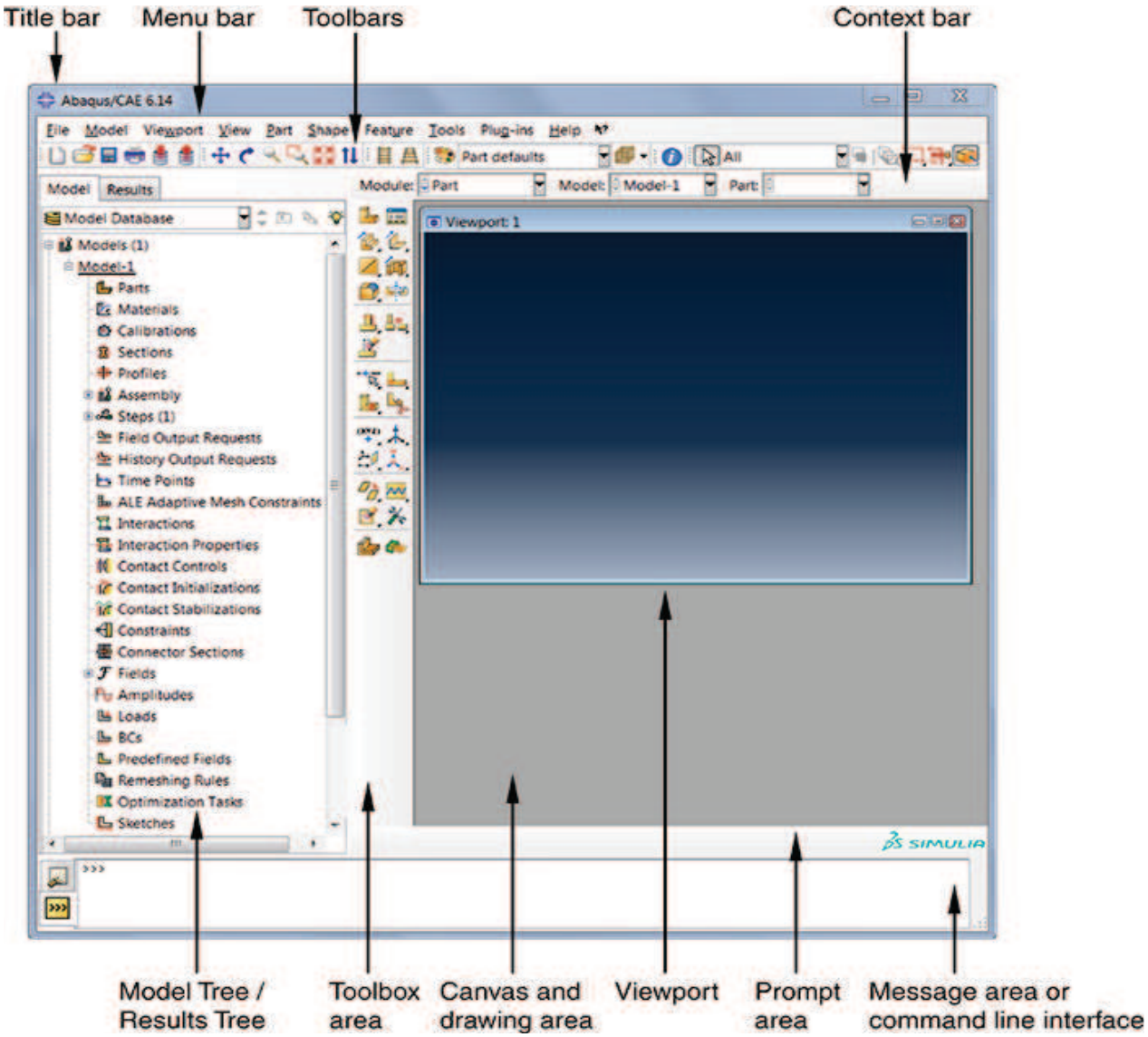

Fig. 3.3: Components of the main window

- Results Tree: The Results Tree give us a graphical overview of the output databases and other session-specific data such as X–Y plots. If there is more than one output database open in your session, it is possible to use the Results Tree to move between output databases;
- Toolbox area: When a specific module is used, the toolbox area displays tools in the toolbox that are appropriate for that module. The toolbox allows quick access to many of the module functions that are also available from the menu bar;
- Canvas and drawing area: The canvas can be thought of as an infinite screen or bulletin board on which viewports are posted;
- Viewport: Viewports are windows on the canvas in which Abaqus/CAE displays the model;

- Prompt area: The prompt area displays instructions to follow during a procedure;
- Message area: Abaqus/CAE prints status information and warnings in the message area;
- Command line interface: The command line interface is used to type Python commands and to evaluate mathematical expressions using the Python interpreter that is built into Abaqus/CAE®.

CHAP. 4 : THE COHESIVE ZONE MODEL TECHNIQUE

4.1 Introduction

In this chapter, a brief overview of cohesive models and their properties is given. [Cornec et al., 2003]. Cohesive models are used to describe damage and fracture in a wide range of materials at various length and time scales. These materials include metals, polymers, ceramics, concrete, fibre reinforced materials, wood, rock, glass, and others. As early as 1960, Dugdale introduced a strip-yield model with the idea of a cohesive force preventing a crack from extending [Dudgale, 1960]. The magnitude of this cohesive force is equal to the yield strength of the material; strain hardening is not considered, i.e. the material is supposed to behave in an elastic-ideally plastic manner. Since the local stress is limited by the yield strength of the material, the occurrence of a physically unrealistic singularity at the crack tip is avoided, as shown in figure 4.1.

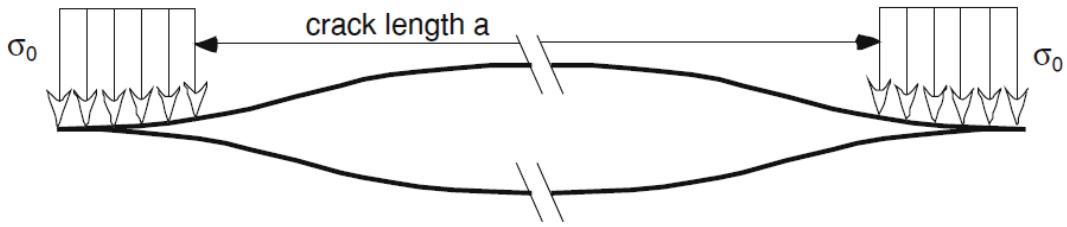

Fig. 4.1: The Dudgale model

The result of this analysis is the length of the plastic zone ahead of a crack in an infinitely wide sheet subjected to a crack opening Mode I load; it is valid for small scale as well as wide spread yielding until the applied stress reaches the yield strength. Later, Goodier and Field applied the Dugdale model to the determination of the opening profile of the crack including the crack tip opening displacement.

The cohesive models in their present form date back to the work of Barenblatt who replaced the yield strength with a cohesive law to model the atomic lattices decohesion (fig. 4.2). This way, the plastic zone was replaced by a process zone within which damage and fracture occur.

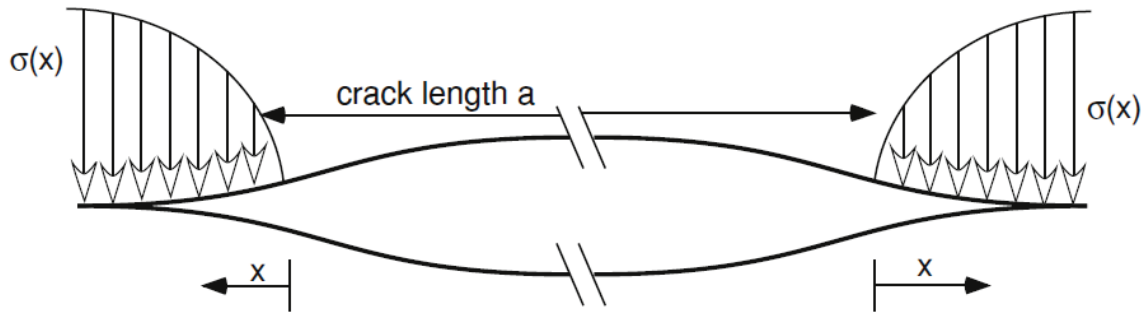

Fig. 4.2: The Barenblatt model

The detailed processes are:

- Plastic deformation;
- Initiation, growth, and coalescence of voids in ductile materials;
- Micro cracking in brittle materials.

Material degradation and separation are concentrated in a discrete plane, represented by cohesive elements, which are embedded in the continuum elements representing the test piece or structural component. In both the Dugdale and Barenblatt models, the stresses along the ligament within the process zone do no longer depend on the applied load; they are now a material property. It should be noted that in Barenblatt's model the traction is expressed as a function of the distance from the crack tip, whereas the cohesive models actually in use define the traction as functions of the separation within the cohesive zone. Material degradation and separation are concentrated in a discrete plane, represented by cohesive elements that are embedded in the continuum elements representing the test
piece or structural component. To our knowledge, the first application of the cohesive model to the fracture behaviour of a material was performed by Hillerborg et al. as early as in 1976, who used this model to describe the damage behaviour of concrete. This material has attracted much attention as to its characterisation using the cohesive model. For the other highly important class of engineering materials: metals and their alloys, pioneering work was performed by Needleman, Tvergaard, and Hutchinson. The first analysis of micro damage in ductile materials (particle debonding from a ductile matrix) was performed by Needleman in 1987, and the first macroscopic crack extension in ductile materials was analysed by [Tvergaard and Hutchinson, 1992]. Figure 4.3 shows how the physical process can be represented by the cohesive model. Experimental validation of the cohesive model for ductile materials has been investigated later on, e.g. by [Yuan et al. 1996].

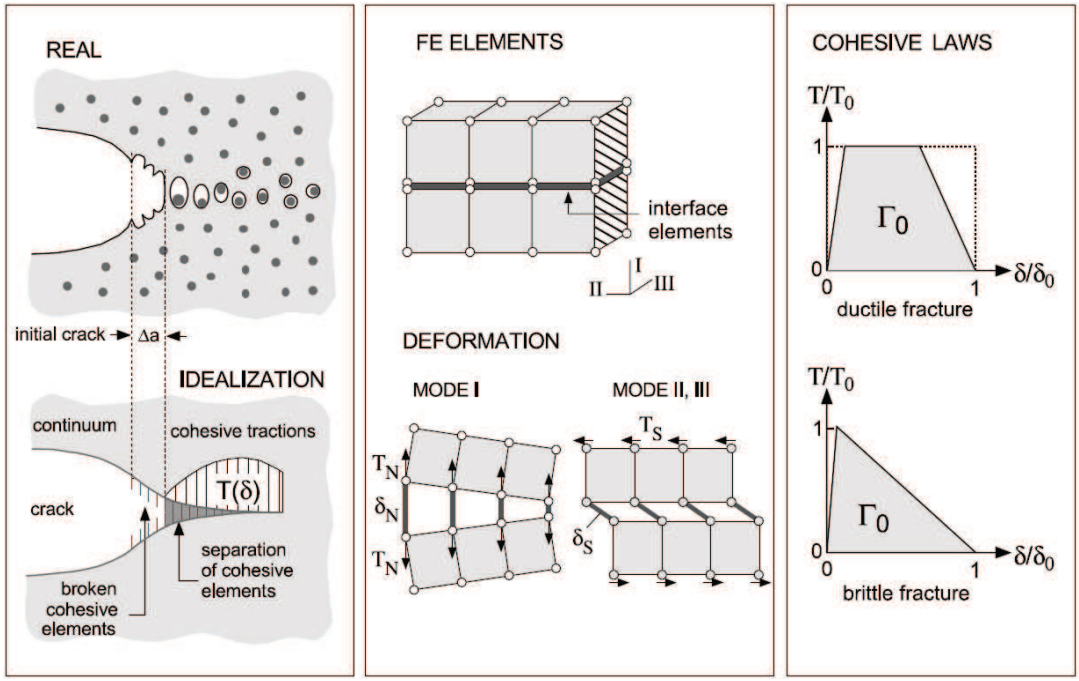

Fig. 4.3: Cohesive model: representation of the physical damage process by separation function within numerical interfaces of zero height, i.e. the cohesive elements

4.2 Traction-separation law

The constitutive behaviour of the cohesive model is formulated as a traction-separation law (TSL), which relates the traction, T, to the separation, δ, (figure 4.3) which represents the displacement jump within the cohesive elements. A cohesive element fails when the separation attains a material specific critical value, δ_0. The related stress is then zero. The maximum stress reached in a TSL, the cohesive strength, T_0, is a further material parameter. A host of traction–separation laws (TSL) have been suggested. Figure 4.4 gives an overview of frequently used shapes. Brittle crack extension analyses of concrete were the first applications of the cohesive model. In purely brittle materials, the traction-separation law can be easily identified, since all deformation that is inelastic can be assumed to be a material separation. Therefore, the traction-separation behaviour can be determined from a simple uniaxial tensile test, in which the stress state is homogeneous and the elastic deformation can be subtracted from the global structural response.

The resulting traction-separation law is often approximated by a linearly decreasing function (Fig. 4.4c) or by a bilinear function (Fig. 4.4d), which has two additional parameters.

For ductile metals, a TSL with a finite initial stiffness and a smooth shape as shown in Fig. 4.4a, sometimes also with a softening curve approaching a horizontal asymptote and thus

approaching zero traction at infinity (Fig. 4.4b), is often used in the literature. Other laws, which are more versatile by introducing additional shape parameters, have also been used. For a given shape of the TSL, the two parameters, δ_0 and T_0, are sufficient for modelling the complete separation process. In practice, it has been proven useful to use the cohesive energy, C_0, instead of the critical separation. The cohesive energy is the work needed to create a unit area of fracture surface (in fact twice the unit fracture surface because of the two mating fracture surfaces) and is given by

$$\Gamma_0 = \int_0^{\delta_0} T(\delta) d\delta \qquad 4.1$$

There is a dispute as to whether the traction-separation law should have a finite slope right from the beginning, i.e. also small stresses lead to a material separation, or not. One can see that the shape used for ductile metals has a finite compliance in the beginning as shown in Fig. 4.4a and b, whereas for more brittle materials, Fig. 4.4c and d, the separation is set to zero until the cohesive strength is reached. In order to avoid an unwanted ‘‘elastic’’ opening of the cohesive element, it is advantageous to have a high stiffness in the beginning. For example, in Fig. 4.4e and f the initial compliance can be defined based on additional shape parameters, which specify the separation at which the cohesive strength is reached.
If a traction-separation law is used, which starts without any separation until the cohesive strength is reached (Fig. 4.4c and d), a contact algorithm must be employed in the implementation of the cohesive element, since conventional elements can never have an infinite stiffness. Therefore, a TSL with a finite stiffness in the beginning is more convenient for implementation into an existing finite element code as a user element. The choice of the TSL affects the magnitudes of the cohesive parameters, demonstrating the phenomenological nature of the cohesive model. This means that each traction- separation law requires a different set of parameters for a given problem.

4.3 Tangential separation and mixed mode Fracture

In the case of mixed mode loading, a tangential separation mode, usually designated Mode II and Mode III, accompanies the normally considered crack opening, Mode I. In linear elastic fracture mechanics, a phase angle, Ψ_{LEFM}, can be defined as:

$$\Psi = \tan^{-1}\left(\frac{K_{II}}{K_I}\right) \qquad 4.2$$

where K_I and K_{II} denote the stress intensity factors for crack opening Modes I and II,

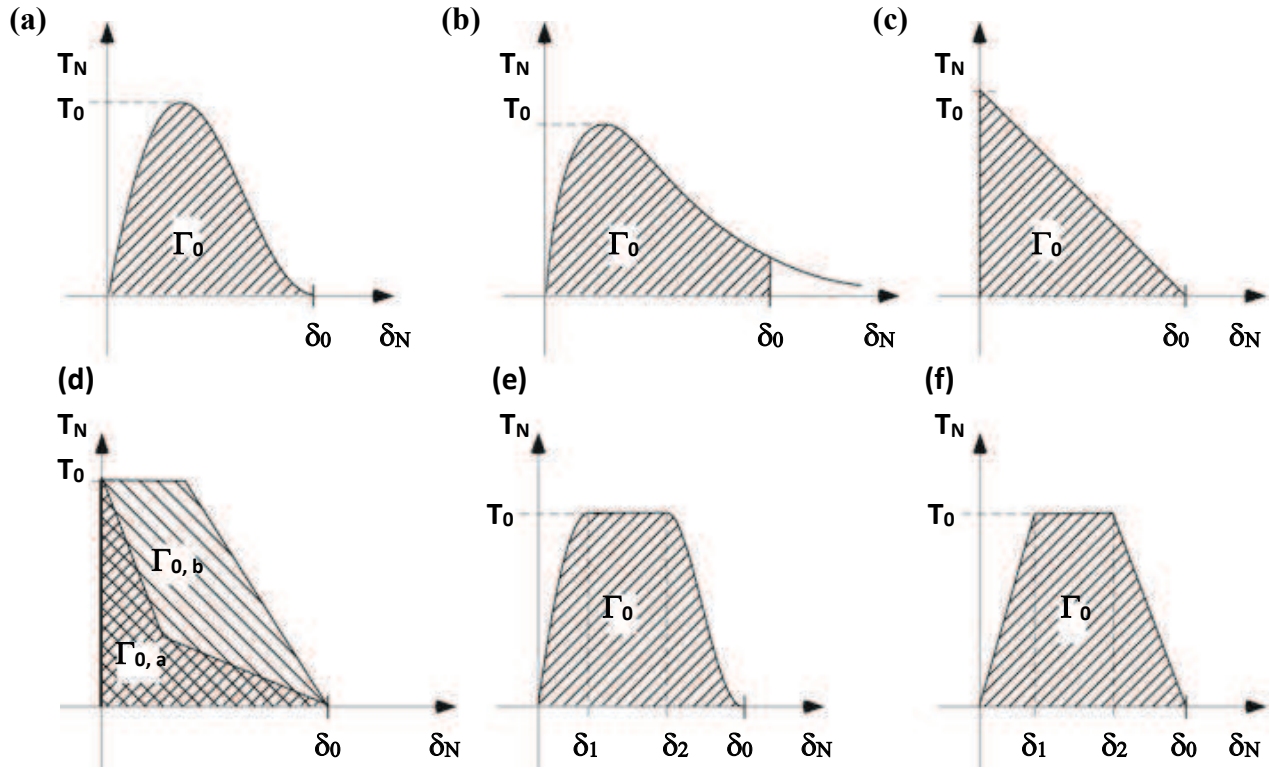

Fig. 4.4: Typical traction–separation laws: **a** Needleman (1987), **b** Needleman (1990), **c** Hillerborg (1976), **d** Bazant (2002), **e** Scheider (2003), **f** Tvergaard and Hutchinson (1992).

respectively. In the context of the cohesive model, a tangential displacement, δ_t, represents the additional shear mode and is superimposed to the displacement normal to the crack plane (or plane of expected damage in the absence of a pre-existing crack), δ_n. In analogy to Eq. (4.2), a phase angle for the cohesive model [Walter et al., 2008] reads:

$$\Psi = \tan^{-1}\left(\frac{\delta_t}{\delta_n}\right) \tag{4.3}$$

Alternatively, the phase angle can be expressed in terms of the energy release rate corresponding to the cohesive energy by re-formulating Eq. (4.2):

$$\Psi = \tan^{-1}\sqrt{\frac{G_{II}}{G_I}} \tag{4.4}$$

In general, the resulting displacement can be obtained from:

$$\delta_{res} = \sqrt{(\delta_n^2 + \delta_t^2)} \tag{4.5}$$

It must be noted that there are almost as many mixed mode formulations for the cohesive model as traction–separation laws. If the simple formulation, Eq. (4.5), is used for an ‘‘effective’’ separation, the resulting traction in normal and tangential directions is calculated by [Camacho et al., 1996]:

$$\boldsymbol{T} = T(\delta_{eff})\left(\frac{\delta_N}{\delta}\boldsymbol{n} + \frac{\delta_t}{\delta}\boldsymbol{t}\right) \tag{4.6}$$

in which **n** and **s** are the normal and the tangential unit vectors of the cohesive element, respectively. A similar formulation is given by an additional weighting factor ß for the tangential separation in Eq. (4.6) as introduced by Camanho and Ortiz, which then leads to:

$$\boldsymbol{T} = T(\delta_{eff})\left(\frac{\delta_N}{\delta}\boldsymbol{n} + \beta^2\frac{\delta_t}{\delta}\boldsymbol{t}\right) \tag{4.7}$$

It is worth noting that mixed mode loading causes path dependency, i.e. damage depends on how the two modes are activated during the loading process.

4.4 Cohesive elements

In this thesis, cohesive elements are considered as interface elements with two surfaces, which usually lie on top of each other in the undeformed state. If, however, the two surfaces have a finite distance in between, the resulting volume does not have any physical meaning, since it is not the strain in the element that is the relevant quantity, but the displacement jump between the surfaces. In order to make the cohesive interface to work well, the volume of the cohesive elements should be as small as possible and negligible compared to any other dimension in the model. In the framework of the finite element method, they have to be implemented corresponding to the surrounding continuum model, i.e. if the structure is modelled by 3D continuum elements, the cohesive elements must consist of surfaces as shown in Fig. 4.6a, if the structure is modelled in 2D or shell elements the cohesive elements reduce to line elements, see Fig. 4.6b and c. The difference between cohesive elements for plane strain/plane stress and shell structures is that the latter are defined in the three dimensional space. Therefore, any separation may be in plane or out of plane, and the in

plane direction must be defined by the user, which can be done by a fifth node as shown in Fig. 4.6c.

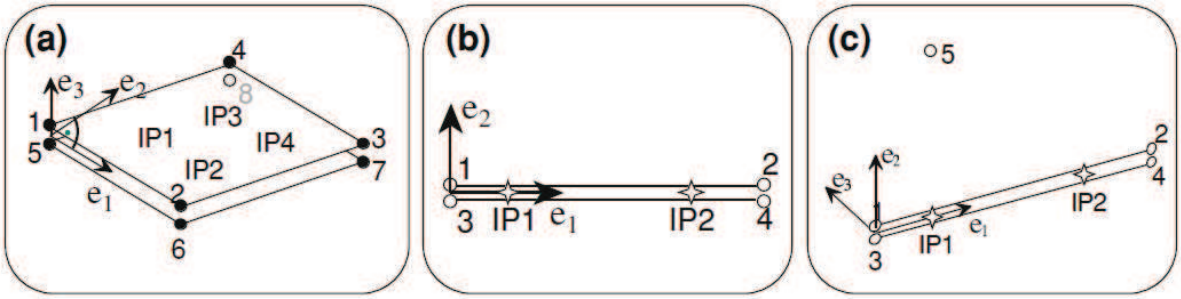

Fig. 4.6: Cohesive element library for 3D FE models (a), for plane stress/strain models (b), and for shell models (c)

Abaqus offers a library of cohesive elements to model the behaviour of adhesive joints, interfaces in composites, and other situations where the integrity and strength of interfaces may be of interest.

Modeling with cohesive elements consists of:

- choosing the appropriate cohesive element type;
- including the cohesive elements in a finite element model, connecting them to other components, and understanding typical modeling issues that arise during modeling using cohesive elements;
- defining the initial geometry of the cohesive elements and defining the mechanical constitutive behaviour of the cohesive elements.

The mechanical constitutive behaviour of the cohesive elements can be defined:

- with a continuum-based constitutive model, if we have to define an adhesive layer of finite thickness or
- by using a constitutive model specified directly in terms of traction versus separation.

Cohesive elements are useful in modeling adhesives, bonded interfaces, gaskets, and rock fracture. The constitutive response of these elements depends on the specific application and is based on certain assumptions about the deformation and stress states that are appropriate for each application area. The nature of the mechanical constitutive response may broadly be classified to be based on:

- a continuum description of the material; or
- a traction-separation description of the interface.

4.4.1 Continuum-based modeling

The modeling of adhesive joints involves situations where two bodies are connected together by a gluelike material (Figure 4.7). A continuum-based modeling of the adhesive is appropriate when the glue has a finite thickness. The macroscopic properties, such as stiffness and strength, of the adhesive material can be measured experimentally and used directly for modeling purposes. The adhesive material is generally more compliant than the surrounding material. The cohesive elements model the initial loading, the initiation of damage, and the propagation of damage leading to eventual failure in the material.

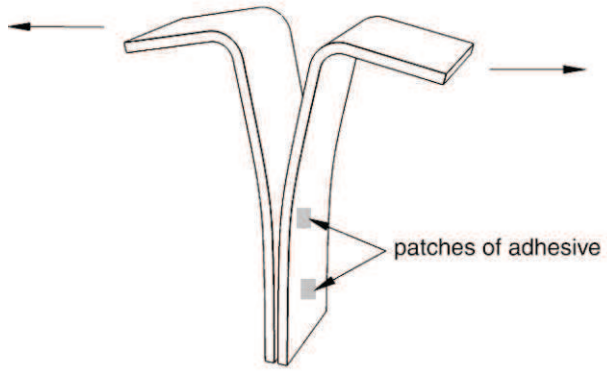

Fig. 4.7: Typical peel test using cohesive elements to model finite-thickness adhesives.

In three-dimensional problems, as used in this thesis work, the continuum-based constitutive model assumes one direct (through-thickness) strain, two transverse shear strains, and all (six) stress components to be active at a material point.

4.4.2 Traction-separation-based modeling

The modeling of bonded interfaces in composite materials often involves situations where the intermediate glue material is very thin and for all practical purposes may be considered to be of zero thickness (Figure 4.8). In this case, the macroscopic material properties are not relevant directly, and the analyst must resort to concepts derived from fracture mechanics, such as the amount of energy required to create new surfaces.

The cohesive elements model the initial loading, the initiation of damage, and the propagation of damage leading to eventual failure at the bonded interface. The behaviour of the interface prior to initiation of damage is often described as linear elastic in terms of a penalty stiffness that degrades under tensile and/or shear loading but is unaffected by pure compression.

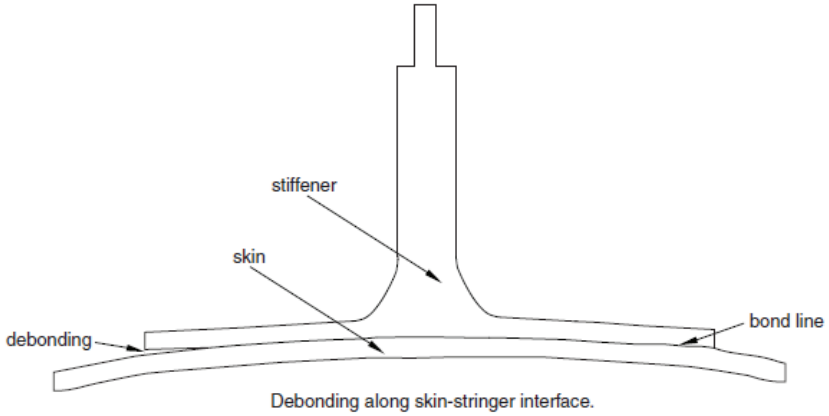

Fig. 4.8: Debonding along a skin-stringer interface: typical situation for Traction-separation-based modeling.

The cohesive elements may be used in areas of the model where cracks are expected to develop. However, the model need not have any crack to begin with. In fact, the precise locations (among all areas modeled with cohesive elements) where cracks initiate, as well as the evolution characteristics of such cracks, are determined as part of the solution. The cracks are restricted to propagate along the layer of cohesive elements and will not deflect into the surrounding material.

In three-dimensional problems, the traction-separation-based model assumes three components of separation: one normal to the interface and two parallel to it; and the corresponding stress components are assumed to be active at a material point.

4.4.3 Spatial representation of a cohesive element

Figure 4.9 demonstrates the key geometrical features that are used to define cohesive elements. The connectivity of cohesive elements is like that of continuum elements, but it is useful to think of cohesive elements as being composed of two faces separated by a thickness. The relative motion of the bottom and top faces measured along the thickness direction (local 3-direction for three-dimensional elements) represents opening or closing of the interface.

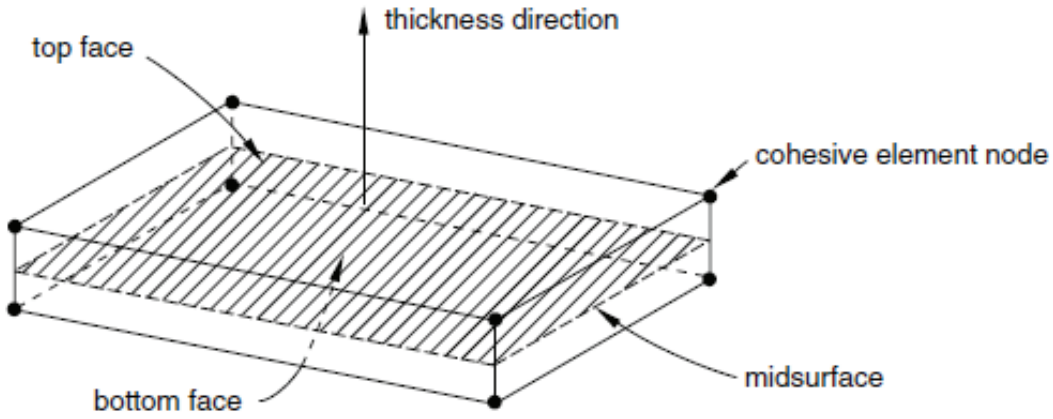

Fig. 4.9: Spatial representation of a three-dimensional cohesive element.

The relative change in position of the bottom and top faces measured in the plane orthogonal to the thickness direction quantifies the transverse shear behaviour of the cohesive element. Stretching and shearing of the mid surface of the element (the surface halfway between the bottom and top faces) are associated with membrane strains in the cohesive element; however, it is assumed that the cohesive elements do not generate any stresses in a purely membrane response. Figure 4.10 shows the different deformation modes of a cohesive element.

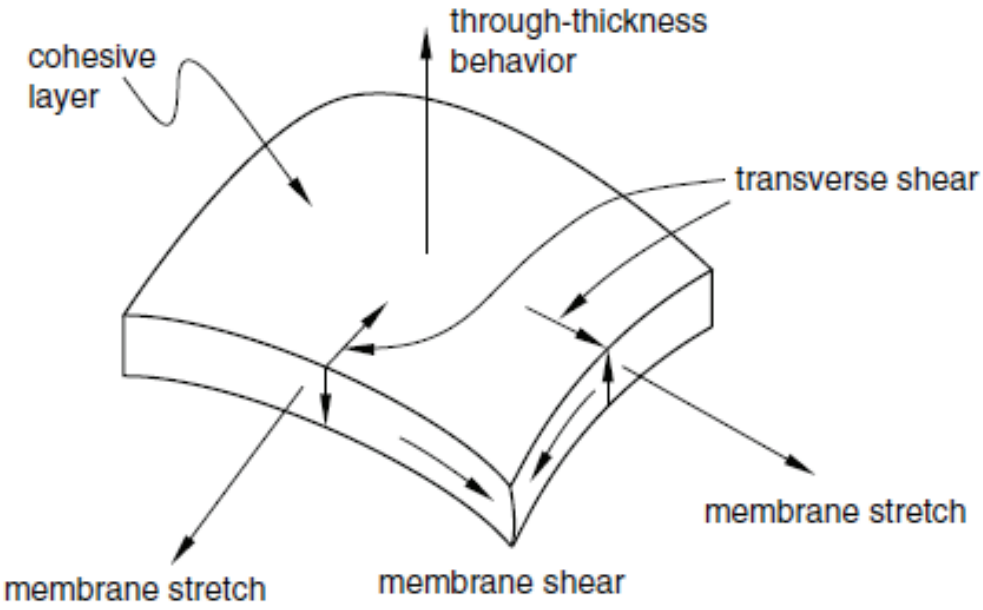

Fig. 4.10: Deformation modes of a cohesive element.

4.4.4 Naming convention in Abaqus

The cohesive elements used in Abaqus are named as follows:

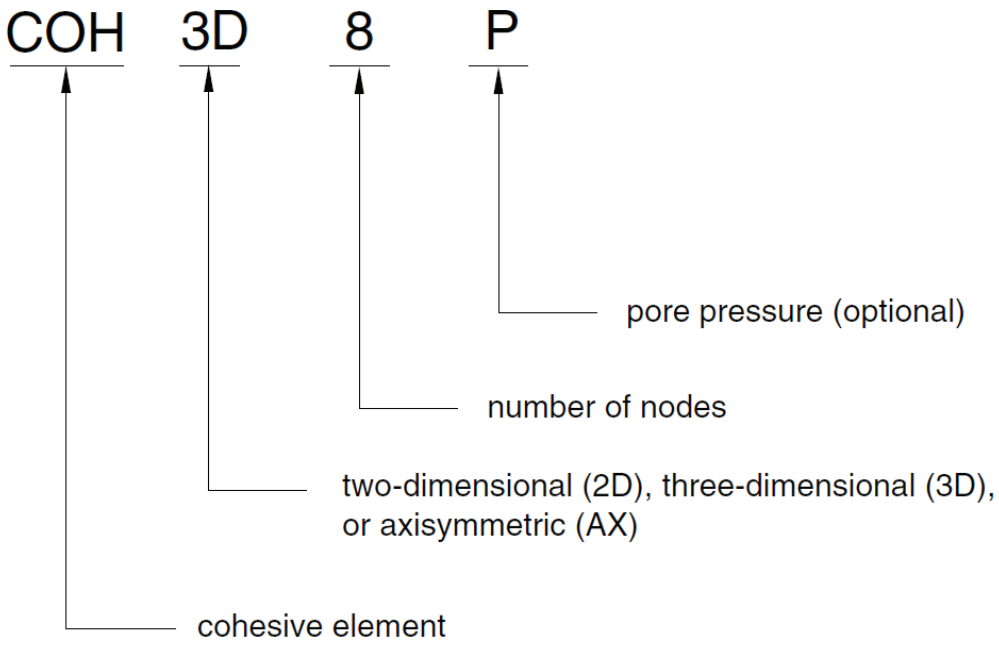

4.5 Modeling with cohesive elements

As written before, cohesive elements:

- are used to model adhesives between two components, each of which may be deformable or rigid;
- are used to model interfacial debonding using a cohesive zone framework;
- are used to model gaskets and/or small adhesive patches;
- can be connected to the adjacent components by sharing nodes, by using mesh tie constraints, or by using MPCs type TIE or PIN; and
- may interact with other components via contact for gasket applications.

In the next, the discussion is on the techniques that are available to discretize cohesive zones and assemble them in a model representing several components that are bonded to one another.

4.5.1 Discretizing cohesive zones using cohesive elements

The cohesive zone must be discretized with a single layer of cohesive elements through the thickness. If the cohesive zone represents an adhesive material with a finite thickness, the continuum macroscopic properties of this material can be used directly for modeling the constitutive response of the cohesive zone. Alternatively, if the cohesive zone represents an

infinitesimally thin layer of adhesive at a bonded interface, it may be more relevant to define the response of the interface directly in terms of the traction-separation law at the interface versus the relative motion across the interface.

4.5.2 Connections between cohesive elements and other components

At least one of either the top or the bottom face of the cohesive element must be constrained to another component. In most applications, it is appropriate to have both faces of the cohesive elements tied to neighboring components. If only one face of the cohesive element is constrained and the other face is free, the cohesive element exhibits one or (for three-dimensional elements) more singular modes of deformation due to the lack of membrane stiffness. The singular modes can propagate from one cohesive element to the adjacent one but can be suppressed by constraining the nodes on the side face at the end of a series of cohesive elements.

In some cases, it may be convenient and appropriate to have cohesive elements share nodes with the elements on the surfaces of the adjacent components. More generally, when the mesh in the cohesive zone is not matched to the mesh of the adjacent components, cohesive elements can be tied to other components.

4.5.3 Cohesive elements sharing nodes with other components

When the cohesive elements and their neighboring parts have matched meshes, it is straightforward to connect cohesive elements to other components in a model simply by sharing nodes (Figure 4.11).

When these elements are used as adhesives or to model debonding, this method can be used to obtain initial results from a model: more accurate local results (in the decohesion zone) would typically be obtained with the cohesive zone more refined than the elements of the surrounding components.

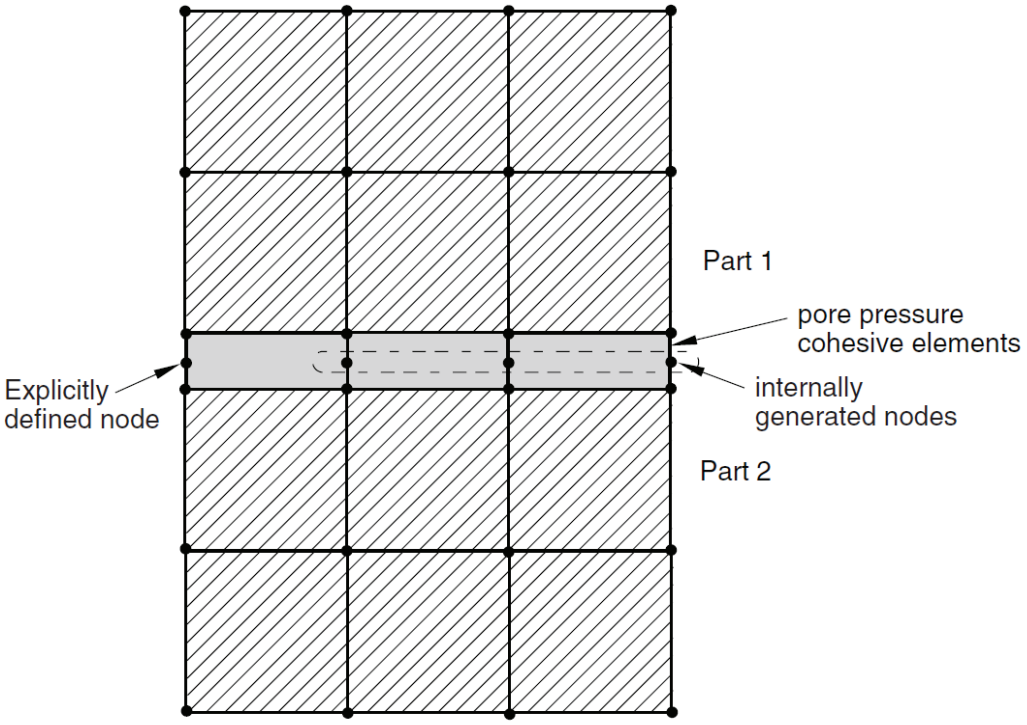

Fig. 4.11: Cohesive elements sharing nodes with other Abaqus elements.

4.5.4 Connections between cohesive elements and other components by using surface-based tie constraint

If the two neighboring parts do not have matched meshes, such as when the discretization level in the cohesive layer is different (typically finer) from the discretization level in

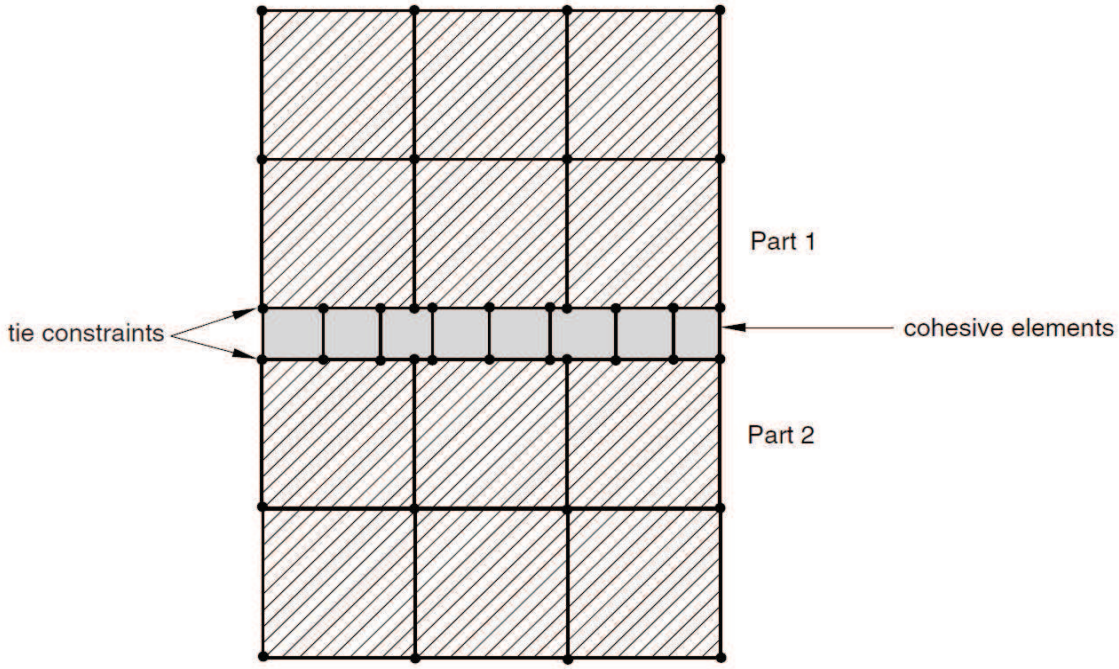

Fig. 4.12: Independent mesh with tie constraints.

the surrounding structures, the top and/or bottom surfaces of the cohesive layer can be tied to the surrounding structures using a tie constraint. Figure 4.12 shows an example in which a finer discretization is used for the cohesive layer than for the neighboring parts.

4.5.5 Using cohesive elements in large-displacement analyses

Cohesive elements can be used in large-displacement analyses. The assembly containing the cohesive elements can undergo finite displacement as well as finite rotation. This is the case of this work, where large displacement as well as finite rotation are implemented in the model.

4.5.6 Assigning a material behaviour to a cohesive element

Using cohesive element, we have to assign the name of a material definition to a particular element set. The constitutive behaviour for this element set is defined entirely by the constitutive thickness of the cohesive layer and the material properties referring to the same name. The constitutive behaviour of the cohesive elements can be defined either in terms of a material model provided in Abaqus or a user-defined material model When cohesive elements are used in applications involving a finite-thickness adhesive, any available material model in Abaqus, including material models for progressive damage, can be used.
For applications in which the behaviour of cohesive elements is defined directly in terms of traction versus separation, the response can be defined only in terms of a linear elastic relation (between the traction and the separation) along with progressive damage. To define the constitutive behaviour of cohesive elements, it is possible to assign the name of a material model to a particular element set through the section definition. The actual material model for a user-defined material model is defined in user subroutine UMAT in Abaqus/Standard.

4.5.7 Contact between surrounding components

Cohesive elements are used to bond two different components. Often the cohesive elements completely degrade in tension and/or shear because of the deformation. Subsequently, the components that are initially bonded together by cohesive elements may come into contact with each other. Approaches for modeling this kind of contact include the following:

- In certain situations, this kind of contact can be handled by the cohesive element itself. By default, cohesive elements retain their resistance to compression even if their resistance to other deformation modes is completely degraded. As a result, the cohesive elements resist interpenetration of the surrounding components even after the cohesive element has completely degraded in tension and/or shear. This approach works best when

the top and the bottom faces of the cohesive element do not displace tangentially by a significant amount relative to each other during the deformation. In other words, to model the situation described above, the deformation of the cohesive elements should be limited to “small sliding”.

- Another possible approach is to define contact between the surfaces of the surrounding components that could potentially come into contact and to delete the cohesive elements once they are completely damaged. Thus, contact is modeled throughout the analysis. This approach is not recommended if the geometric thickness of the cohesive elements in the model is very small or zero (the geometric thickness of the cohesive elements may be different from the constitutive thickness you specify while defining the section properties of the cohesive elements because contact will effectively cause nonphysical resistance to compression of the cohesive layer while the cohesive elements are still active. If frictional contact is modeled, there may also be nonphysical shearing forces.

This is the behaviour that will occur by default with the general contact algorithm (Figure 4.13 and 4.14).

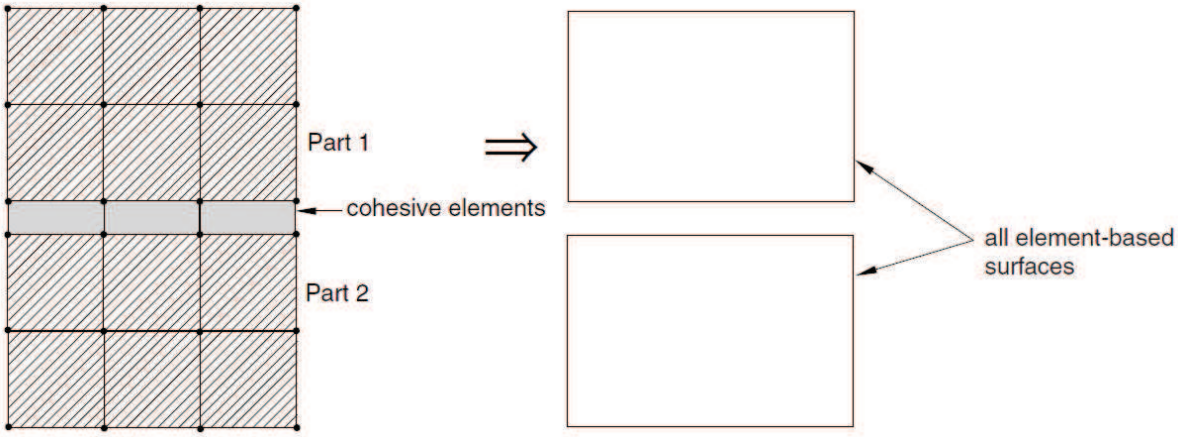

Fig. 4.13: Default surface when cohesive elements share nodes with surrounding elements.

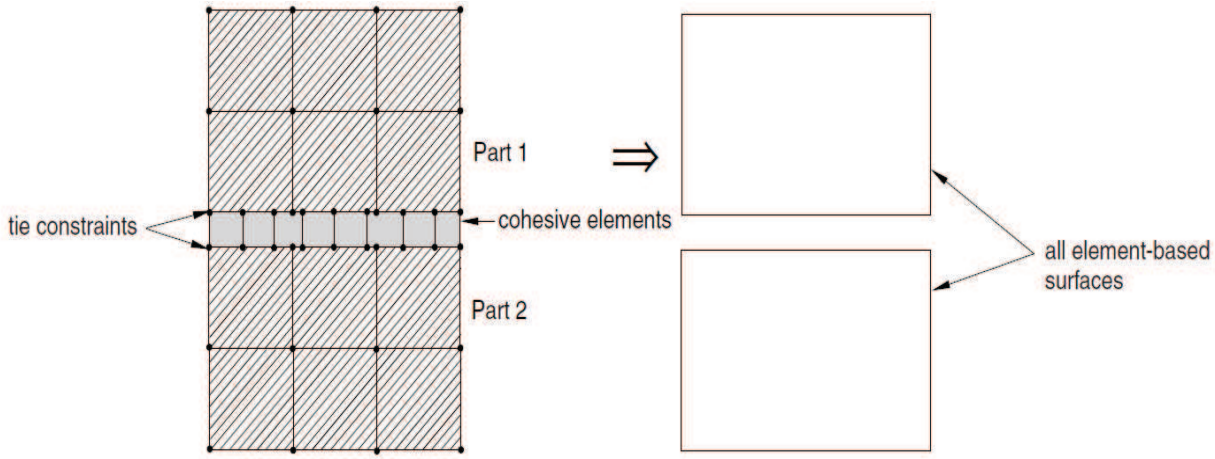

Fig. 4.14: Default surface when cohesive elements are tied to the surrounding elements.

4.6 Convergence issues in Abaqus/Standard

In many problems, cohesive elements are modeled as undergoing progressive damage leading to failure. The modeling of progressive damage involves softening in the material response, which is known to lead to convergence difficulties in an implicit solution procedure, such as in Abaqus/Standard. Convergence difficulties may also occur during unstable crack propagation, when the energy available is higher than the fracture toughness of the material. Several methods are available to help avoid these convergence problems, some of which are:

- **Using viscous regularization:** Abaqus/Standard provides a viscous regularization capability that helps in improving the convergence for these kinds of problems.
- **Using automatic stabilization:** Another approach to help convergence behaviour is the use of automatic stabilization, which is useful when a problem is unstable due to local instabilities. Generally, if sufficient viscous regularization is used (as measured by the viscosity coefficient, the use of the automatic stabilization technique is not necessary. In problems where a small amount or no viscous regularization is used, automatic stabilization will improve the convergence characteristics.
- **Using nondefault solution controls:** The use of nondefault solution controls and activation of the line search technique may be useful in improving the solution efficiency.

4.7 The constitutive response of cohesive elements using a continuum approach

The features described in this section are used to model cohesive elements using a continuum approach, which assumes that the cohesive zone contains material of finite thickness that can be modeled using the conventional material models in Abaqus. If the cohesive zone is

very thin and for all practical purposes may be considered to be of zero thickness, the constitutive response is commonly described in terms of a traction-separation law.

The constitutive response of cohesive elements modeled as a continuum:

- can be defined in terms of macroscopic material properties such as stiffness and strength using conventional material models;
- can be specified in terms of either a built-in material model or a user-defined material model; and
- can also include the effects of material damage and failure in a low-cycle fatigue analysis in Abaqus/Standard.

4.7.1 Behaviour of cohesive elements with conventional material models

The implementation of the conventional material models (including user-defined models) in Abaqus for cohesive elements is based on certain assumptions regarding the state of the deformation in the cohesive layer. Two different classes of problems are considered: modeling of an adhesive layer of finite thickness and modeling of gaskets.

Modeling of damage with cohesive elements for these classes of problems can be carried out in both Abaqus/Standard and Abaqus/Explicit. You may need to alter the damage model for an adhesive material to account for the fact that the failure of an adhesive bond may occur at the interface between the adhesive and the adherent rather than within the adhesive material. When used with conventional material models in Abaqus, cohesive elements use true stress and strain measures. When used with a material model that is based on a traction-separation description, cohesive elements use nominal stress and strain measures.

4.7.2 Modeling of an adhesive layer of finite thickness

For adhesive layers with finite thickness it is assumed that the cohesive layer is subjected to only one direct component of strain, which is the through-thickness strain, and to two transverse shear strain components. The other two direct components of the strain (the direct membrane strains) and the in-plane (membrane) shear strain are assumed to be zero for the constitutive calculations. More specifically, the through-thickness and the transverse shear strains are computed from the element kinematics. However, the membrane strains are not computed based on the element kinematics; they are simply assumed to be zero for the constitutive calculations. These assumptions are appropriate in situations where a relatively thin and compliant layer of adhesive bonds two relatively rigid (compared to the adhesive) parts. The above kinematic assumptions are approximately correct everywhere inside the cohesive layer except around its outer edges. An additional linear elastic transverse shear

behaviour can be defined to provide more stability to cohesive elements, particularly after damage has occurred. The transverse shear behaviour is assumed to be independent of the regular material response and does not undergo any damage.

4.8 The constitutive response of cohesive elements using a traction-separation description

The features described in this section are primarily intended for bonded interfaces where the interface thickness is negligibly small. In such cases it may be straightforward to define the constitutive response of the cohesive layer directly in terms of traction versus separation. If the interface adhesive layer has a finite thickness and macroscopic properties (such as stiffness and strength) of the adhesive material are available, it may be more appropriate to model the response using conventional material models.

Cohesive behaviour defined directly in terms of a traction-separation law:

- can be used to model the delamination at interfaces in composites directly in terms of traction versus separation;
- allows specification of material data such as the fracture energy as a function of the ratio of normal to shear deformation (mode mix) at the interface;
- assumes a linear elastic traction-separation law prior to damage;
- assumes that failure of the elements is characterized by progressive degradation of the material stiffness, which is driven by a damage process;
- allows multiple damage mechanisms; and
- can be used with user subroutine UMAT in Abaqus/Standard® to specify user-defined traction-separation laws.

4.8.1 Constitutive response in terms of traction-separation laws

When defining the section behaviour of the cohesive elements, we have to choose a traction-separation response to define the constitutive response of the cohesive element directly in terms of traction versus separation.

4.8.2 Linear elastic traction-separation behaviour

The available traction-separation model in Abaqus assumes initially linear elastic behaviour followed by the initiation and evolution of damage. The elastic behaviour is written in terms of an elastic constitutive matrix that relates the nominal stresses to the nominal strains across the interface. The nominal stresses are the force components divided by the original area at

each integration point, while the nominal strains are the separations divided by the original thickness at each integration point. The default value of the original constitutive thickness is 1.0 if traction-separation response is specified, which ensures that the nominal strain is equal to the separation (i.e., relative displacements of the top and bottom faces). The constitutive thickness used for traction-separation response is typically different from the geometric thickness (which is typically close or equal to zero).

The nominal traction stress vector, **t**, consists of three components: t_n, t_s, and (in three-dimensional problems) t_t, which represent the normal (along the local 3-direction in three dimensions) and the two shear tractions (along the local 1- and 2-directions in three dimensions), respectively. The corresponding separations are denoted by δ_n, δ_s, and δ_t. Denoting by the original thickness of the cohesive element, the nominal strains can be defined as:

$$\varepsilon_n = \frac{\delta_n}{T_0};\ \varepsilon_s = \frac{\delta_s}{T_0};\ \varepsilon_t = \frac{\delta_t}{T_0} \tag{4.8}$$

The elastic behaviour can then be written as:

$$\mathbf{t} = \begin{Bmatrix} t_n \\ t_s \\ t_t \end{Bmatrix} = \begin{bmatrix} E_{nn} & E_{ns} & E_{nt} \\ E_{ns} & E_{ss} & E_{st} \\ E_{nt} & E_{st} & E_{tt} \end{bmatrix} \begin{Bmatrix} \varepsilon_n \\ \varepsilon_s \\ \varepsilon_t \end{Bmatrix} = \mathbf{E\varepsilon}. \tag{4.9}$$

The elasticity matrix provides fully coupled behaviour between all components of the traction vector and separation vector and can depend on temperature and/or field variables. Set the off-diagonal terms in the elasticity matrix to zero if uncoupled behaviour between the normal and shear components is desired.

4.8.3 Interpretation of material properties

The material parameters, such as the interfacial elastic stiffness, for a traction-separation model can be better understood by studying the equation that represents the displacement of a truss of length L, elastic stiffness E, and original area A, due to an axial load P:

$$\delta = \frac{PL}{AE} \tag{4.10}$$

This equation can be rewritten as:

$$\delta = \frac{S}{K} \quad 4.11$$

where S=P/A is the nominal stress and K=E/L is the stiffness that relates the nominal stress to the displacement. Likewise, the total mass of the truss, assuming a density ρ, is given by

$$M = \rho AL = \bar{\rho} A. \quad 4.12$$

The above equations suggest that the actual length L may be replaced with 1.0 (to ensure that the strain is the same as the displacement) if the stiffness and the density are appropriately reinterpreted. In particular, the stiffness is $K = (E/L)$ and the density is $\overline{\rho} = (\rho L)$, where the true length of the truss is used in these equations. The density represents mass per unit area instead of mass per unit volume. These ideas can be carried over to a cohesive layer of initial thickness T_c. If the adhesive material has stiffness E_a and density ρ_c, the stiffness of the interface (relating the nominal traction to the nominal strain) is given by $E_c = (E_a/T_c)T_0$ and the density of the interface is given by $\overline{\rho_c} = (\rho_c T_c)$. As discussed earlier, the default choice of the constitutive thickness T_0 for modeling the response in terms of traction versus separation is 1.0 regardless of the actual thickness of the cohesive layer. With this choice, the nominal strains are equal to the corresponding separations. When the constitutive thickness of the cohesive layer is "artificially" set to 1.0, ideally you should specify T_c and $\overline{\rho_c}$ (if needed) as the material stiffness and density, respectively, as calculated with the true thickness of the cohesive layer.

The above formulae provide a recipe for estimating the parameters required for modeling the traction-separation behaviour of an interface in terms of the material properties of the bulk adhesive material. As the thickness of the interface layer tends to zero, the above equations imply that the stiffness, E_c, tends to infinity and the density, $\overline{\rho_c}$, tends to zero. This stiffness is often chosen as a penalty parameter. A very large penalty may result in ill-conditioning of the element operator in Abaqus/Standard.

4.8.4 Damage modeling

Abaqus/Standard allows modeling of progressive damage and failure in cohesive layers whose response is defined in terms of traction-separation. Damage of the traction-separation response is defined within the same general framework used for conventional materials. This general framework allows the combination of several damage mechanisms acting

simultaneously on the same material. Each failure mechanism consists of three ingredients: a damage initiation criterion, a damage evolution law, and a choice of element removal (or deletion) upon reaching a completely damaged state. While this general framework is the same for traction-separation response and conventional materials, many details of how the various ingredients are defined are different.

Therefore, the details of damage modeling for traction-separation response are presented below. The initial response of the cohesive element is assumed to be linear as discussed above. However, once a damage initiation criterion is met, material damage can occur according to a user-defined damage evolution law. Figure 4.15 shows a typical traction-separation response with a failure mechanism. If the damage initiation criterion is specified without a corresponding damage evolution model, Abaqus will evaluate the damage initiation criterion for output purposes only; there is no effect on the response of the cohesive element (i.e., no damage will occur). The cohesive layer does not undergo damage under pure compression.

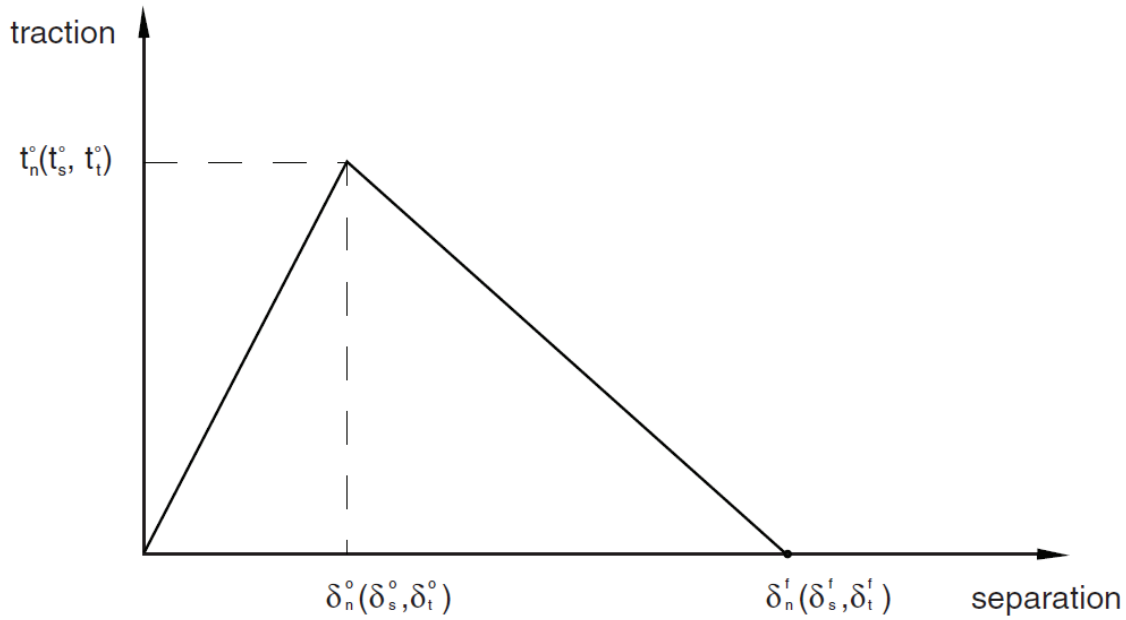

Fig. 4.15: Typical traction-separation response.

4.8.5 Damage initiation

As the name implies, damage initiation refers to the beginning of degradation of the response of a material point. The process of degradation begins when the stresses and/or strains satisfy certain damage initiation criteria that we specify. Several damage initiation criteria are available and are discussed below. Each damage initiation criterion also has an output

variable associated with it to indicate whether the criterion is met. A value of 1 or higher indicates that the initiation criterion has been met. Damage initiation criteria that do not have an associated evolution law affect only output. Thus, it's possible to use these criteria to evaluate the propensity of the material to undergo damage without actually modeling the damage process (i.e., without actually specifying damage evolution).

In the next expression written below, t_n^0, t_s^0, and t_t^0, represent the peak values of the nominal stress when the deformation is either purely normal to the interface or purely in the first or the second shear direction, respectively. Likewise, ε_n^0, ε_s^0, and ε_t^0, represent the peak values of the nominal strain when the deformation is either purely normal to the interface or purely in the first or the second shear direction, respectively. With the initial constitutive thickness T_0=1, the nominal strain components are equal to the respective components of the relative displacement δ_n^0, δ_n^0, and δ_n^0, between the top and bottom of the cohesive layer. The symbol <> used below represents the Macaulay bracket with the usual interpretation. The Macaulay brackets are used to signify that a pure compressive deformation or stress state does not initiate damage.

The damage initiation criteria are as follow:

- **Maximum nominal stress criterion:** Damage is assumed to initiate when the maximum nominal stress ratio (as defined in the expression below) reaches a value of one. This criterion can be represented as:

$$max\left\{\frac{\langle t_n\rangle}{t_n^0}, \frac{t_s}{t_s^0}, \frac{t_t}{t_t^0}\right\} = 1 \qquad 4.13$$

- **Maximum nominal strain criterion:** Damage is assumed to initiate when the maximum nominal strain ratio (as defined in the expression below) reaches a value of one. This criterion can be represented as:

$$max\left\{\frac{\langle \varepsilon_n\rangle}{\varepsilon_n^0}, \frac{\varepsilon_s}{\varepsilon_s^0}, \frac{\varepsilon_t}{\varepsilon_t^0}\right\} = 1 \qquad 4.14$$

- **Quadratic nominal stress criterion:** Damage is assumed to initiate when a quadratic interaction function involving the nominal stress ratios (as defined in the expression below) reaches a value of one. This criterion can be represented as:

$$\left\{\frac{\langle t_n \rangle}{t_n^0}\right\}^2 + \left\{\frac{t_s}{t_s^0}\right\}^2 + \left\{\frac{t_t}{t_t^0}\right\}^2 = 1 \qquad 4.15$$

- **Quadratic nominal strain criterion:** Damage is assumed to initiate when a quadratic interaction function involving the nominal strain ratios (as defined in the expression below) reaches a value of one. This criterion can be represented as:

$$\left\{\frac{\langle \varepsilon_n \rangle}{\varepsilon_n^0}\right\}^2 + \left\{\frac{\varepsilon_s}{\varepsilon_s^0}\right\}^2 + \left\{\frac{\varepsilon_t}{\varepsilon_t^0}\right\}^2 = 1 \qquad 4.16$$

4.8.6 Damage evolution

The damage evolution law describes the rate at which the material stiffness is degraded once the corresponding initiation criterion is reached. Conceptually, similar ideas apply for describing damage evolution in cohesive elements with a constitutive response that is described in terms of traction versus separation; however, many details are different. A scalar damage variable, D, represents the overall damage in the material and captures the combined effects of all the active mechanisms. It initially has a value of 0. If damage evolution is modeled, D monotonically evolves from 0 to 1 upon further loading after the initiation of damage. The stress components of the traction-separation model are affected by the damage according to:

$$t_n = \begin{cases} (1-D)\bar{t}_n^0, & \bar{t}_n \geq 0 \\ \bar{t}_n & otherwise\ (no\ damage\ to\ compressive\ stiffness); \end{cases}$$

$$t_s = (1-D)\bar{t}_s, \qquad 4.17$$

$$t_t = (1-D)\bar{t}_t,$$

where $\bar{t}_n^0$, $\bar{t}_s$ and $\bar{t}_t$ are the stress components predicted by the elastic traction-separation behaviour for the current strains without damage.

To describe the evolution of damage under a combination of normal and shear deformation across the interface, it is useful to introduce an effective displacement [Camanho and Davila, 2002] defined as:

$$\delta_m = \sqrt{\langle \delta_n \rangle^2 + \delta_s^2 + \delta_t^2} \qquad 4.18$$

4.8.7 Mixed-mode definition

The mixed-mode of the deformation fields in the cohesive zone quantify the relative proportions of normal and shear deformation. Abaqus uses two measures of mixed-mode, one based on energies and the other based on tractions. We can choose one of these measures when we specify the mode dependence of the damage evolution process. Denoting by G_n, G_s, and G_t the work done by the tractions and their conjugate relative displacements in the normal, first, and second shear directions, respectively, and defining $G_T = G_n + G_s + G_t$, the mode-mix definitions based on energies are as follows:

$$m_1 = \frac{G_n}{G_T} \qquad m_2 = \frac{G_s}{G_T} \qquad m_3 = \frac{G_t}{G_T} \qquad 4.19$$

Clearly, only two of the three quantities defined above are independent. It is also useful to define the $G_S = G_s + G_t$ quantity to denote the portion of the total work done by the shear traction and the corresponding relative displacement components. As written later, Abaqus requires that you specify material properties related to damage evolution as functions of $m_2 + m_3$ ($= G_S / G_T$) (or, equivalently, $1 - m_1$) and $m_3 / (m_2 + m_3)$ ($= G_t / G_S$).

The corresponding definitions of the mode mix based on traction components are given by

$$\varphi_1 = \left(\frac{2}{\pi}\right) \tan^{-1}\left(\frac{\tau}{\langle t_n \rangle}\right)$$

$$\varphi_2 = \left(\frac{2}{\pi}\right) \tan^{-1}\left(\frac{t_t}{t_s}\right) \qquad 4.20$$

where $\tau = \sqrt{\tau_s^2 + \tau_t^2}$ is a measure of the effective shear traction. Figure 4.16 illustrates the angular measures used in the above definition (before they are normalized by the factor $2/\pi$).

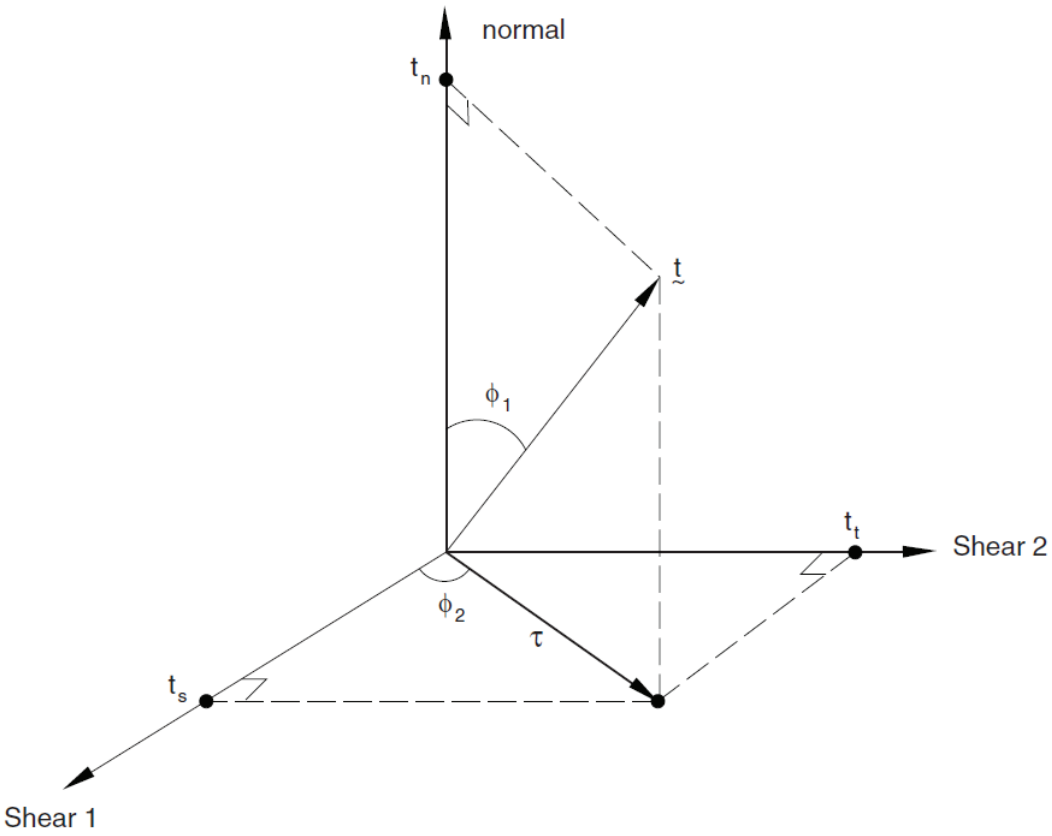

Fig. 4.16: Mixed-mode measures based on tractions.

The mixed-mode ratios defined in terms of energies and tractions can be quite different in general. The following example illustrates this point. In terms of energies a deformation in the purely normal direction is one for which $G_n \neq 0$ and $G_s = G_t = 0$, irrespective of the values of the normal and the shear tractions. In particular, for a material with coupled traction-separation behaviour both the normal and shear tractions may be nonzero for a deformation in the purely normal direction. For this case, the definition of mixed-mode based on energies would indicate a purely normal deformation, while the definition based on tractions would suggest a mix of both normal and shear deformation.

There are two components to the definition of the evolution of damage. The first component involves specifying either the effective displacement at complete failure, δ_m^f, relative to the effective displacement at the initiation of damage, δ_m^o; or the energy dissipated due to failure, G^C (Figure 4.17). The second component to the definition of damage evolution is the specification of the nature of the evolution of the damage variable, D, between initiation of damage and final failure. This can be done by either defining linear or exponential softening laws or specifying D directly as a tabular function of the effective displacement relative to the effective displacement at damage initiation. The material data described above will in general be functions of the mixed-mode, temperature, and/or field variables. Figure 4.18 is

a schematic representation of the dependence of damage initiation and evolution on the mode mix, for a traction-separation response with isotropic shear behaviour.

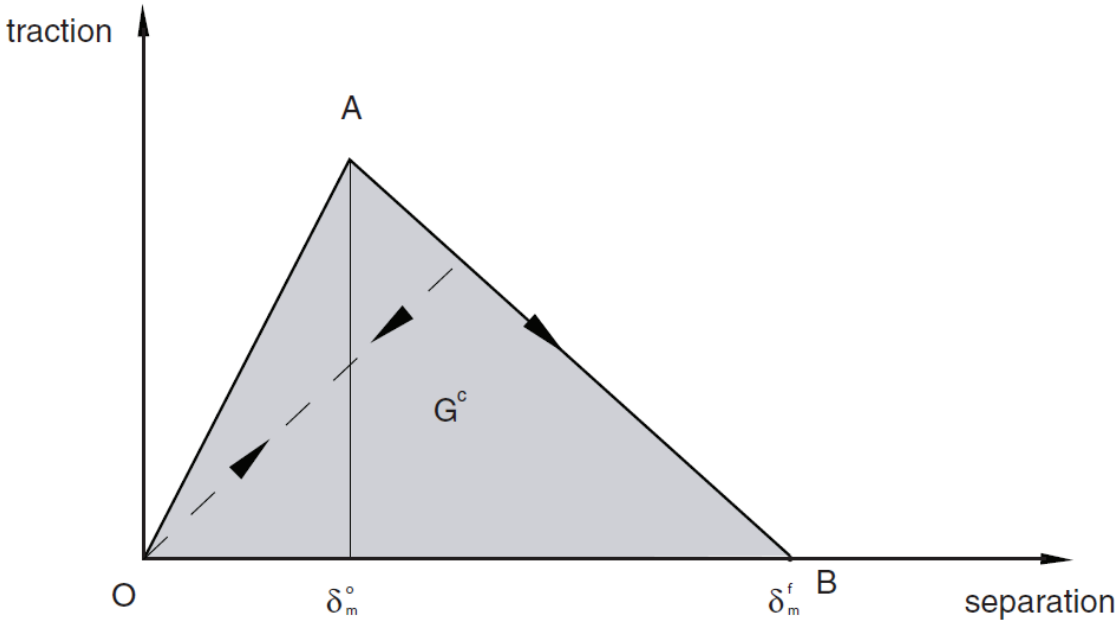

Fig. 4.17: Linear damage evolution

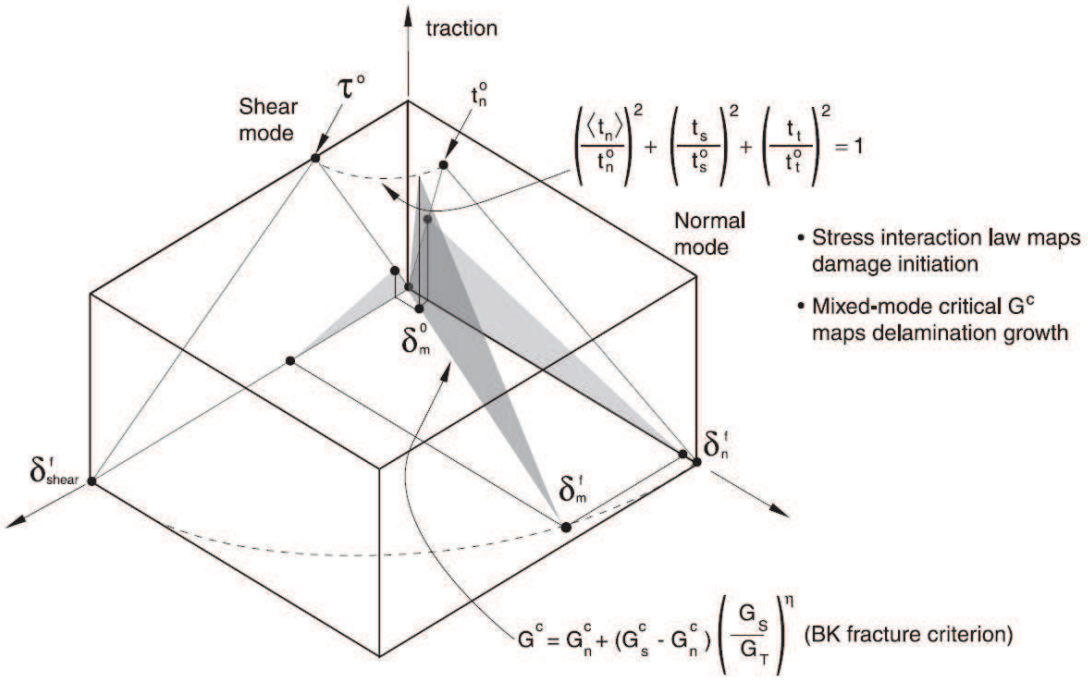

Fig. 4.18: Illustration of mixed-mode response in cohesive elements.

The figure 4.18 shows the traction on the vertical axis and the magnitudes of the normal and the shear separations along the two horizontal axes. The unshaded triangles in the two

vertical coordinate planes represent the response under pure normal and pure shear deformation, respectively. All intermediate vertical planes (that contain the vertical axis) represent the damage response under mixed-mode conditions with different mode mixes. The dependence of the damage evolution data on the mode mix can be defined either in tabular form or, in the case of an energy-based definition, analytically. The manner in which the damage evolution data are specified as a function of the mixed-mode is discussed later in this chapter.

Unloading subsequent to damage initiation is always assumed to occur linearly toward the origin of the traction-separation plane, as shown in Figure 4.17. Reloading subsequent to unloading also occurs along the same linear path until the softening envelope (line AB) is reached. Once the softening envelope is reached, further reloading follows this envelope as indicated by the arrow in Figure 4.17.

4.8.8 Evolution based on effective displacement

The quantity δ_m^f - δ_m^o (i.e., the effective displacement at complete failure, δ_m^f, relative to the effective displacement at damage initiation, δ_m^o, as shown in Figure 4.17) can be specified as a tabular function of the mixed-mode, temperature, and/or field variables. In addition, it is possible to choose either a linear or an exponential softening law that defines the detailed evolution (between initiation and complete failure) of the damage variable, D, as a function of the effective displacement beyond damage initiation. Alternatively, instead of using linear or exponential softening, we can specify the damage variable, D, directly as a tabular function of the effective displacement after the initiation of damage, $\delta_m - \delta_m^o$, mixed-mode, temperature, and/or field variables.

- **Linear damage evolution:** For linear softening (Figure 4.17) Abaqus uses an evolution of the damage variable, D, that reduces (in the case of damage evolution under a constant mixed-mode, temperature, and field variables) to the expression proposed by [Camanho and Davila, 2002], namely:

$$D = \frac{\delta_m^f(\delta_m^{max} - \delta_m^o)}{\delta_m^{max}\left(\delta_m^f - \delta_m^o\right)} \qquad 4.21$$

In the preceding expression, δ_m^{max} refers to the maximum value of the effective displacement attained during the loading history. The assumption of a constant mixed-mode

at a material point between initiation of damage and final failure is customary for problems involving monotonic damage (or monotonic fracture).

- **Exponential damage evolution:** For exponential softening (Figure 4.19) Abaqus uses an evolution of the damage variable, D, that reduces (in the case of damage evolution under a constant mode mix, temperature, and field variables) to:

$$D = 1 - \left\{\frac{\delta_m^o}{\delta_m^{max}}\right\}\left\{1 - \frac{1 - exp\left(-\alpha\left(\frac{\delta_m^{max} - \delta_m^o}{\delta_m^f - \delta_m^o}\right)\right)}{1 - exp(-\alpha)}\right\} \qquad 4.22$$

In the expression above α is a non-dimensional material parameter that defines the rate of damage evolution and *exp(x)* is the exponential function.

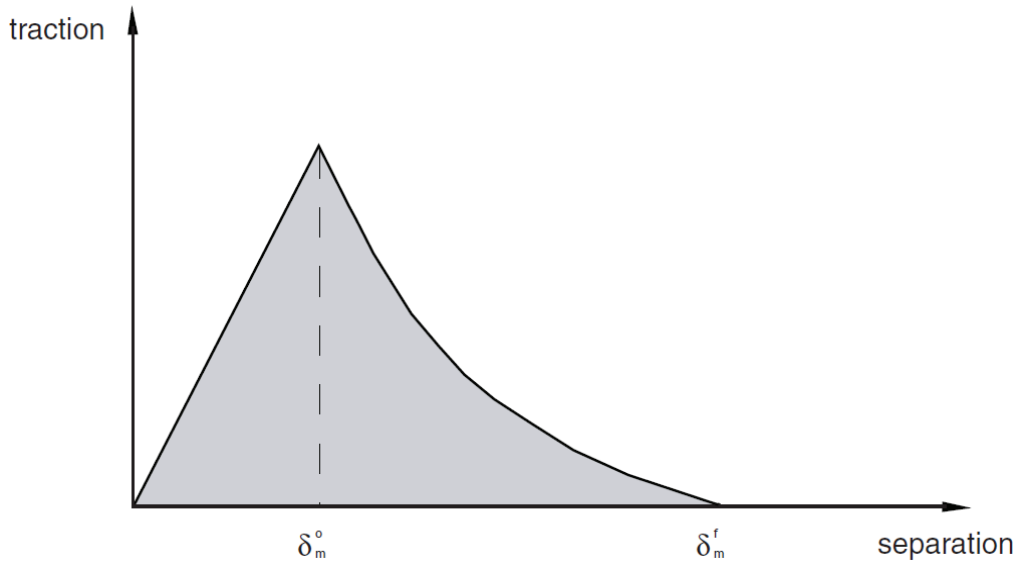

Fig. 4.19: Exponential damage evolution

- **Tabular damage evolution:** Abaqus permits, for tabular softening, the definition of the evolution of D directly in tabular form. D must be specified as a function of the effective displacement relative to the effective displacement at initiation, mixed-mode, temperature, and/or field variables.

4.8.9 Evolution based on energy

Damage evolution can be defined based on the energy that is dissipated as a result of the damage process, also called the fracture energy. The fracture energy is equal to the area under the traction-separation curve (Figure 4.17). The fracture energy can be written as a material property and we can choose either a linear or an exponential softening behaviour. Abaqus ensures that the area under the linear or the exponential damaged response is equal to the fracture energy.

The dependence of the fracture energy on the mixed-mode can be specified either directly in tabular form or by using analytical forms as described below. When the analytical forms are used, the mixed-mode ratio is assumed to be defined in terms of energies. Below are written the different forms of possible evolution based on energy:

- **Tabular form:** The simplest way to define the dependence of the fracture energy is to specify it directly as a function of the mixed-mode in tabular form.
- **Power law form:** The dependence of the fracture energy on the mixed-mode can be defined based on a power law fracture criterion. The power law criterion states that failure under mixed-mode conditions is governed by a power law interaction of the energies required to cause failure in the individual (normal and two shear) modes. It is given by:

$$\left\{\frac{G_n}{G_n^C}\right\}^{\alpha} + \left\{\frac{G_s}{G_s^C}\right\}^{\alpha} + \left\{\frac{G_t}{G_t^C}\right\}^{\alpha} = 1 \qquad 4.23$$

The mixed-mode fracture energy $G^C = G_T$ when the above condition is satisfied. In other words,

$$G^C = 1/\left(\left\{\frac{m_1}{G_n^C}\right\}^{\alpha} + \left\{\frac{m_2}{G_s^C}\right\}^{\alpha} + \left\{\frac{m_3}{G_t^C}\right\}^{\alpha}\right)^{\frac{1}{\alpha}} \qquad 4.24$$

We have only to specify the quantities G_n^C, G_s^C and G_t^C, which refer to the critical fracture energies required to cause failure in the normal, the first, and the second shear directions, respectively.

- **Benzeggagh-Kenane (BK) form**: The Benzeggagh-Kenane fracture criterion [Benzeggagh and Kenane, 1996] is particularly useful when the critical fracture energies

during deformation purely along the first and the second shear directions are the same, i.e. $G_s^C = G_t^C$. It is given by

$$G_n^C + (G_s^C + G_t^C)\left\{\frac{G_S}{G_T}\right\}^{\eta} = G^C \qquad 4.25$$

where $G_S = G_s + G_t$, $G_T = G_n + G_S$, and η is a material parameter. The inputs are: G_n^C, G_s^C, and η.

- **Linear damage evolution:** For linear softening (Figure 4.17) Abaqus uses an evolution of the damage variable, D, that reduces to

$$D = \frac{\delta_m^f(\delta_m^{max} - \delta_m^o)}{\delta_m^{max}(\delta_m^f - \delta_m^o)} \qquad 4.26$$

where $\delta_m^f = 2G^C/T_{eff}^o$ with T_{eff}^o as the effective traction at damage initiation. δ_m^{max} refers to the maximum value of the effective displacement attained during the loading history.

- **Exponential damage evolution:** For exponential softening Abaqus uses an evolution of the damage variable, D, that reduces to:

$$D = \int_{\delta_m^o}^{\delta_m^f} \frac{T_{eff}\,d\delta}{G^c - G_o} \qquad 4.27$$

In the expression above T_{eff} and δ are the effective traction and displacement, respectively. G_o is the elastic energy at damage initiation. In this case the traction might not drop immediately after damage initiation, which is different from what is seen in Figure 4.19.

4.9 Viscous regularization in Abaqus/Standard

Material models exhibiting softening behaviour and stiffness degradation often lead to severe convergence difficulties in implicit analysis programs, such as Abaqus/Standard. A common technique to overcome some of these convergence difficulties is the use of viscous regularization of the constitutive equations, which causes the tangent stiffness matrix of the softening material to be positive for sufficiently small time increments.

The traction-separation laws can be regularized in Abaqus/Standard using viscosity by permitting stresses to be outside the limits set by the traction-separation law. The

regularization process involves the use of a viscous stiffness degradation variable, D_v, which is defined by the evolution equation:

$$\dot{D}_v = \frac{1}{\mu}(D - D_v) \tag{4.28}$$

where μ is the viscosity parameter representing the relaxation time of the viscous system and D is the degradation variable evaluated in the inviscid backbone model. The damaged response of the viscous material is given as

$$\mathbf{t} = (1 - D_v)\bar{\mathbf{t}} \tag{4.29}$$

Using viscous regularization with a small value of the viscosity parameter (small compared to the characteristic time increment) usually, helps improve the rate of convergence of the model in the softening regime, without compromising results. The basic idea is that the solution of the viscous system relaxes to that of the inviscid case as $\mathbf{t}/\mu \to \infty$, where $\mathbf{t}$ represents time. We can specify the value of the viscosity parameter as part of the section controls definition. If the viscosity parameter is different from zero, output results of the stiffness degradation refer to the viscous value, D_v. The default value of the viscosity parameter is zero so that no viscous regularization is performed.

The approximate amount of energy associated with viscous regularization over the whole model or over an element set is available using output variable ALLCD.

CHAP. 5: TRACTION AND BENDING LAMINATE TESTS WITH ABAQUS

5.1 Introduction

In this chapter, some CFRP laminates, with different lamina orientations, are implemented with the Abaqus software simulation. Numerical results are compared with analytical calculations or another software simulation like ANSYS. Simulations consist in:

- traction of a $[0°/90°]_s$ laminate;
- traction of a $[45°/-45°]_s$ laminate;
- traction of a $[0°/90°]_s$ laminate with a hole;
- bending of a [0°/90°/0°/90°/0°/90°/0°] laminate (NAFEMS R0031).

The laminate with a hole is also compared for the solution convergence with another software, as written before. Data, for each type of test, are:

- laminate dimensions;
- laminate type;
- material used;
- loads and boundary conditions;
- element type and mesh used for the simulation;
- deformation;
- expected analytical results;
- numerical results;
- results comparison.

5.2 $[0°/90°]_s$ laminate

5.2.1 Laminate dimensions

Fig. 5.1 shows the laminate, a simple 100 x 100 mm square, with t=0,15 mm of laminae thickness.

5.2.2 Laminate model

As we can see in Fig. 5.2, laminate is made of 4 symmetric thin layer oriented at 0° and 90°. On the right fig. 5.2 shows a vertical section of the laminate with direction 1 as x axes, direction 2 as y axes, and direction 3 as z axes, wiz the stack direction of the laminate.

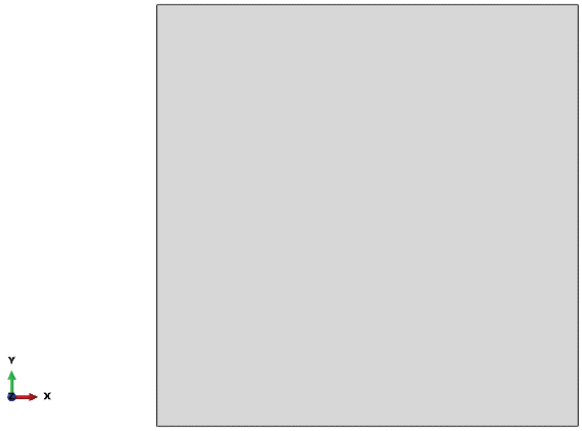

Fig. 5.1: $[0°/90°]_s$ laminate

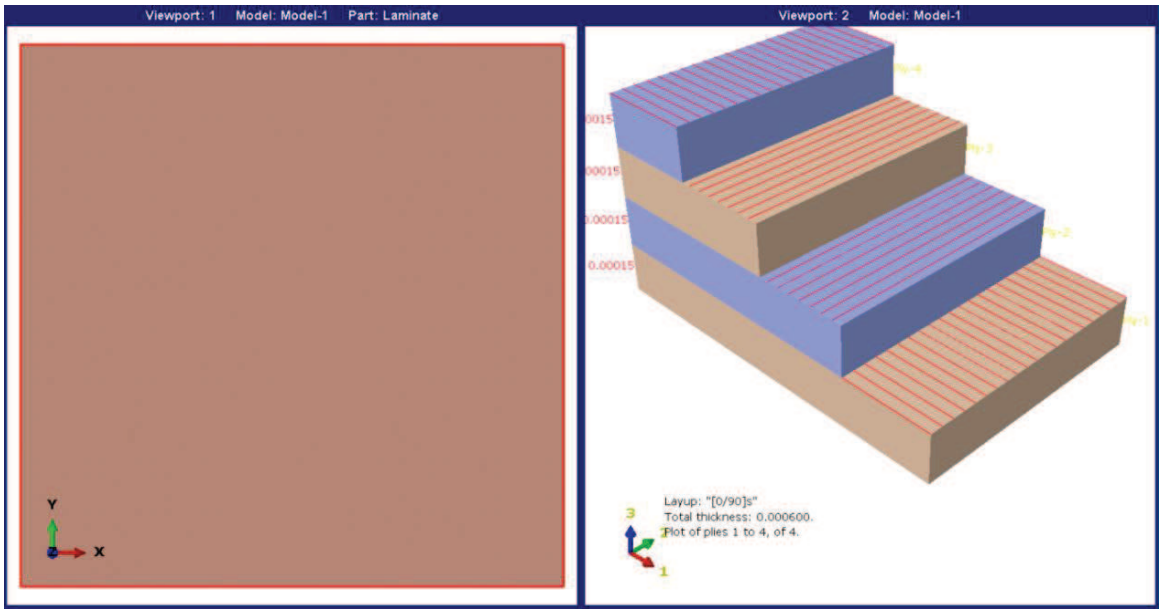

Fig. 5.2: Laminate model and relative section

5.2.3 Material properties

Laminae are made of Graphite/Epoxy material, which properties are in table 5.1:

E_1=155,0 GPa	ν_{12}=0,248	G_{12}=4,40 GPa	α_1=–0,018x10^{-6} /°C
E_2=12,10 GPa	ν_{13}=0,248	G_{13}=4,40 GPa	α_2=24,3x10^{-6}/°C
E_3=12,10 GPa	ν_{23}=0,458	G_{23}=3,20 GPa	α_3=24,3x10^{-6}/°C

Table 5.1: Material properties

5.2.4 Boundary conditions and loads

In fig. 5.3 we can see loads and boundary conditions used for the simulation. The vertical left zone is pinned, in other words, all the displacements are locked (U1=U2=U3=0); on the upper and lower side, displacement in y direction and rotations about x and z directions are inhibited (U2=UR1=UR3=0); on the right side we impose a constant displacement of U1=1 mm in the positive direction of x axes.

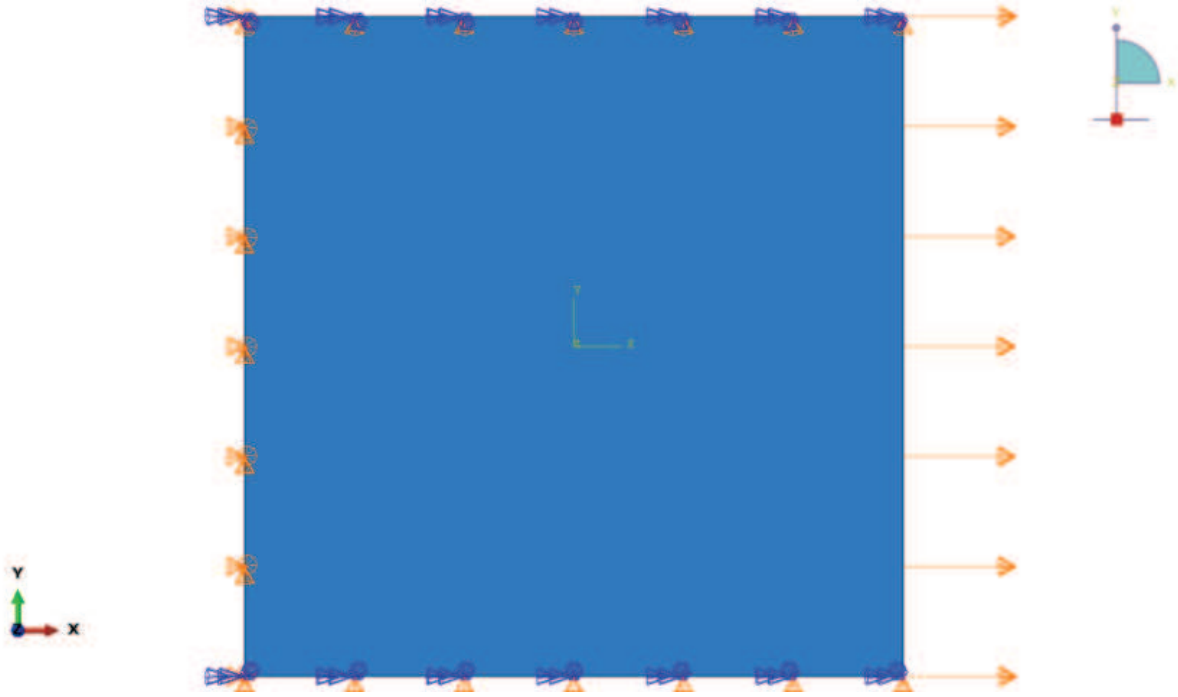

Fig. 5.3: Boundary conditions and loads

5.2.5 Element type and mesh

Element type used for the simulation is a Shell element (S8R) with 8 nodes. In Abaqus, Shell elements are used to model structures in which one dimension is significantly smaller than the other two dimensions; in this case, the thickness t = 0,6 mm respect to the width and the length of the model (100 x 100 mm). Conventional shell elements use this condition to discretize the body by the 2D geometry at a reference surface (Fig. 5.4). In this case the thickness is defined through the section property definition. Conventional shell elements have displacement and rotational degrees of freedom.

In contrast, continuum shell elements discretize an entire three-dimensional body. The thickness is determined from the element nodal geometry. Continuum shell elements have only displacement degrees of freedom. From a modeling point of view continuum shell elements look like three-dimensional continuum solids, but their kinematic and constitutive behavior is similar to conventional shell elements.

In this simulation, due to model geometry, conventional shell elements with 6 degrees of freedom, 3 for displacements and 3 for rotations, are used. Fig. 5.5 shows the 8 nodes disposition, with the thickness direction indication, an important parameter to be entered. The code S8R is an 8-node, quadrilateral, stress/displacement shell element with reduced integration and a large-strain formulation.

Furthermore, for a composite section the total number of section points is defined by adding the number of integration points per layer for all of the layers. For shell sections integrated during the analysis, we can define the number of integration points per layer. The default is three for Simpson's rule and two for Gauss quadrature. For general shell sections, the number of section points for output per layer is three. Here the default Simpson's rule is used.

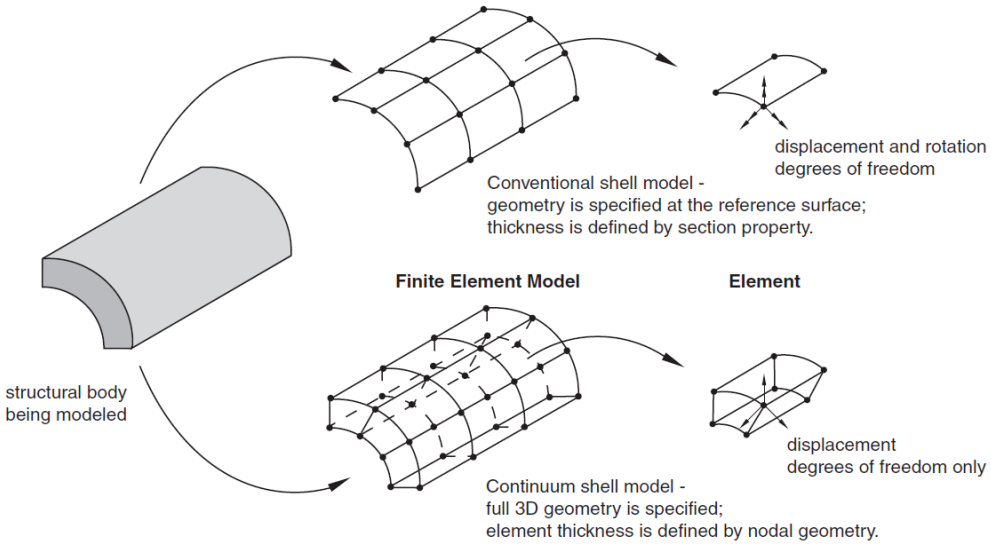

Fig. 5.4: Conventional versus continuum shell element

The mesh is visible in fig. 5.6, a geometry of 10x10 symmetrical square. The single shell element, obviously, is a square of side 10 mm.

5.2.6 Deformation results

As an example, figures 5.7, 5.8, 5.9 and 5.10 show some simulation results. In particular, the first figure gives us, in the left up corner, the value of the stresses in x direction (σ_x) of the Ply-1 (0°), the second one shows the stresses in y direction always for the Ply-1, fig 5.9 the imposed displacement in x direction, and fig. 5.10 the displacement in y direction due to the Poisson coefficient ν_{xy}. In all figure, the left down corner shows the reference system. Table 5.2 summarizes all the data extracted from the simulation.

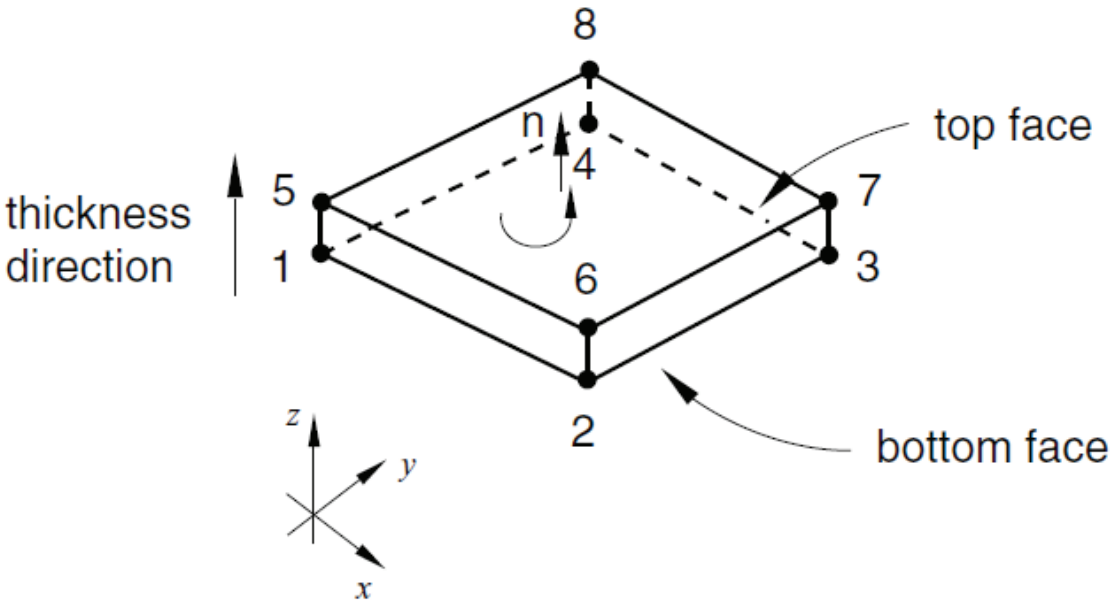

Fig. 5.5: Default normals and thickness direction for continuum shell elements

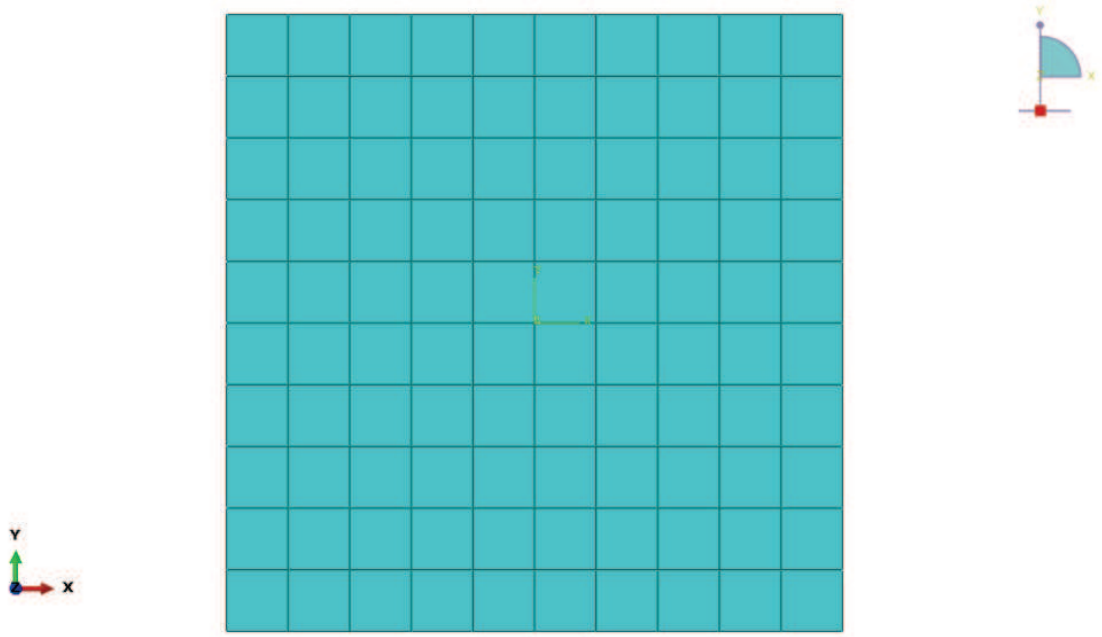

Fig. 5.6: Model mesh

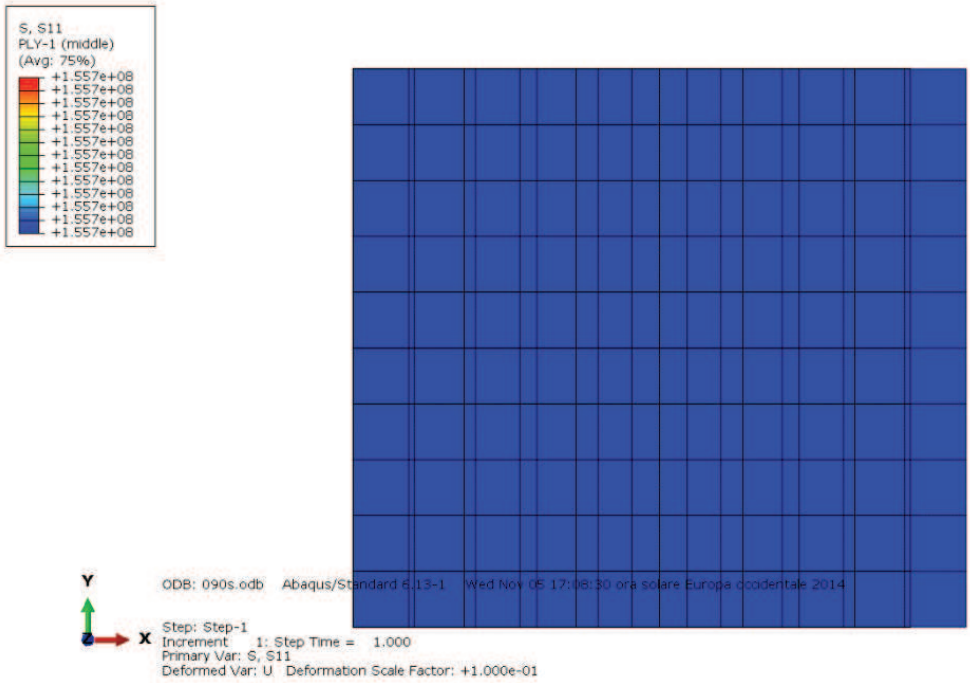

Fig. 5.7: σ_x stress of the Ply-1 in x direction

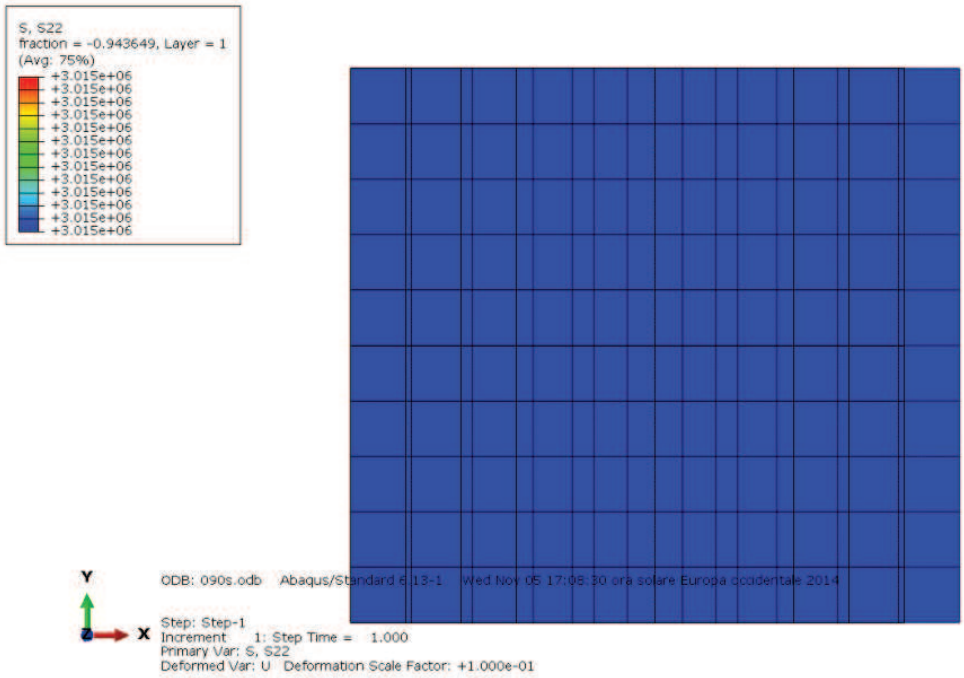

Fig. 5.8: σ_y stress of the Ply-1 in x direction

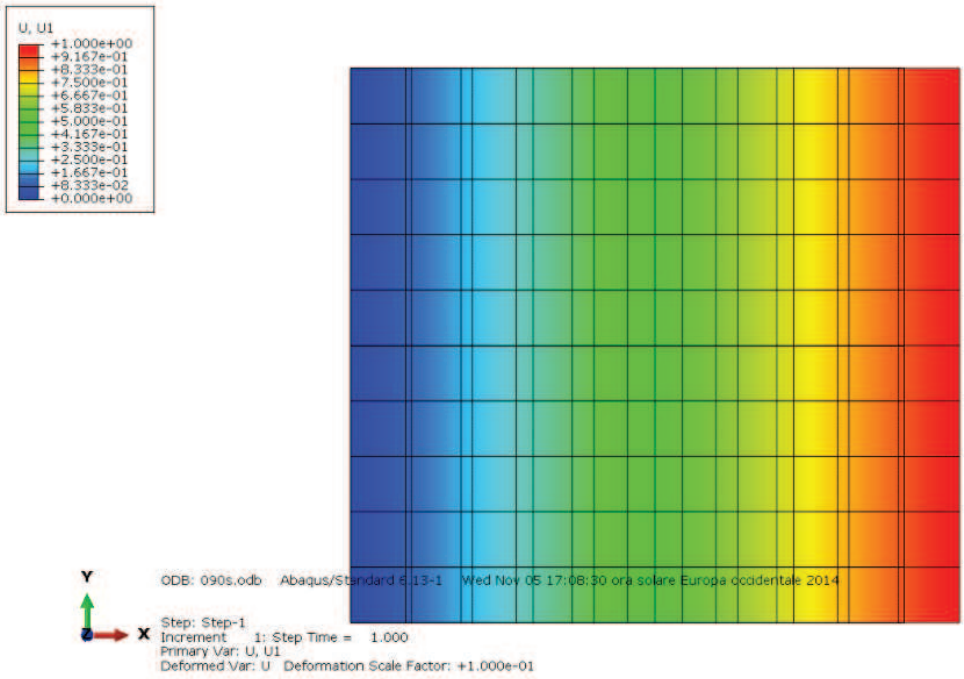

Fig. 5.9: U_x displacement of the Ply-1 in x direction

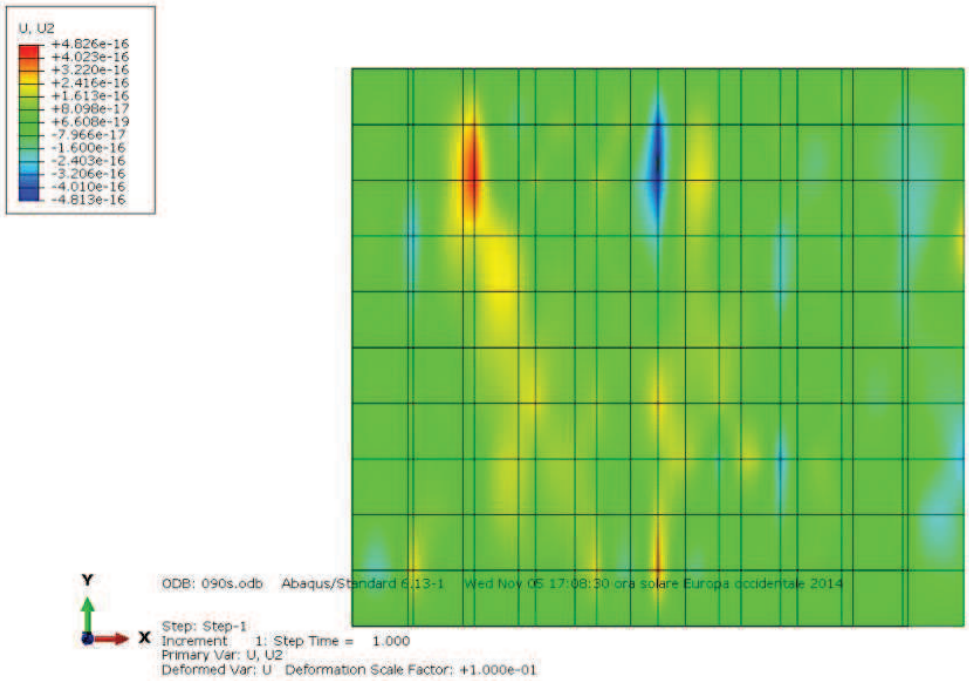

Fig. 5.10: U_y displacement of the Ply-1 in y direction

Orientation		S_{11} (Pa) [σ_x]	S_{22} (Pa) [σ_y]	S_{12} (Pa) [τ_{xy}]
Ply 1	0°	1.55748E08	3.01528E06	0.340E–08
Ply 2	90°	1.21584E07	3.01528E06	–3.182E–08
Ply 3	90°	1.21584E07	3.01528E06	–3.182E–08
Ply 4	0°	1.55748E08	3.01528E06	0.340E–08

Tab. 5.2: Numerical values from the simulation

5.2.7 Expected analytical results

Analytical values of the laminate were calculated by means of an Excel file (Tab. 5.4). From the Excel file, the results of interest were extracted (Tab. 5.3) and we have:

Ply-1 (0°)	Ply-2 (90°)
σ_x=155,75 MPa	σ_x=12,158 MPa
σ_y=3,0153 MPa	σ_y=3,0153 MPa
τ_{xy}=0	τ_{xy}=-2,1017E-11

Tab. 5.3: Analytical results

5.2.8 Results comparison

As we can see, comparing results from table 5.2 and table 5.3, we can confirm that there are no relevant differences. Further confirmation of the good results is taken out from Hyer "Stress Analysis of Fiber-Reinforced Composite Materials", 1998, Example 1, pp. 231, from which the table 5.5 was extracted.

Orientation		σ_x [MPa]	σ_y [MPa]	τ_{xy} [MPa]
Ply 1	0°	155.7	3.02	0
Ply 2	90°	12.16	3.02	0
Ply 3	90°	12.16	3.02	0
Ply 4	0°	155.7	3.02	0

Tab. 5.5: Extracted results from Hyer (example 1, pg. 231)

Laminato [0/90]s																			
					gradi	rad													
E1=	1,55E+11	NI12=	0,248	teta1=	0	0	V1=	6,14202E-11	V3=	-1,68721E-11									
E2=	1,21E+10	NI21=	0,01936	teta2=	90	1,570796327	V2=	-3,80965E-11	v4=	-1,84721E-11									
G12=	4,40E+09																		
G13=	4,40E+09	epsilon1=	1,00E-03		epsilon1=	1,00E-03	z0=	-0,0003	z3=	0,00015									
G23=	3,20E+09	epsilon2=	0,00E+00		epsilon2=	0,00E+00	z1=	-0,00015	z4=	0,0003									
		epsilon6=	0,00E+00		epsilon6=	0,00E+00	z2=	0											
t=	1,50E-04																		
			teta1			teta2				teta1		teta2							
Q11=	1,5575E+11	Q11segn=	1,5575E+11		Q11segn=	1,2158E+10	S11=	6,4516E-12	S11segn=	6,4516E-12	S11segn=	8,2645E-11	A11=	5,0372E+07	B11=	0,00E+00	D11=	7,4412E+00	
Q12=	3,0153E+09	Q22segn=	1,2158E+10		Q22segn=	1,5575E+11	S22=	8,2645E-11	S22segn=	8,2645E-11	S22segn=	6,4516E-12	A22=	5,0372E+07	B22=	0,00E+00	D22=	1,6258E+00	
Q22=	1,2158E+10	Q12segn=	3,0153E+09		Q12segn=	3,0153E+09	S12=S21=	-1,6000E-12	S12segn=	-1,6000E-12	S12segn=	-1,6000E-12	A12=	1,8092E+06	B12=	0,00E+00	D12=	1,6282E-01	
Q66=	4,4000E+09	Q16segn=	0,0000E+00		Q16segn=	-2,1017E-08	S66=	2,2727E-10	S16segn=	0,0000E+00	S16segn=	3,6009E-27	A16=	-6,3052E-12	B16=	0,00E+00	D16=	-1,4187E-19	
		Q26segn=	0,0000E+00		Q26segn=	8,8169E-06			S26segn=	0,0000E+00	S26segn=	-1,2936E-26	A26=	2,6451E-09	B26=	0,00E+00	D26=	5,9514E-17	
		Q66segn=	4,4000E+09		Q66segn=	4,4000E+09			S66segn=	2,2727E-10	S66segn=	2,2727E-10	A66=	2,6400E+06	B66=	0,00E+00	D66=	2,3760E-01	
		sigma x=	1,5575E+08		sigma x=	1,2158E+07	Nx=	5,0372E+04											
		sigma y=	3,0153E+06		sigma y=	3,0153E+06	Ny=	1,8092E+03											
		tau xy=	0,0000E+00		tau xy=	-2,1017E-11	Nxy=												

Tab. 5.4: Excel file with analytical results

5.3 Laminate $[45°/-45°]_s$

5.3.1 Laminate dimensions

Fig. 5.11 shows the laminate, a simple 100 x 100 mm square, with t=0,25 mm of laminae thickness.

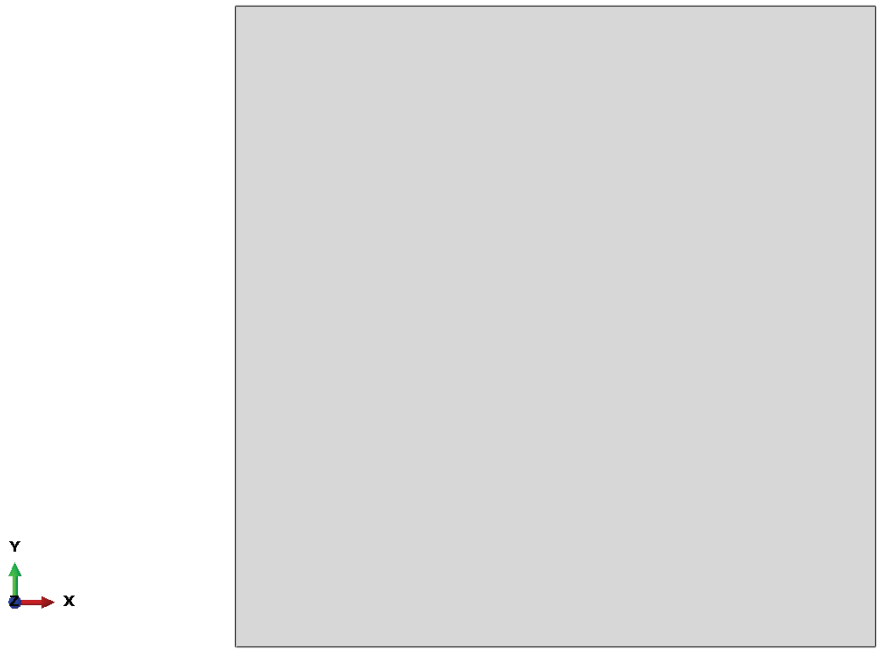

Fig. 5.11: $[45°/-45°]_s$ laminate

5.3.2 Laminate model

As we can see in Fig. 5.12, laminate is made of 4 symmetric thin layer oriented at 45° and -45°. On the right fig. 5.12 shows a vertical section of the laminate with direction 1 as x axes, direction 2 as y axes, and direction 3 as z axes, wiz the stack direction of the laminate.

5.3.3 Material properties

Laminae are made of Graphite/Epoxy material (AS4/3501-6) [26], which properties are in table 5.6:

E_1=138,0 GPa	ν_{12}=0,30	G_{12}=6,90 GPa
E_2=9,0 GPa	ν_{13}=0,30	G_{13}=6,90 GPa
E_3=9,0 GPa	ν_{23}=0,50	G_{23}=3,70 GPa

Tab. 5.6: Material properties

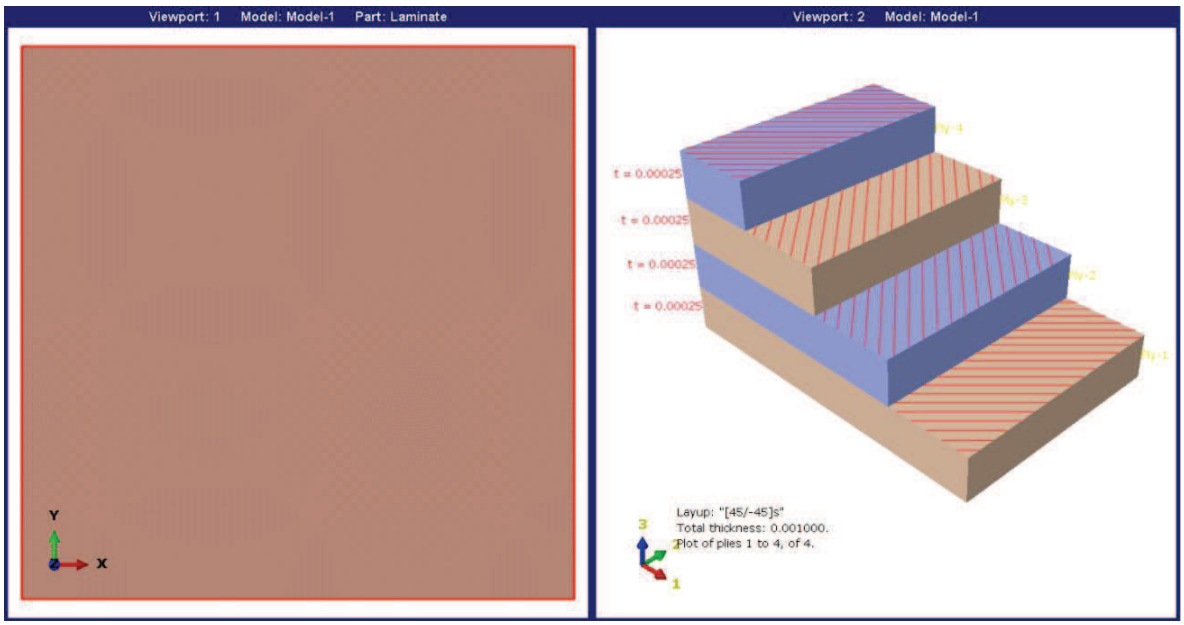

Fig. 5.11: Laminate model and relative section

5.3.4 Boundary conditions and loads

In fig. 5.12 we can see loads and boundary conditions used for the simulation. The vertical left zone is pinned symmetrically; in other words, the displacements along x axes and the rotations along y and z axes are locked (U1=UR2=UR3=0); upper and lower part of the model are free; on the right side we impose a constant load (Shell Edge Load) in x direction of 50 MPa.mm in the positive direction of x axes.

5.3.5 Element type and mesh

Shell type is the same used in par. 5.2.5, wiz S8R, with the same integration modality. The only difference is the mesh dimension, visible in fig. 5.13, a geometry of 5x5 symmetrical square. The single shell element, obviously, is a square of side 5 mm.

5.3.6 Deformation results

As an example, figures 5.14, 5.15 and 5.16 show the strains for each direction. In particular, the first figure gives us, in the left up corner, the value of the strain in x direction (ε_{0x}), identical for all plies due to symmetry of the laminate, the second one shows the strain in y direction (ε_{0y}), and the third figure the displacement in z direction (γ_{xy}).

For completeness, fig 5.17, 5.18 and 5.19 show the displacement configuration of the first ply, u_1, u_2 and u_3. In all figure, the left down corner shows the reference system. Table 5.6 summarizes all the data extracted from the simulation.

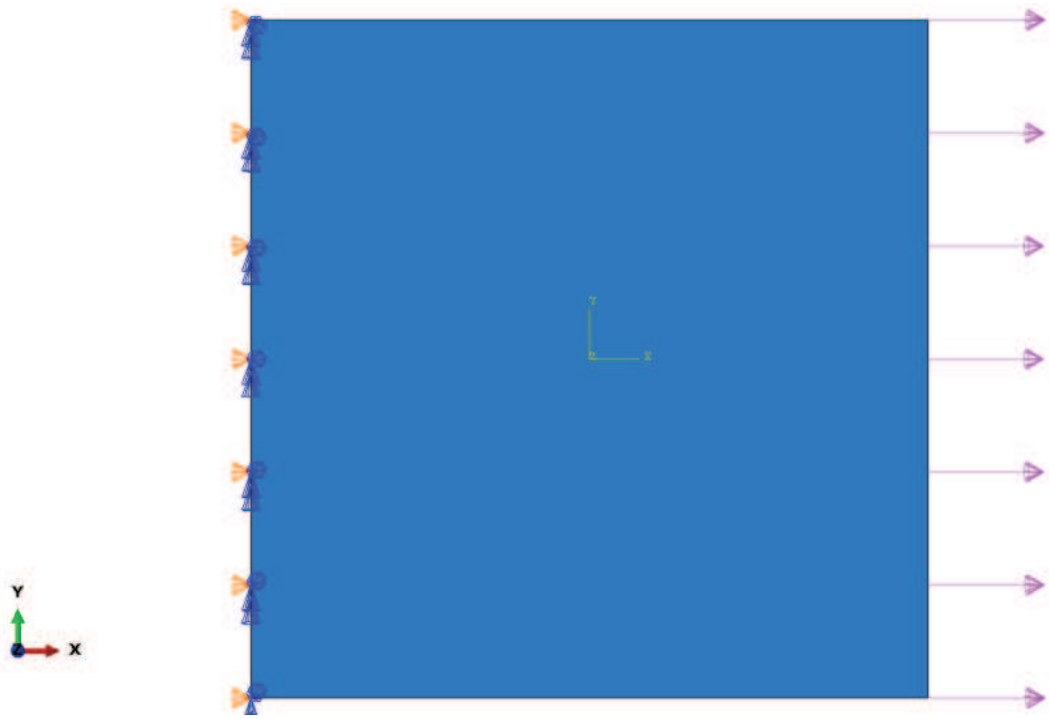

Fig. 5.12: Boundary conditions and loads

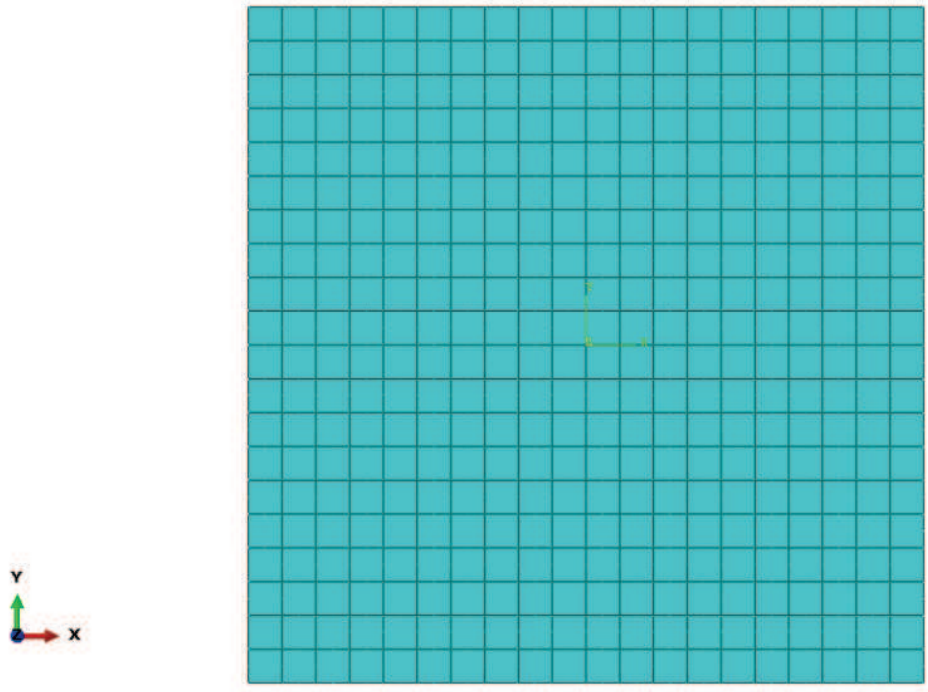

Fig. 5.13: Model mesh

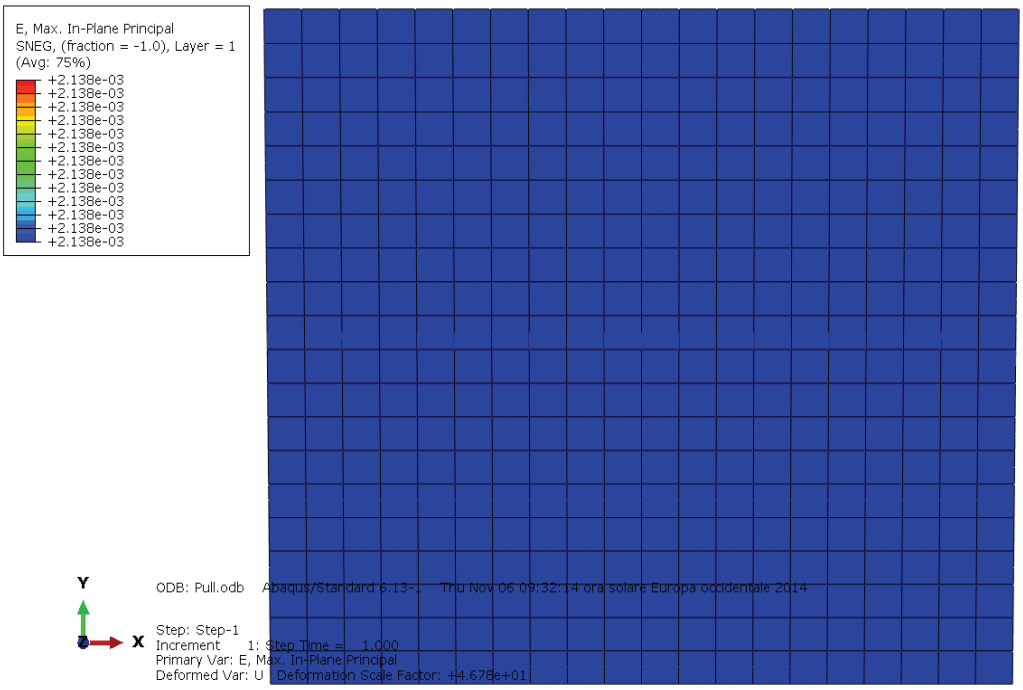

Fig. 5.14: Strain in x direction (ε_{0x})

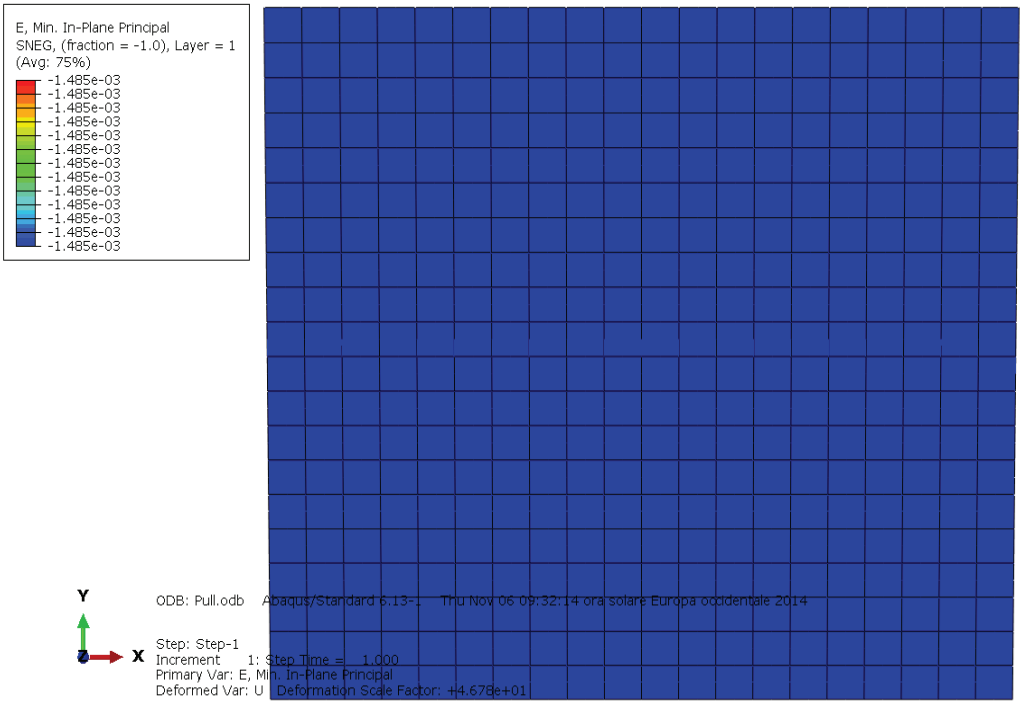

Fig. 5.15: Strain in y direction (ε_{0y})

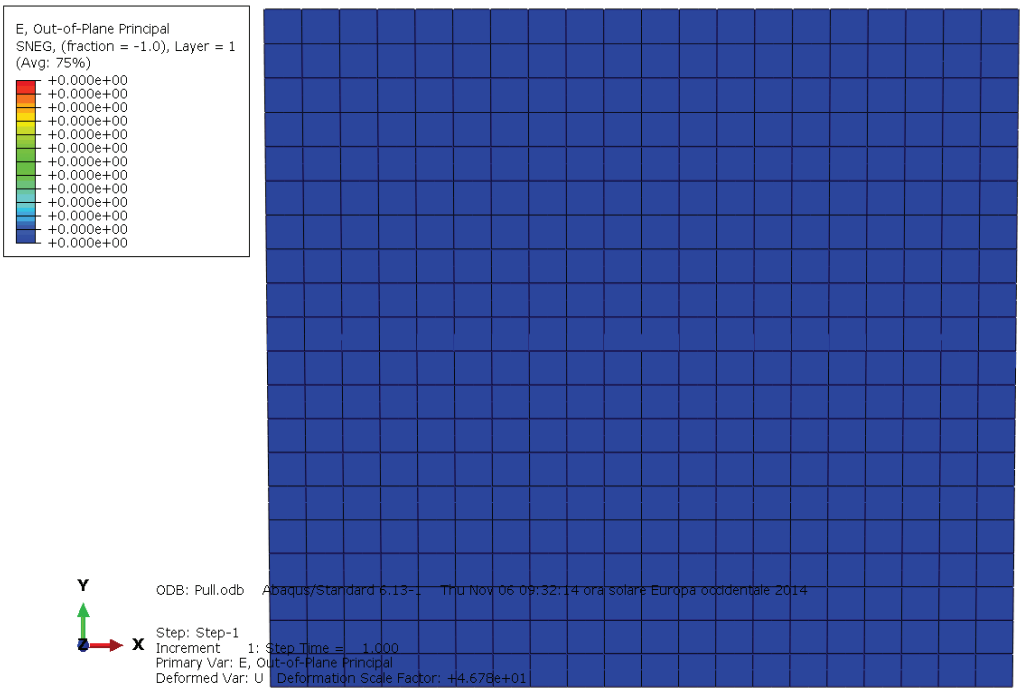

Fig. 5.16: Strain in z direction (γ_{xy})

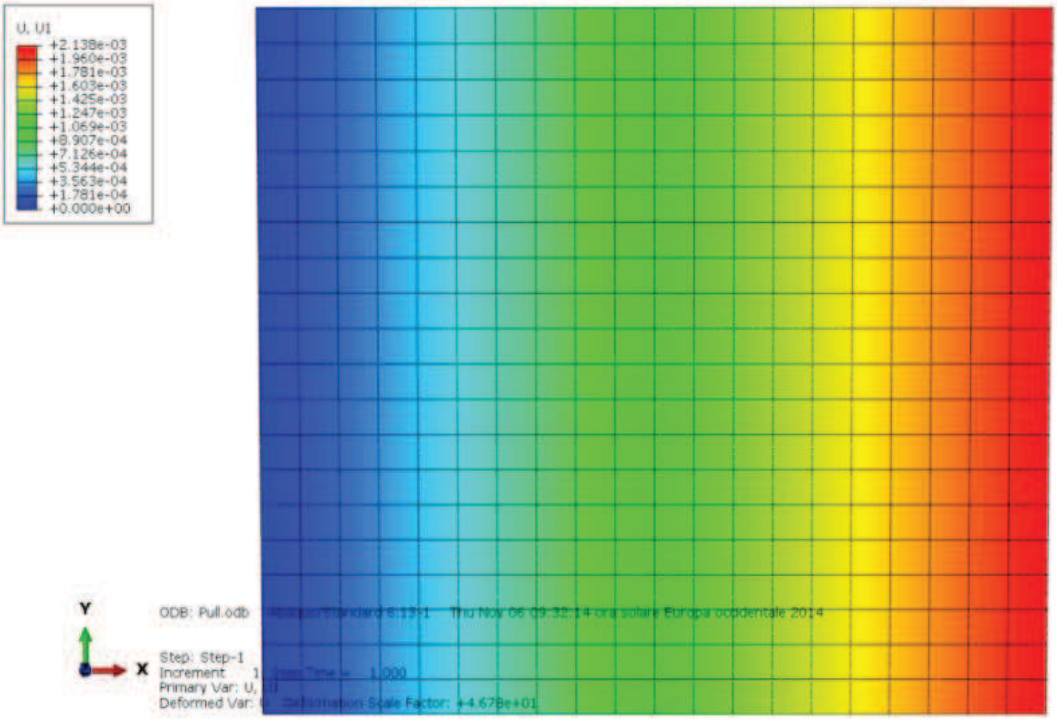

Fig. 5.17: Displacement in x direction (u_1)

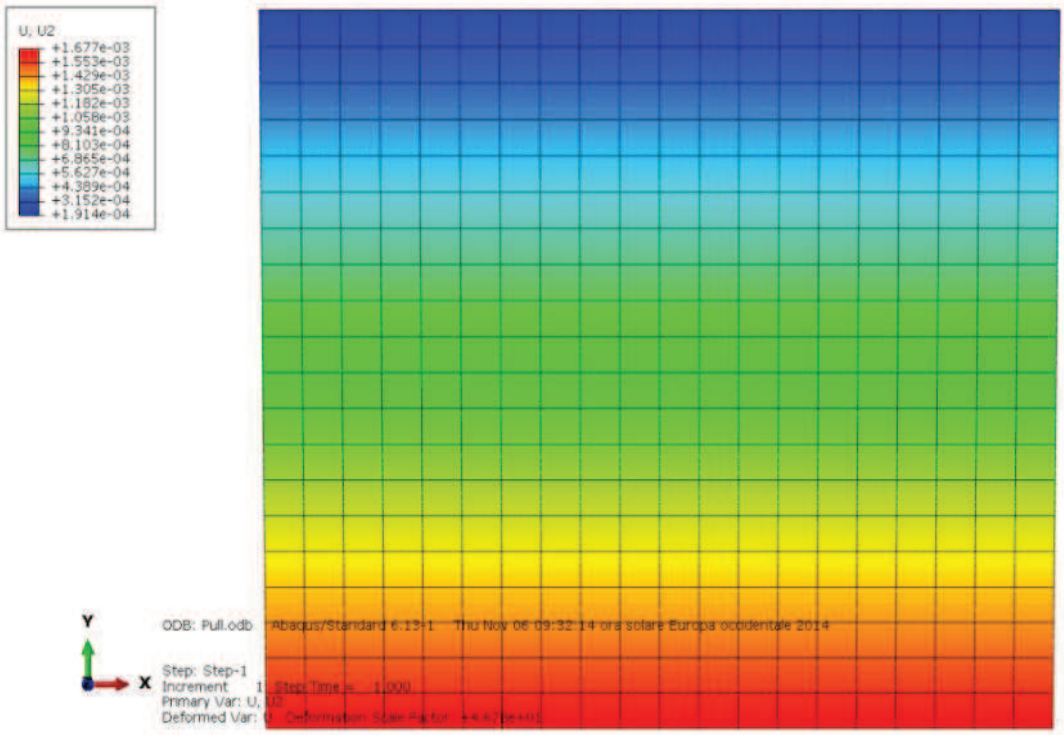

Fig. 5.18: Displacement in y direction (u_2)

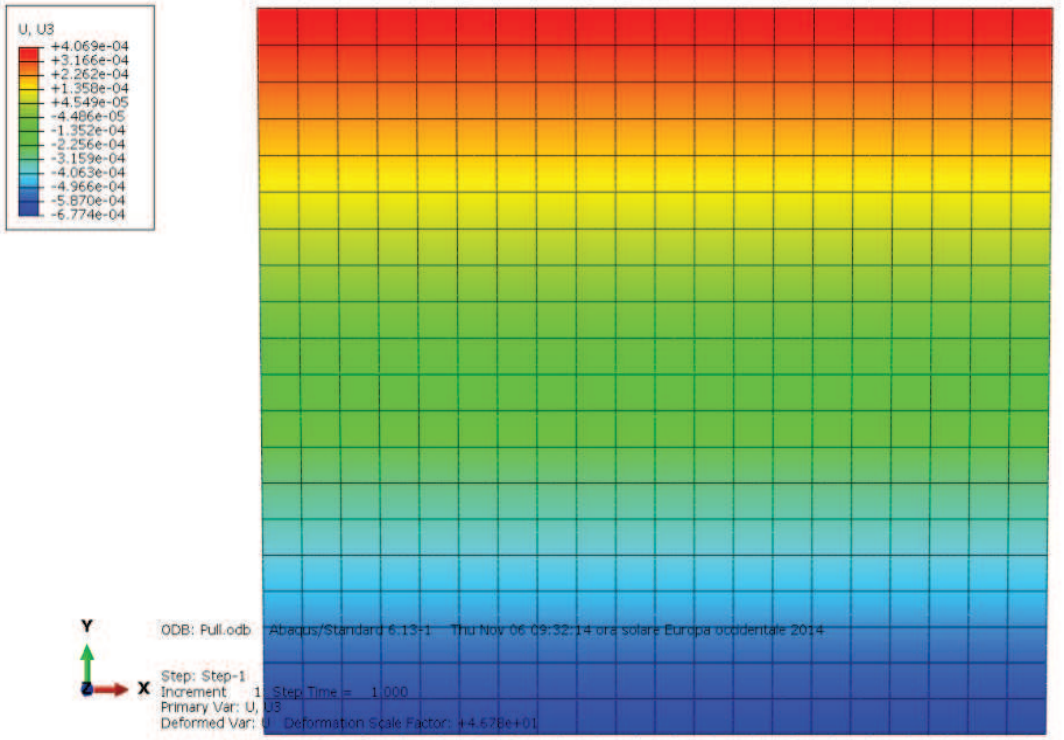

Fig. 5.19: Displacement in z direction (u_3)

Orientation		ε_{0x}	ε_{0y}	γ_{xy}
Ply 1	45°	2.13775E–03	–1.48544E–03	0
Ply 2	-45°	2.13775E–03	–1.48544E–03	0
Ply 3	-45°	2.13775E–03	–1.48544E–03	0
Ply 4	45°	2.13775E–03	–1.48544E–03	0

Tab. 5.7: Numerical values from the simulation

5.3.7 Expected analytical results

Analytical values of the laminate, also in this case, were calculated by means of an Excel file (Tab. 5.9). From the Excel file, the results of interest were extracted (Tab. 5.8) and we have:

ε_{0x}=0,002138 ε_{0y}=-0,001485 γ_{xy}=0

σ_x=50 MPa σ_y=0 τ_{xy}=21,116 MPa

5.3.8 Results comparison

As we can see, comparing results from table 5.7 and table 5.9. We can confirm that there are no relevant differences($\pm$0,1%). Further confirmation of the good results is taken out from Gibson, 3rd Ed, "Principles of Composite Materials Mechanics", Example 7.8 pp. 317-318.

5.4 Laminate [0°/90°]s with an hole

5.4.1 Laminate dimensions

The laminate consists in a rectangular plate of 200 x 100 mm sided, with a centered hole of 20 mm diameter, laminae thickness t=0,15 mm. Due to symmetry plate, the simulation analyses only a quarter of the laminate, once fixed the symmetry boundary conditions along the cuts. Fig. 5.20 shows the model used.

Laminato [45/-45]s									
					gradi	rad			
E1=	1,38E+11	Ni12=	0,3	teta1=	45	0,785398163			
E2=	9,00E+09	Ni21=	0,019565217	teta2=	-45	-0,785398163			
G12=	6,90E+09								
G13=	6,90E+09	N_x	5,000E+04	N_x	5,000E+04	z0=	-0,0005	z3=	0,00025
G23=	4,40E+09	N_y	0,000E+00	N_y	0,000E+00	z1=	-0,00025	z4=	0,0005
		Tau_xy	0,00E+00	Tau_xy	0,00E+00	z2=	0		
t=	0,25 mm	N=	4						
		teta1=	45	teta2=	-45				
Q11=	1,3881E+11	Q11segn=	4,522E+10	Q11segn=	4,522E+10				
Q12=Q21=	2,7159E+09	Q22segn=	4,522E+10	Q22segn=	4,522E+10				
Q22=	9,0531E+09	Q12segn=	3,142E+10	Q12segn=	3,142E+10				
Q66=	6,9000E+09	Q16segn=	3,244E+10	Q16segn=	-3,244E+10				
		Q26segn=	3,244E+10	Q26segn=	-3,244E+10				
		Q66segn=	3,561E+10	Q66segn=	3,561E+10				
A11=	4,522E+07	B11=	0,00E+00	D11=	3,77E+00				
A22=	4,522E+07	B22=	0,00E+00	D22=	3,77E+00				
A12=	3,142E+07	B12=	0,00E+00	D12=	2,62E+00				
A16=	0,000E+00	B16=	0,00E+00	D16=	2,03E+00				
A26=	0,000E+00	B26=	0,00E+00	D26=	2,03E+00				
A66=	3,561E+07	B66=	4,55E-13	D66=	2,97E+00				
Inversa di A		DET=	3,76661E+22						
A'11=	4,276E-08								
A'22=	4,276E-08		epsilon_x=	2,138E-03					
A'12=	-2,971E-08		epsilon_y=	-1,485E-03					
A'16=	0		gamma_xy=	0,00E+00					
A'26=	0								
A'66=	2,808E-08		sigma_x=	5,000E+07					
			sigma_y=	0,000E+00					
			tau_xy=	2,116E+07					

Tab. 5.9: Excel file with analytical results

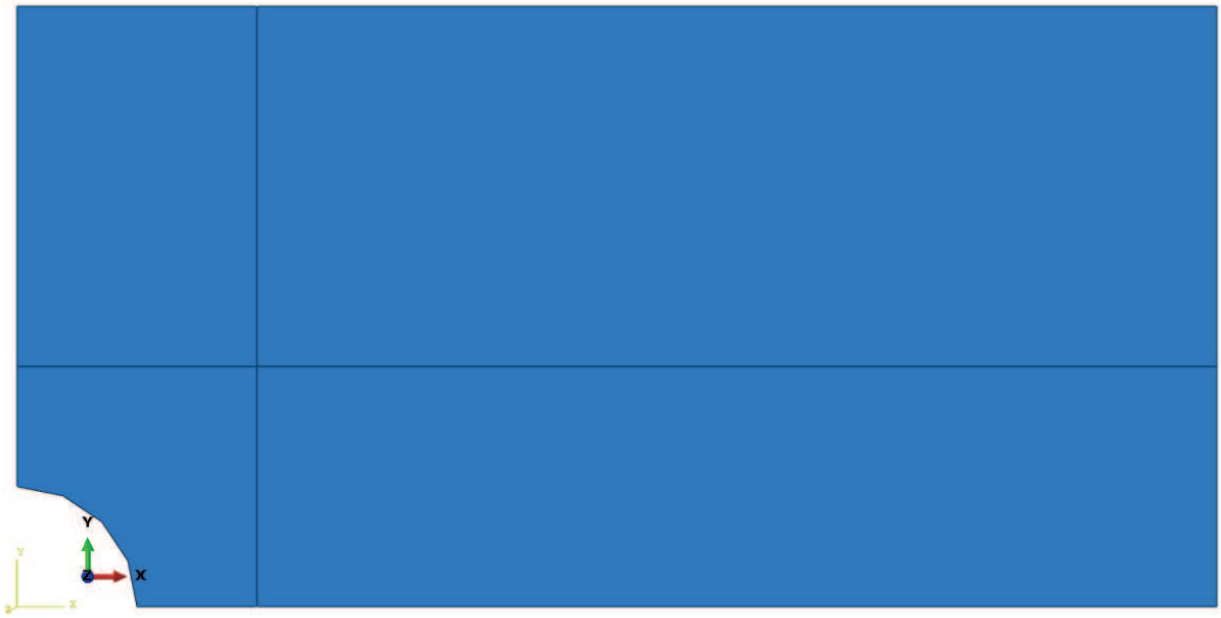

Fig. 5.20: Plate with hole model

5.4.2 Laminate model

As we can see in Fig. 5.21, laminate is made of 4 symmetric thin layer oriented at 0° and 90°, i.e. $[0°, 90°]_s$. On the right side, fig. 5.21 shows a vertical section of the laminate with direction 1 as x axes, direction 2 as y axes, and direction 3 as z axes, wiz the stack direction of the laminate.

5.4.3 Material properties

Laminae are made of Graphite/Epoxy material, the same material used in the first simulation, which properties are in table 5.10.

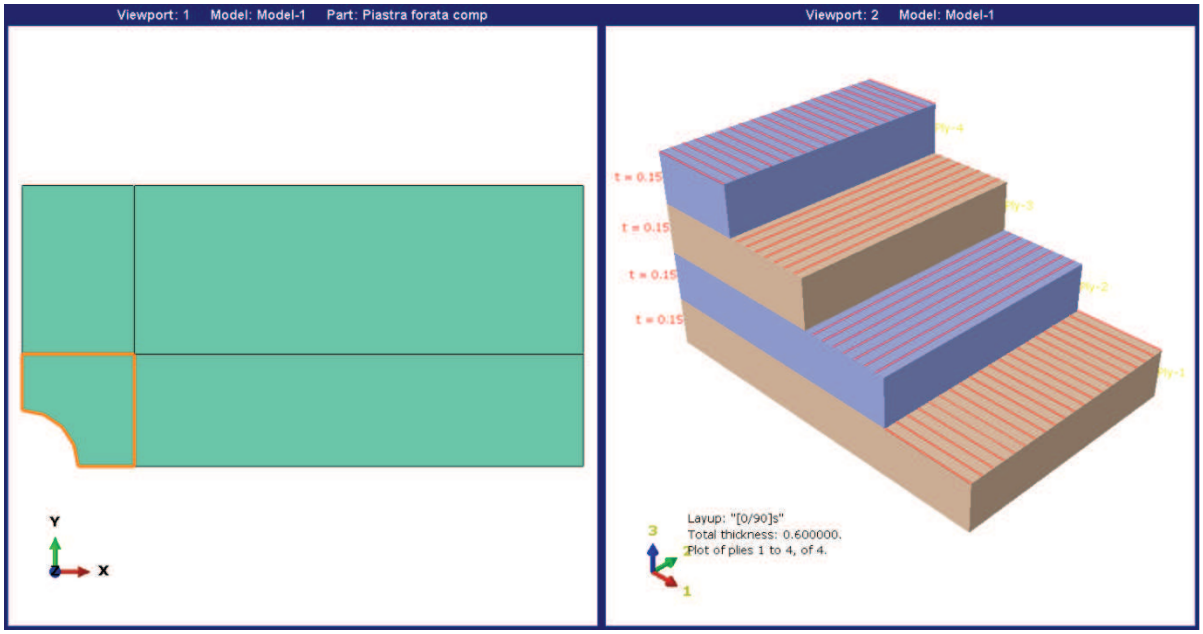

Fig. 5.21: Laminate model and relative section

E_1=155,0 GPa	ν_{12}=0,248	G_{12}=4,40 GPa	α_1=–0,018x10^{-6} /°C
E_2=12,10 GPa	ν_{13}=0,248	G_{13}=4,40 GPa	α_2=24,3x10^{-6}/°C
E_3=12,10 GPa	ν_{23}=0,458	G_{23}=3,20 GPa	α_3=24,3x10^{-6}/°C

Tab. 5.10: Material properties

5.4.4 Boundary conditions and loads

In fig. 5.22, we can see loads and boundary conditions used for the simulation. The vertical left zone and the lower zone are constrained with symmetry conditions. In other words, all the displacements along x are locked in the vertical cut (U_1=0), and the same is for the lower cut (U_2=0). On the right side, we impose a constant Shell Edge Load in x direction of 1 MPa.mm.

5.4.5 Element type and mesh

For a better comprehension of the phenomena, knowing that we have critical values of stress around the hole, the mesh was enhanced just there. The laminate was partitioned in 4 zones, around the hole with a refined mesh, the other three ones with a consequential adapted mesh. In this case, in addition to stress analysis, we made also a convergence study, described later in the paragraph. Fig. 5.23 and 5.24 show the particular mesh used for the last simulation. Shell type is the same used in par. 5.2.5, wiz S8R, with the same integration modality.

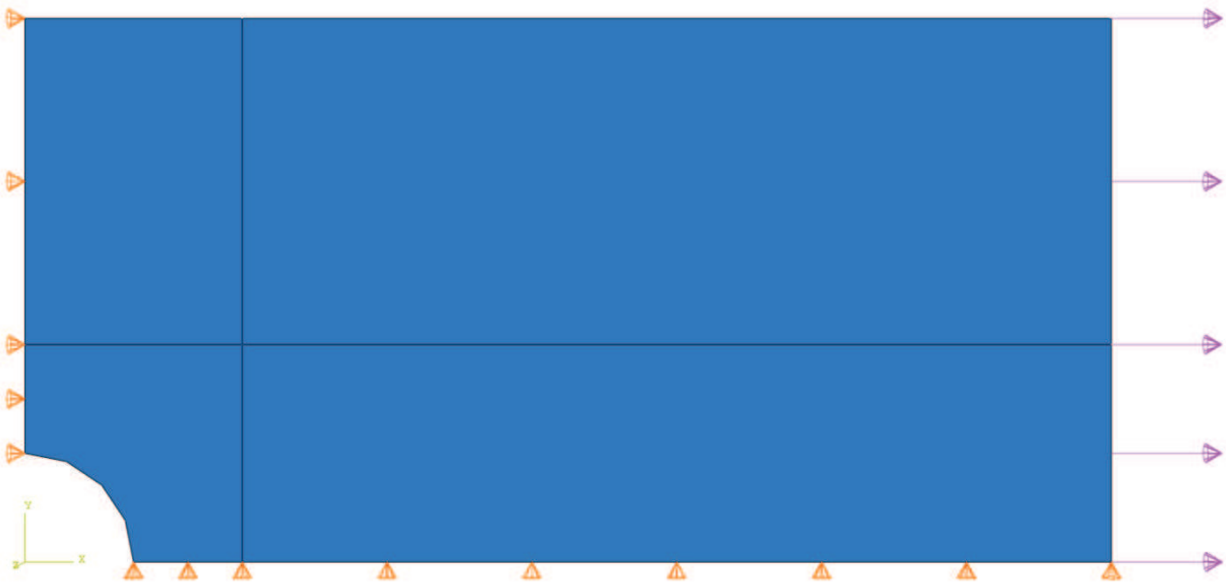

Fig. 5.22: Symmetric boundary conditions and loads

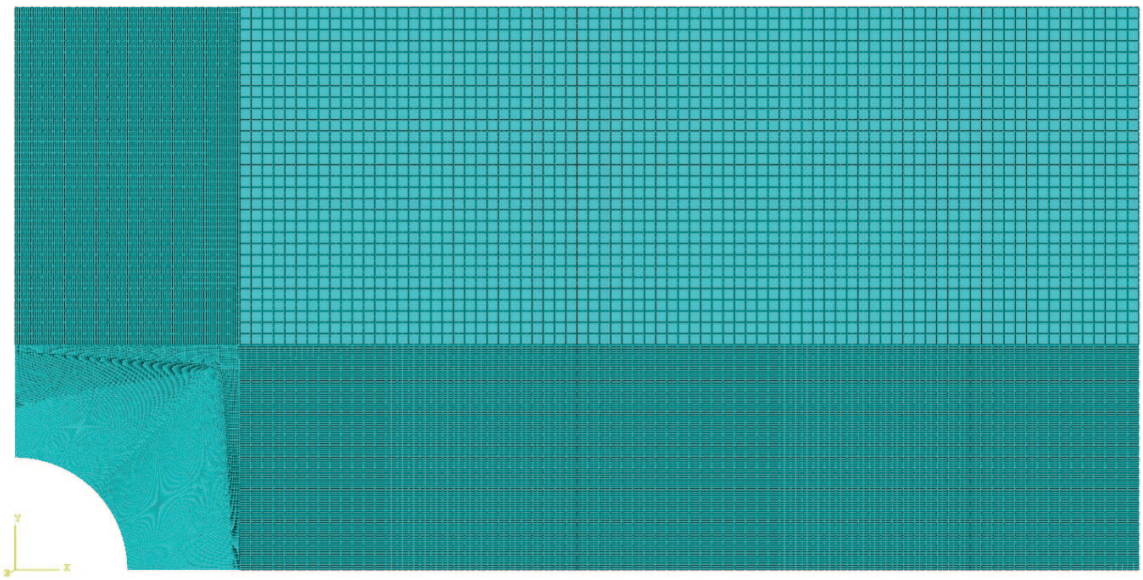

Fig. 5.23: Mesh of the plate with hole

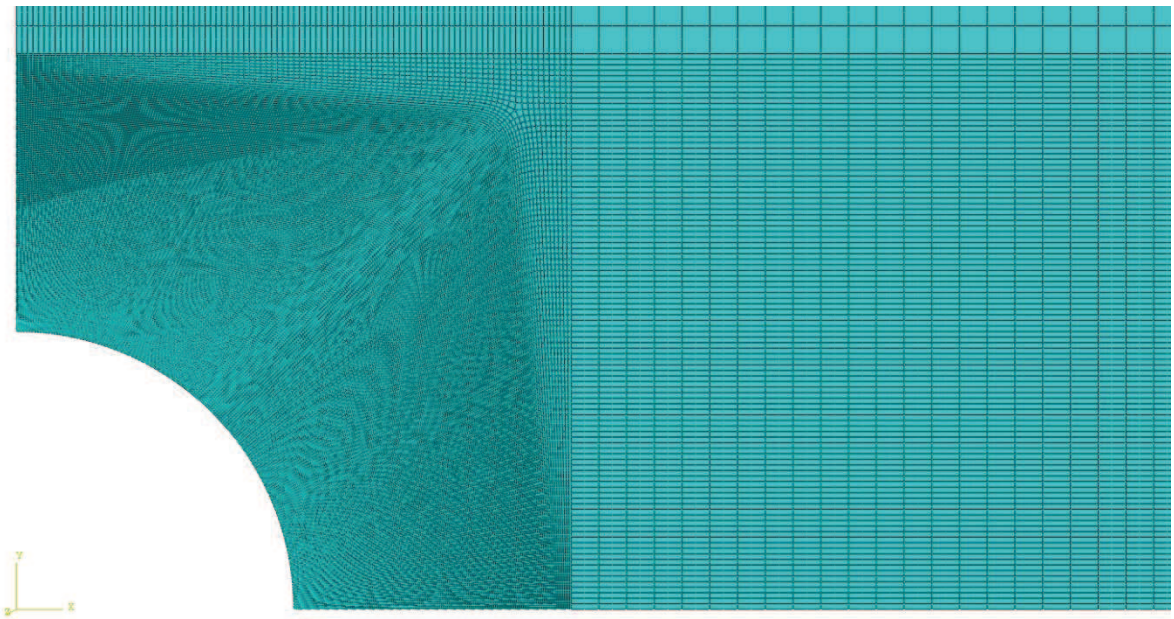

Fig. 5.24: Zoom on the hole mesh

5.4.6 Deformation results

Fig. 5.25 show the max strain deformation along the x direction of the Ply-1 and fig. 5.26 a zoom around the hole of the same plot. Thought fig. 5.27 and 5.28 seems similar, the left up corner gives the stress values, σ_x along the x direction of the Ply-1. Note that the factor scale is very high ($3x10^6$), necessary to emphasize the deformations.

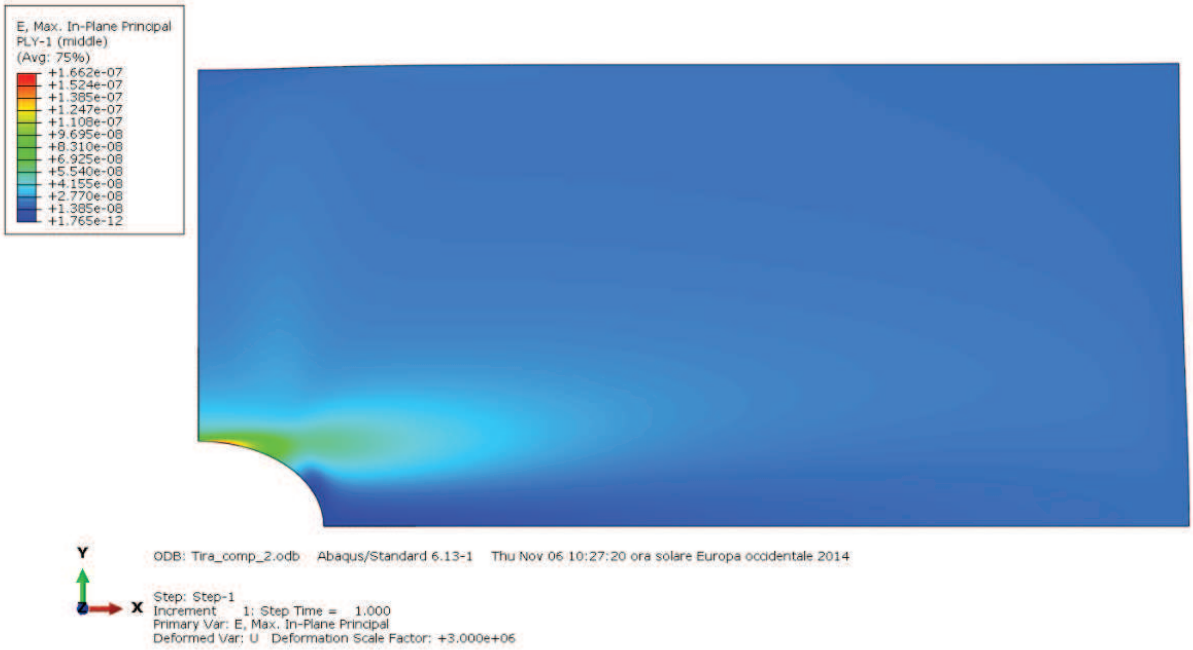

Fig. 5.25: Strain in x direction (ε_{0x})

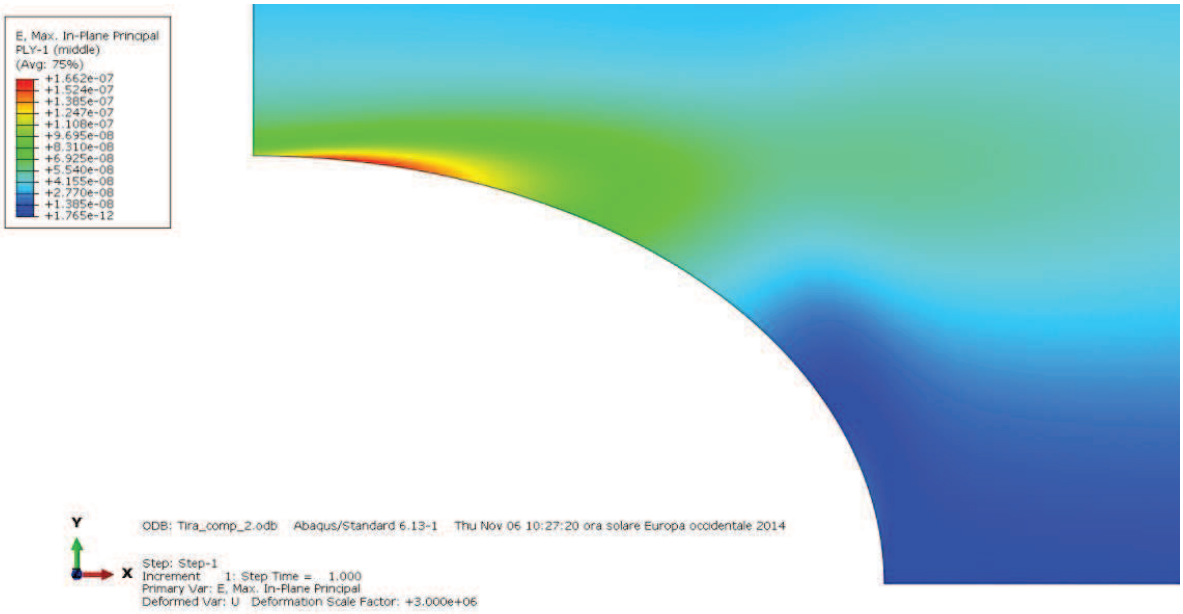

Fig. 5.26: Zoom around the hole of fig. 5.25

Fig. 5.27: σ_x stress of the Ply-1 in x direction

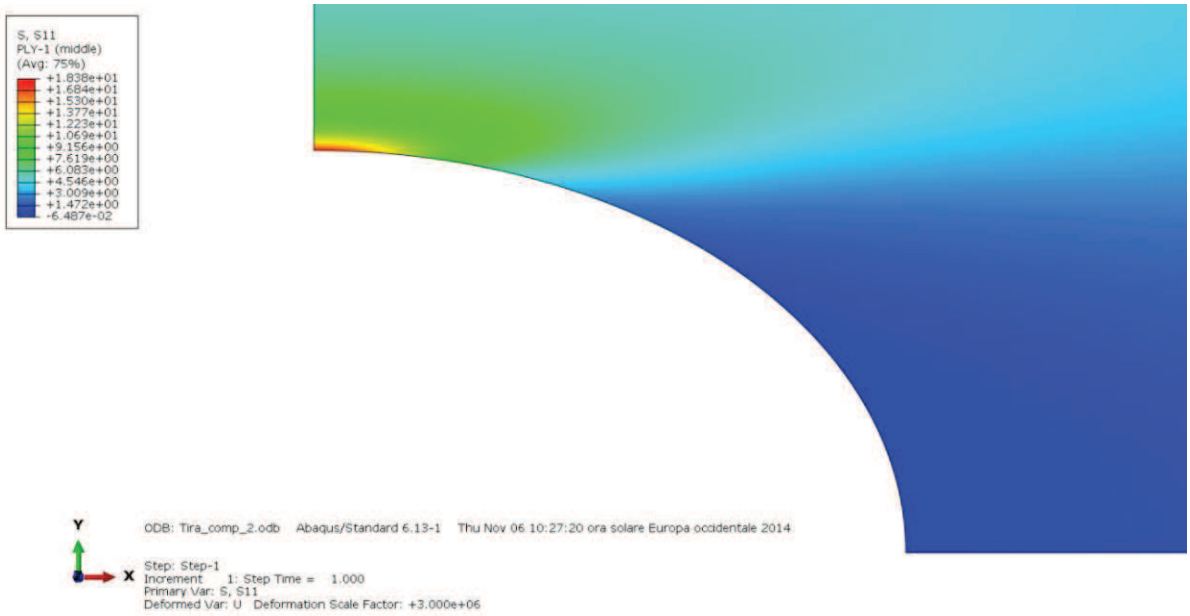

Fig. 5.28: Zoom of fig. 5.27

5.4.7 Expected results with Ansys

In this case, the comparison of results is made with another simulation software, Ansys. The thesis co-tutor, Prof. F. Mollica, skilful in the use of this code, analysed the same model, with the same parameter, material properties, boundary conditions and loads.

Mesh	S_{11}	Delta S_{11}
4	9,7009	
8	11,7465	2,0456
16	13,8027	2,0562
24	16,5607	2,758
32	16,9788	0,4181
40	17,292	0,3132
48	17,5397	0,2477
56	17,6916	0,1519
64	17,8059	0,1143

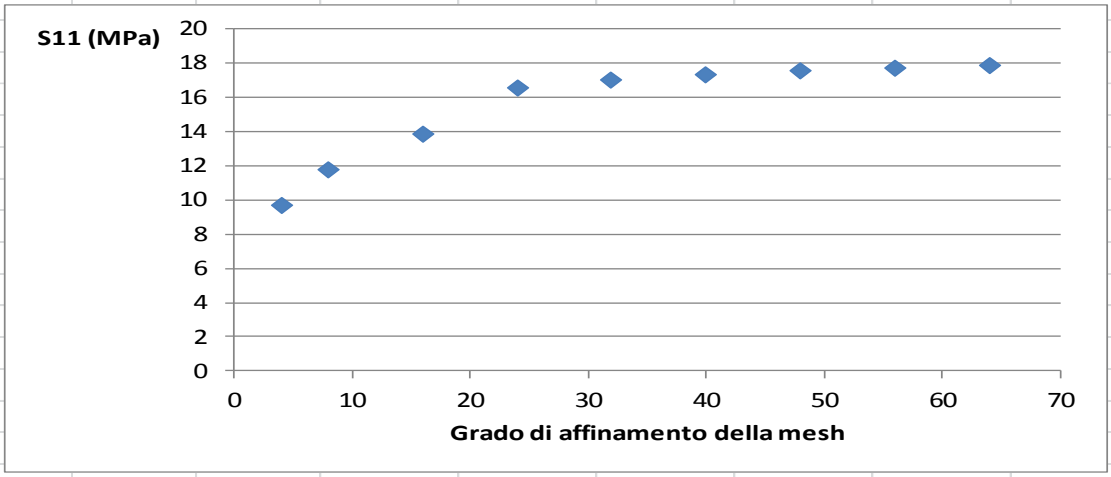

Fig. 5.29: Convergence curve of σ_x vs element number/radius hole ratio (Ansys)

Fig. 5.29 shows the results obtained with Ansys, in particular the figure shows the convergence curve of S_{11} (σ_x) in function of the element number/radius hole ratio. The better value of σ_x, with the finer mesh, is σ_x=17,8059 MPa. Other simulations are made using the same model, but with a different material, steel, (E=210 GPa, ν=0.3), compared with analytical results, and the values are identical, that is, a good validation if the Abaqus model.

5.4.8 Results comparison

As mentioned before, the fig. 5.30 shows the convergence curve of S_{11} (σ_x) versus the element number/radius hole ratio, obtained with Abaqus simulation. The last values, being the differences very small, confirm that the model converges to the exact value of σ_x, that is, it is not necessary to continue the mesh fitting.

Piastra forata composito

Nr elementi/r	2	4	6	8	10	12	14	16	18	20	22	24	26	28	30	32	34	36
S_{11}	17,04	17,54	17,82	18,01	18,12	18,19	18,24	18,27	18,30	18,31	18,33	18,34	18,35	18,36	18,36	18,37	18,37	18,38

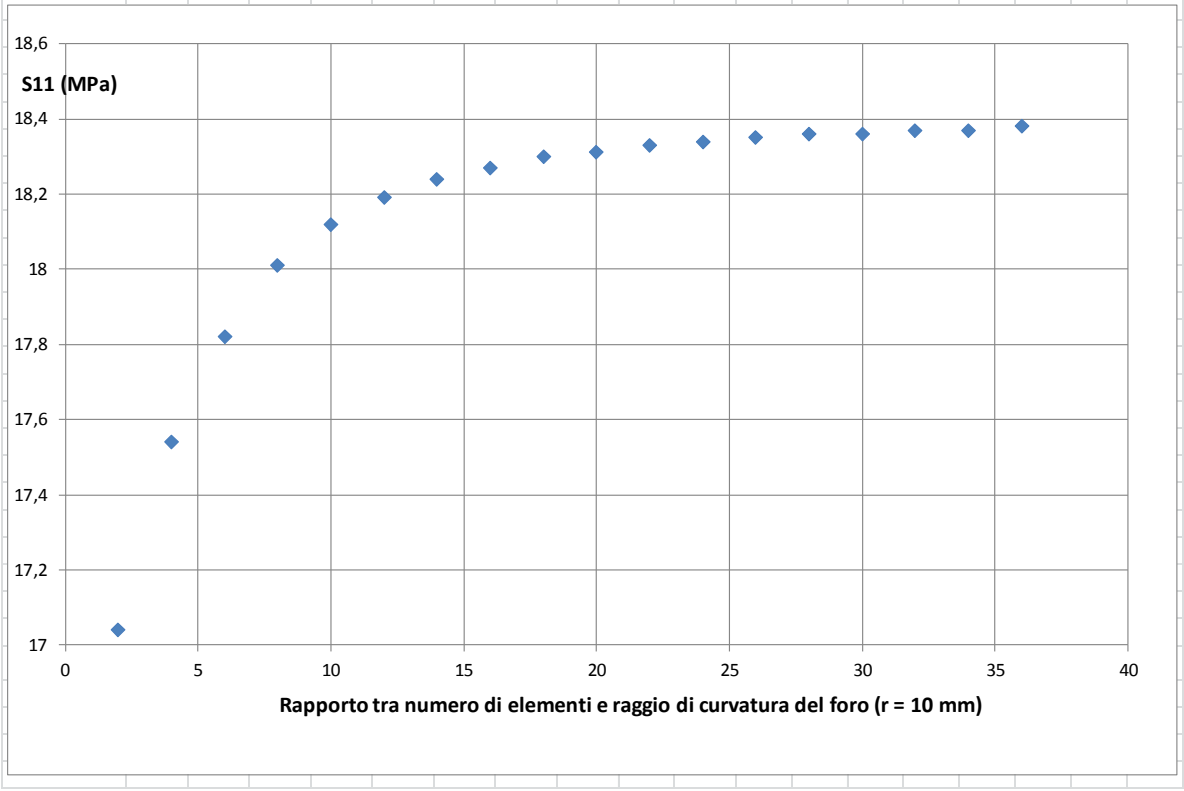

Fig. 5.30: Convergence curve of σ_x vs element number/radius hole ratio (Abaqus)

The next table (Tab. 5.11) is a summary of the output results extracted from the file report of Abaqus. As we can see, the value of σ_x differs from the Ansys value only for +3,12 %. In the critical zone, next the hole, the value goes up, as we can see in fig. 5.28 (the red zone) and in the tab. 5.11 (the red value)

Orientation		**E. max**	**E. mid**	**E. min**	**E_{11}**	**E_{22}**	**E_{12}**
Ply 1	0°	1.66205E-07	3.72017E-09	0	1.18076E-07	4.50654E-09	4.69937E-08
Ply 2	90°	1.76505E-12	-1.02215E-07	0	4.50654E-09	1.18076E-07	2.51779E-07
Ply 3	90°	1.76505E-12	-1.02215E-07	0	4.50654E-09	1.18076E-07	2.51779E-07
Ply 4	0°	1.66205E-07	3.72017E-09	0	1.18076E-07	4.50654E-09	4.69937E-08
Orientation		**ε_{0x}**	**ε_{0y}**	**γ_{xy}**	**S_{11} [σ_x] (Pa)**	**S_{22} [σ_y] (Pa)**	**S_{12} [τ_{xy}] (Pa)**
Ply 1	0°	2.391E-06	4.005E-08	6.528E-21	1.838E07	3.046E05	2.068E05
Ply 2	90°	2.391E-06	4.005E-08	6.528E-21	7.312E05	1.423E06	1.123E06
Ply 3	90°	2.391E-06	4.005E-08	6.528E-21	7.312E05	1.423E06	1.123E06
Ply 4	0°	2.391E-06	4.005E-08	6.528E-21	1.838E07	3.046E05	2.068E05

Tab. 5.11: Summary of the Abaqus report file (.rpt)

5.5 NAFEMS R0031/1 [Abaqus Benchmarks Guide (4.9.1)]

5.5.1 Introduction

Abaqus documentation provides different guides, which help to implement correctly simulations on Abaqus/CAE. One of this guide is the Benchmarks Guide for Abaqus. It contains benchmark problems (including the NAFEMS suite of test problems) and standard analyses used to evaluate the performance of Abaqus. The tests in this guide are multiple element tests of simple geometries or simplified versions of real problems.

Many of these problems are quite difficult and test a combination of capabilities in the code. Another guide is the Abaqus Verification Guide, which contains a large number of examples that are intended as elementary verification of the basic modeling capabilities in Abaqus. The last one is the Abaqus Example Problems Guide, which contains many solved examples that test the code with the type of problems that users are likely to solve.

To evaluate level and capabilities in the use of Abaqus/CAE, some benchmarking models, taken from Benchmarks Guide, are implemented. In particular, attention is focused on NAFEMS suite, which are composite material tests.

NAFEM R0031 tests (from "Composite Benchmarks", Feb. 2005), recommended by the National Agency for Finite Element Method and Standards (U.K.), are three tests used to demonstrate that the software is able to carry out an effective composite analysis. Basically, there are three tests:

- TEST 1: Laminated strip under three-point bending;
- TEST 2: Wrapped thick cylinder under pressure and thermal loading;
- TEST 3: Three-layer sandwich shell under normal pressure loading.

5.5.2 Model implementation and material properties

The benchmark was carried out on the test 1: Laminated strip under three-point bending. The model is visible in the figure 5.31 where, on the left we can see the xy plane model, and on the right a vertical section of the laminate. As we can observe in both figure 5.31 and 5.32, the laminate is a symmetric [0°/90°/0°/90°/0°/90°/0°] with 7 laminae of thickness 0,1 mm, except the central one which is 0,4 mm thick. The material properties are grouped in table 5.12.

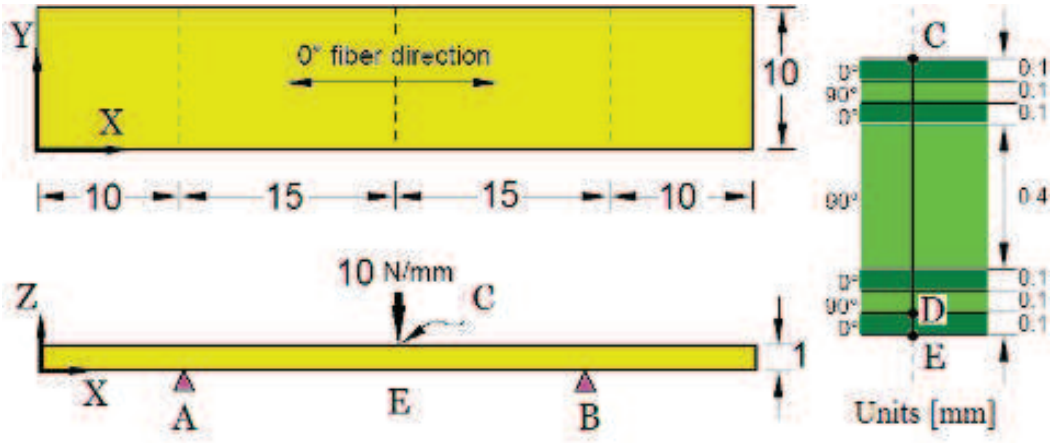

Fig. 5.31: Dimensions, section and loading of the NAFEM R0031 test 1.

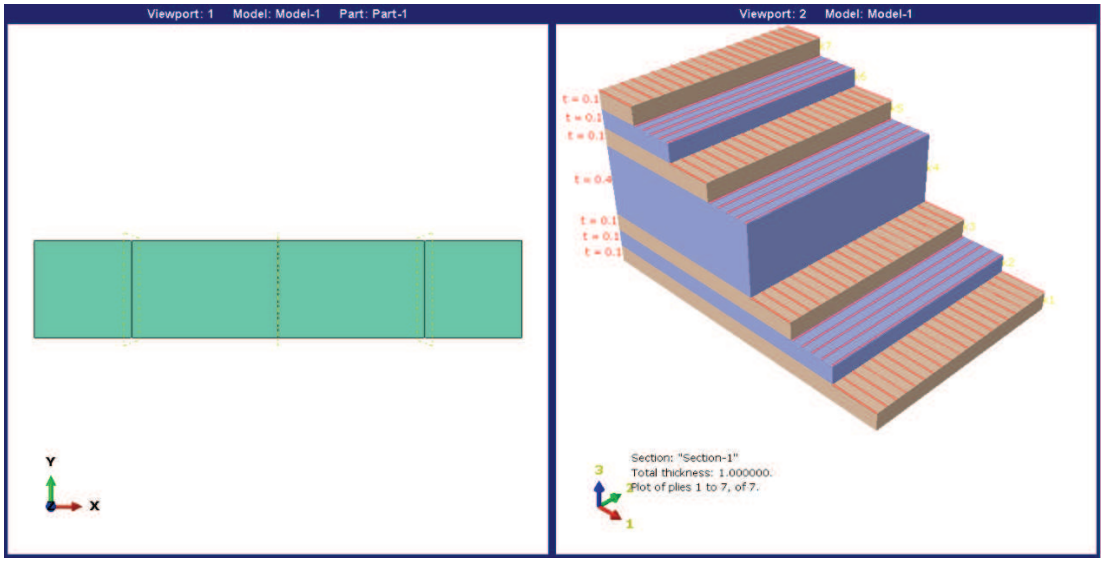

Fig. 5.32: Model and section in Abaqus.

E_1=100,0 GPa	ν_{12}=0,40	G_{12}=3,0 GPa
E_2=5,0 GPa	ν_{13}=0,30	G_{13}=2,0 Gpa
E_3=5,0 GPa	ν_{23}=0,30	G_{23}=2,0 Gpa

Tab. 5.12: Material properties of NAFEM R0031/1.

5.5.3 Boundary conditions and loads

In figure 5.33, the model is implemented with boundary conditions and applied loading. Along the two lines (A, B in fig. 5.31) the displacement of the model in z direction is

inhibited (U_3=0). The loading along the centre line is a concentrated load of 10 N/mm x 10 mm = 100 N. This force in the model is equally distributed on the nodes of the centre line, depending on the used mesh. The figure 3.6 shows a Shell S8R type element. The centre line, in this case, is composed of 15 nodes, then the concentrated force, divided by nodes, is of 100/15 = 6,667 N.

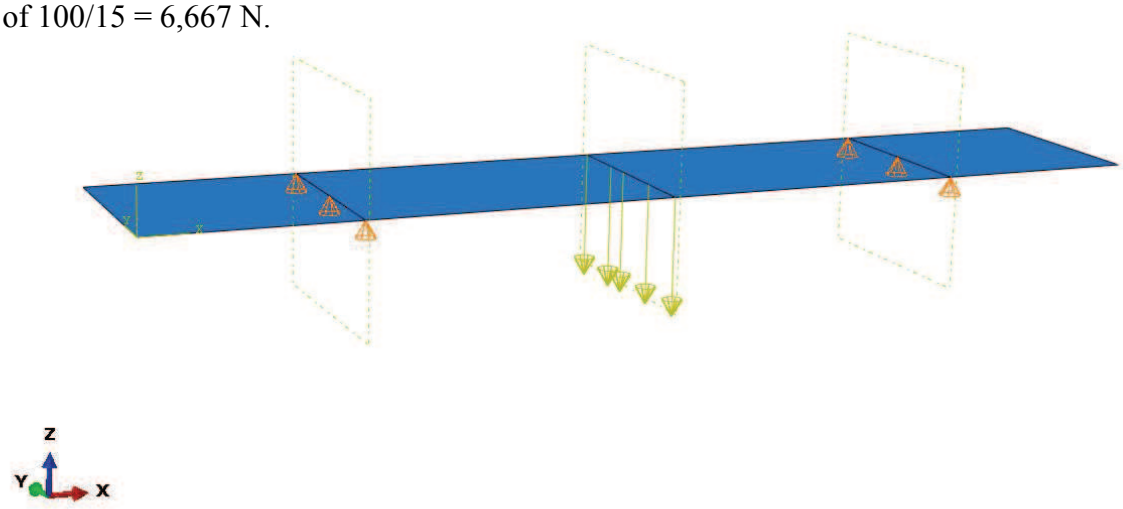

Fig. 5.33: Model with boundary conditions and loading.

The benchmarking consists in running different simulations using various element type, like C3D20 (20-node quadratic brick), a cubic-centered element with 20 nodes, or a SC6R (6-node triangular in-plane continuum shell wedge), a triangular shell element with 6 nodes. In our simulation, the choice is for two types of element: the S8R element, a shell element with 8 nodes and the S4R, same type but with 4 nodes. In this manner, we can compare results of the two simulations with nominal results of NAFEMS.

Figure 5.34 and 5.35 shows some results in the left columns, in particular S_{11} (stresses in x direction) and the displacement U_3 in the z direction, opposite to the load, for one of the simulation achieved. Table 3.2 reports results of Abaqus simulations compared with NAFEMS nominal values. As we can see, the margin error is negligible, and results are very near the NAFEMS nominal values.

Model	U_3 (mm)	S_{11} (MPa)
NAFEMS	−1,06	684
Shell, S4R	−1,068 (+0,1%)	665,9 (−2,65%)
Shell, S8R	−1,068 (+0,1%)	707,5 (+3,4%)

Tab. 5.13: Results of simulations compared with nominal values of NAFEMS.

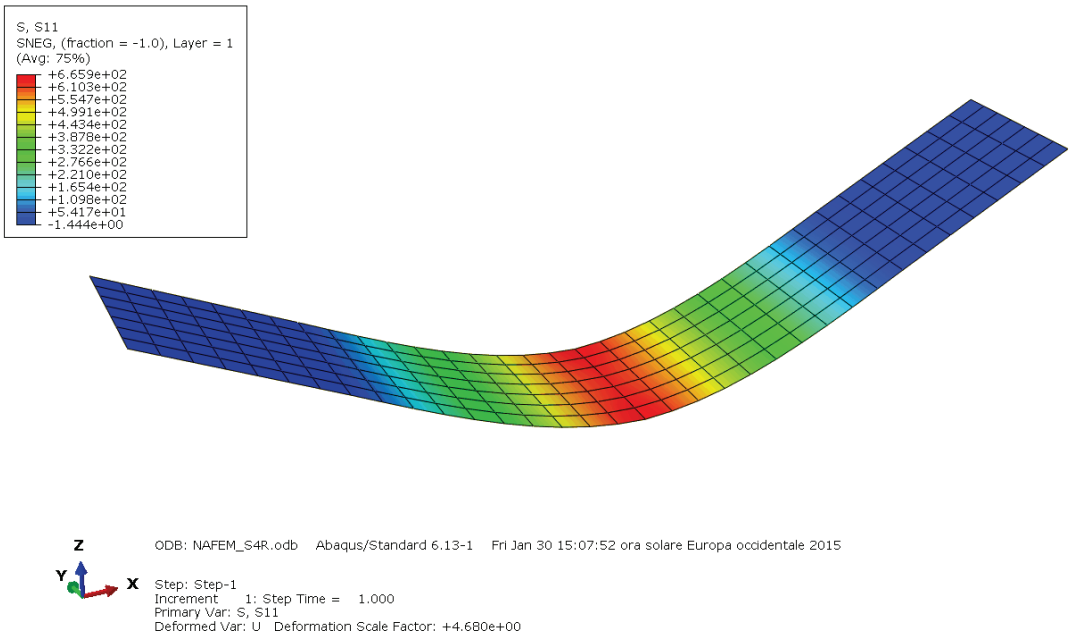

Fig. 5.34: Stress S_{11} with S4R element type.

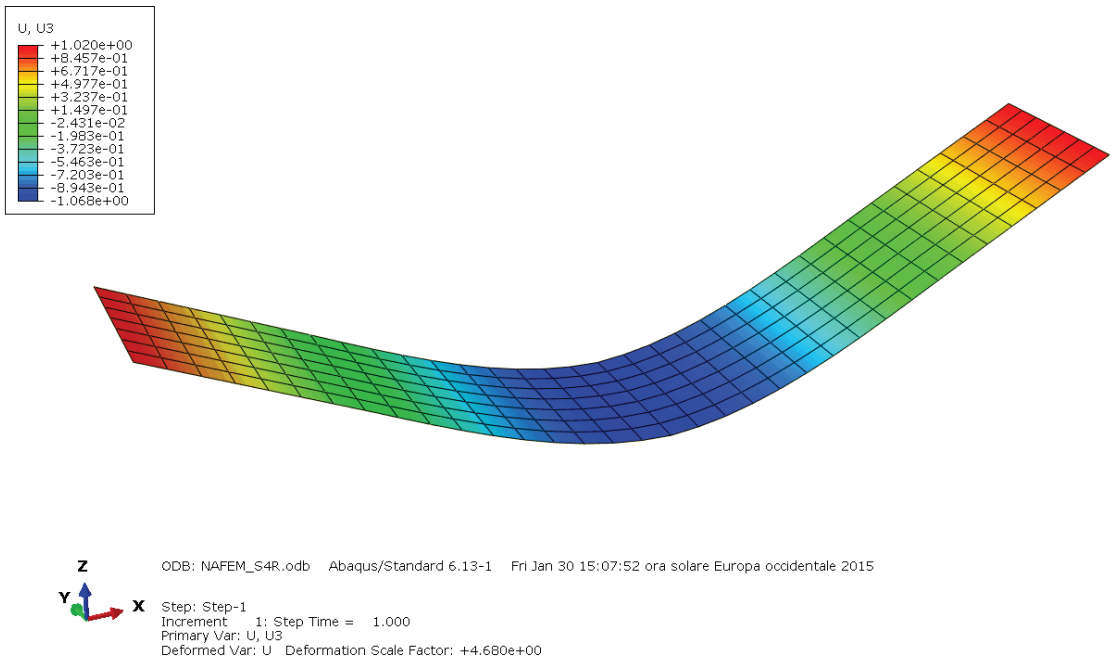

Fig. 5.35: Displacement U_3 with S4R element type.

CHAP. 6: Some Applications of The CZM: The Double Cantilever Beam and The End Notched Flexure

6.1 Introduction

In order to study the behaviour of the model described in Chapter 7, some numerical tests were performed and the results were compared with closed form solutions. These examples include the double cantilever beam test (DCB) for pure mode I, and the end notched flexure test (ENF) for pure mode II. For these tests, two beams bonded by an adhesive were considered, using the cohesive zone model. To overcome some numerical difficulties encountered, small increments were used. However, many iterations were needed to obtain a converged solution. In this chapter, experimental data were taken from literature to validate the full understanding of the Abaqus code, improving some results.

Furthermore, DCB and ENF are the basic tests to obtain the cohesive laws and determine J_{Ic} and J_{IIc}, fracture energies in mode I and in mode II respectively, used later in the next chapter, with an inverse method, to find the cohesive laws of the adhesive layer. The remaining cohesive parameters are estimated fitting the experimental and numerical load-displacement curves of the respective fracture characterization test. Usually, the pure mode III cohesive law is equalled to the pure mode II one. The detailed description of this methodology is presented in the work of [de Moura et al, 2008].

6.2 Double cantilever beam (DCB)

6.2.1 DCB with isotropic material

First of all, to validate the composite model [Dávila et al., 2001] described later in this chapter, study takes into account an isotropic model [Gonçalves et al., 1999] used by the authors to perform a non-linear analysis with the cohesive element included in Abaqus. Material properties and dimensions are shown in Tab. 6.1 and fig 6.1 respectively.

Beams		**Adhesive**			
E (N/mm^2)	**ν**	**J_{IC} (N/mm)**	**J_{IIC} (N/mm)**	**σ_t (N/mm^2)**	**τ_t (N/mm^2)**
69000	0,33	0,055	1,45	20	40

Tab. 6.1: Material properties

As we can see in fig. 6.1, DCB consists of two beams of 100 x 10 x 1,5 mm, bonded together, but only for 70 mm, keeping free the last 30 mm to simulate the initial crack length. To simulate the load, we impose an upward deflection of 11 mm; the right down edge near the

initial crack is pinned, as shown in fig. 6.1. Element type used here is C3D8I for the beams, an 8-node linear brick with incompatible modes, and COH3D8, an 8-node three-dimensional cohesive element. The interface stiffness used were taken equal to 10^7 N/mm^3 (10^{16} Pa/m). This value is a good preliminary agreement between these two conditions:

1. Small values induce large interpenetrations incompatible with physical reality;
2. Large values produce numerical errors related to the computer precision.

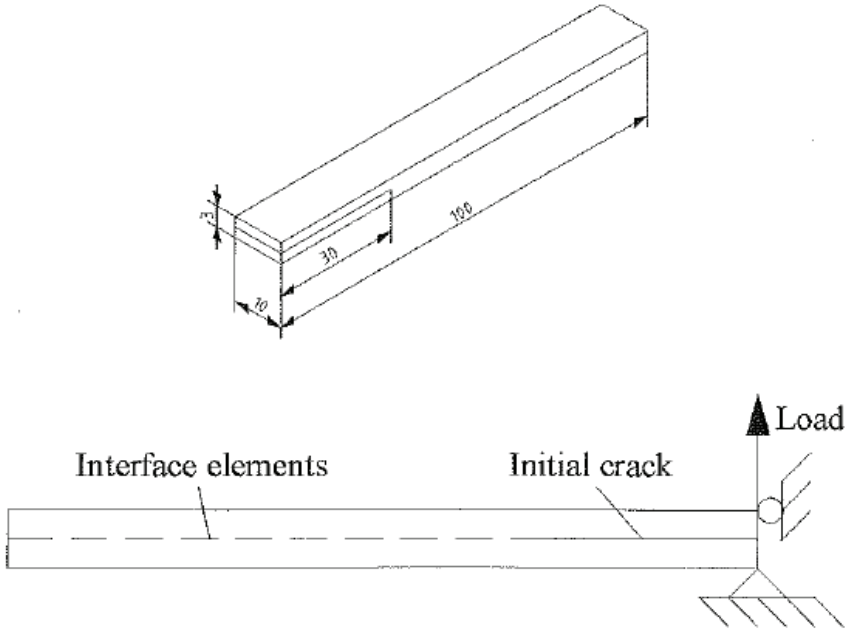

Fig. 6.1: Initial dimensions and configuration of the DCB

The optimum interface stiffnesses are the largest values that do not produce numerical problems. The interface elements are located between the two layers of solid elements along the specimen length and were previously opened to simulate the initial crack along the crack length. (Fig. 6.1). From the paper, fig. 6.2 was extracted, and the authoress's solution with the more refined mesh agrees with the closed form solution.

Abaqus model differs from the authoress's model only for the choice of constraints: we prefer keep free the model to move as reality, and the only boundary conditions used are the imposed displacements of the beams near the initial crack, in the z direction. Fig. 6.3 shows what we mean. Fig. 6.4 is the result obtained, and the similitude with the analytical model damage is clearly visible.

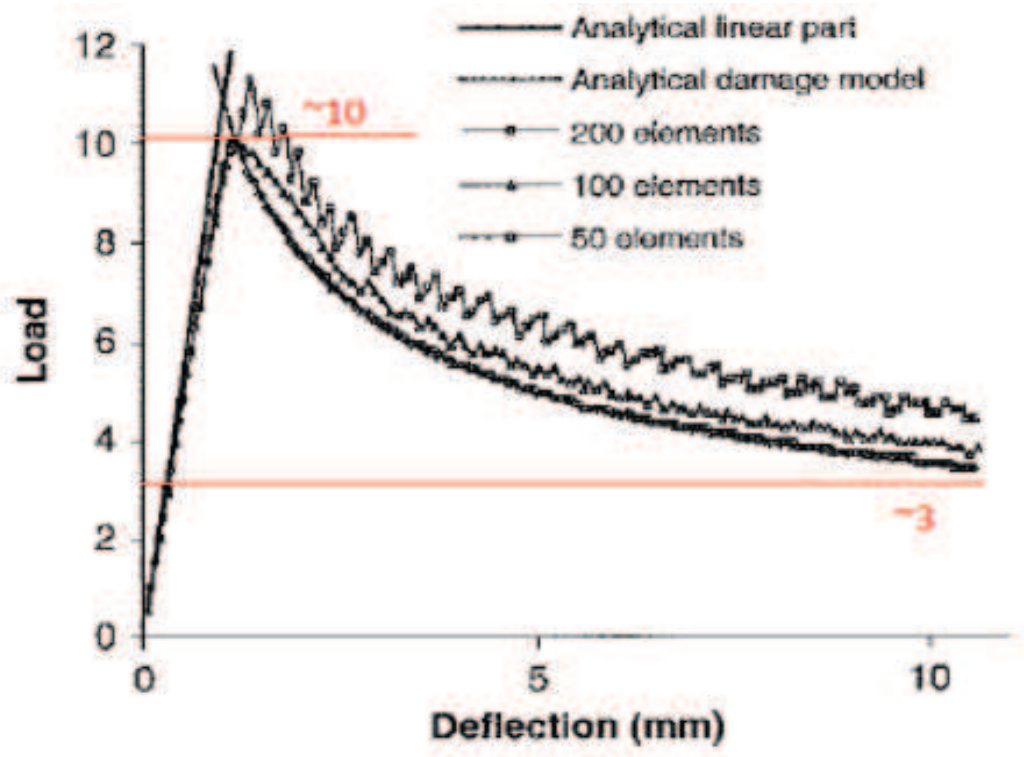

Fig. 6.2: Load/deflection at the end of the specimen for DCB model [Gonçalves et al., 1999]

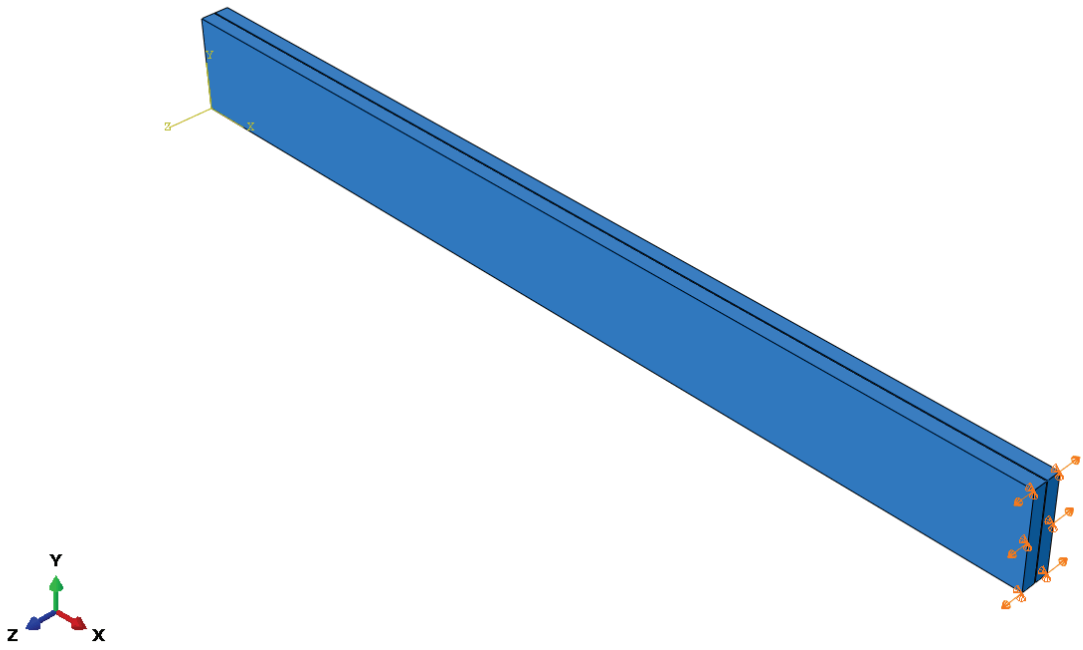

Fig. 6.3: Abaqus model with boundary conditions.

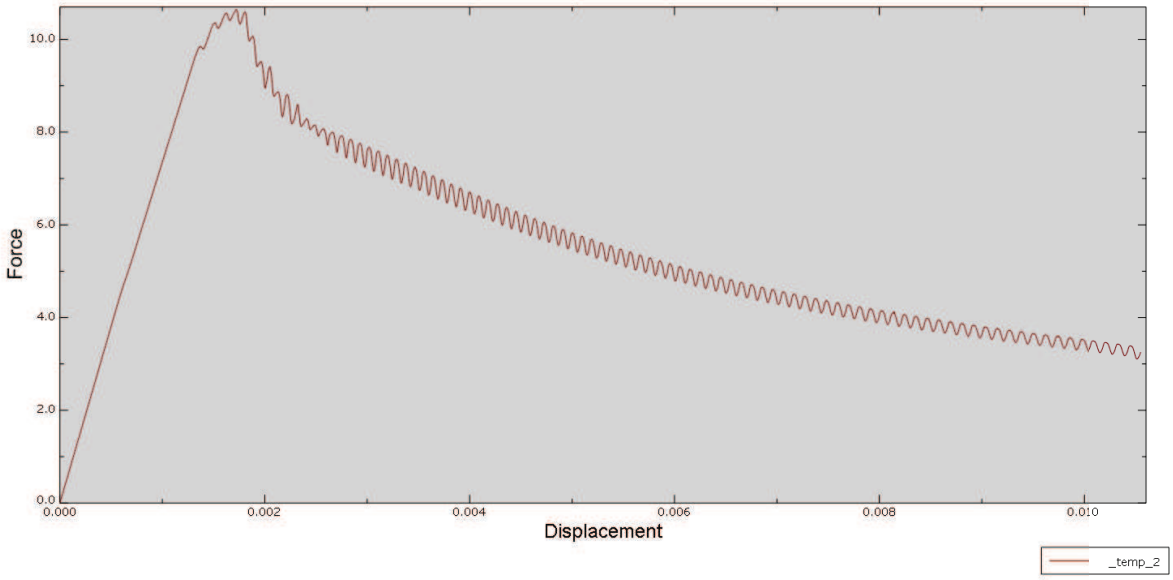

Fig. 6.4: Load/deflection at the end of the specimen for DCB model.

6.2.2 DCB with composite material

The specimen used in this case is made of a unidirectional fiber-reinforced laminate containing a thin insert at the mid-plane near the loaded end [Dávila et al., 2001]. [Morais et al. 2000] tested a 150 mm long specimen, 20 mm wide and composed of two 1,98 mm thick plies of unidirectional material (T300/977-2 CFRP). Initial crack length is 55 mm. (Fig. 6.5). The properties of the material are shown in Table 6.2, and the properties of the interface in Table 6.3. Figure 6.5 and table 6.4 resumes, on the other hand, geometry and dimensions of the specimen used for the simulation respectively.

E_1=150,0 GPa	ν_{12}=0,25	G_{12}=6,0 GPa
E_2=11,0 GPa	ν_{13}=0,25	G_{13}=6,0 GPa
E_3=11,0 GPa	ν_{23}=0,45	G_{23}=3,7 GPa

Tab. 6.2: Graphite/Epoxy material properties

J_{Ic} (N/mm)	J_{IIc} (N/mm)	T (MPa)	S (MPa)	K_p (Pa/m)
0,268	1,45	30	40	10^{15}

Tab. 6.3: Interface Graphite/Epoxy material properties

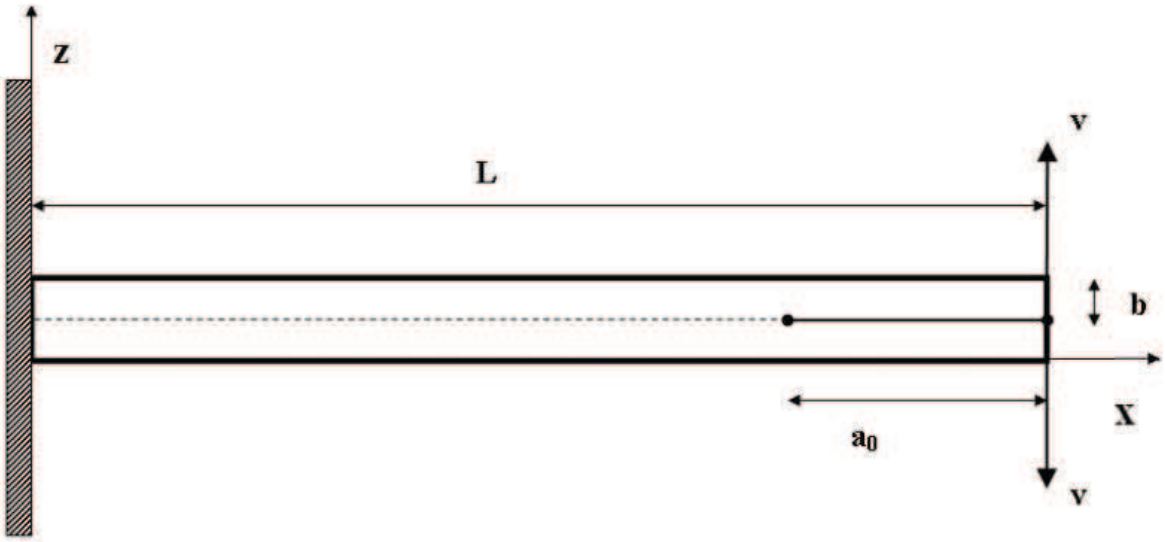

Fig. 6.5: Geometry of the specimen

	DCB T300/977-2
L	150 mm
b	1.98 mm
w	20 mm
a_0	55 mm

Tab. 6.4: Specimen dimensions

The Abaqus finite element model developed by Dávila is shown deformed in fig. 6.6, and consists of two layers of C3D8I incompatible mode 8 node elements. C3D8I elements are superior in bending to other low-order continuum elements. One hundred and twenty elements were used along the span of the model shown in fig. 6.6.

A plot of reaction force as a function of the displacement d, obtained by [Dávila et al. 2001] is shown in fig. 6.7. The beam solution was developed by [Mi and Crisfield 1996] for isotropic adherend materials and using plane stress assumptions.

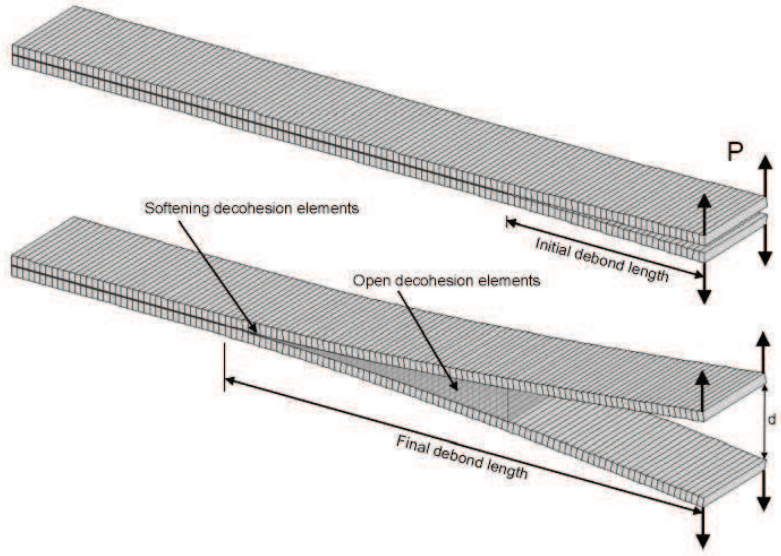

Fig. 6.6: Model of DCB test specimen [Dávila et al., 2001]

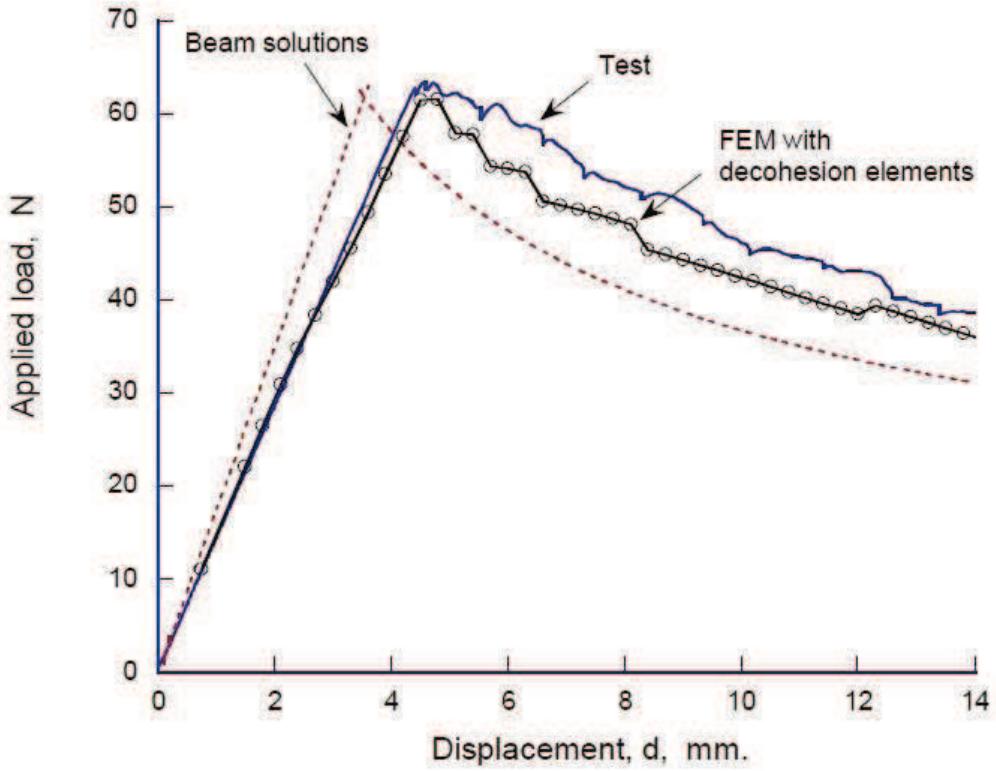

Fig. 6.7: Load-deflection response of DCB test made by [Dávila et al. 2001].

As made before for the isotropic DCB test (par. 6.2.1), the model is reproduced to validate the comprehension of the CZM. In this case, the model uses same geometry and dimensions, same material properties and interface properties. The difference from the Dávila model is

made on the mesh, which is visible in Fig. 6.8. That is, elements are doubled respect to the original mesh used by Dávila.

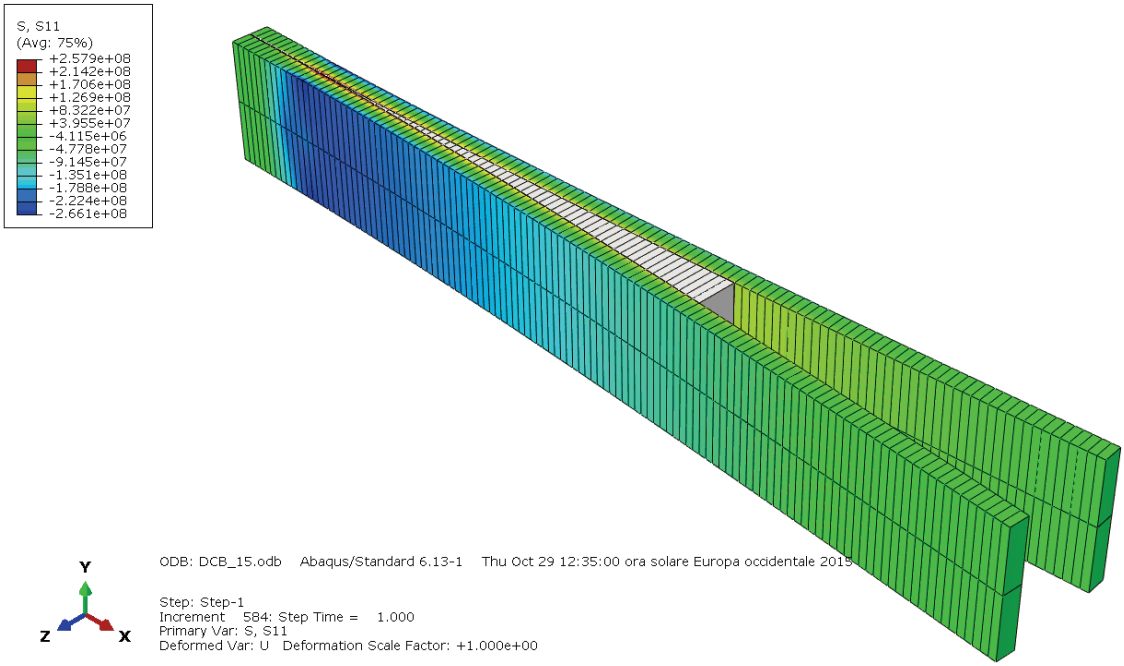

Fig. 6.8: Mesh of deformed model

Cohesive elements COH3D8 with 8 nodes are used on the bonded interface between the two composite specimens. Result of the simulation is shown in fig. 6.9, where we can see the extreme similitude with the authoress's model.

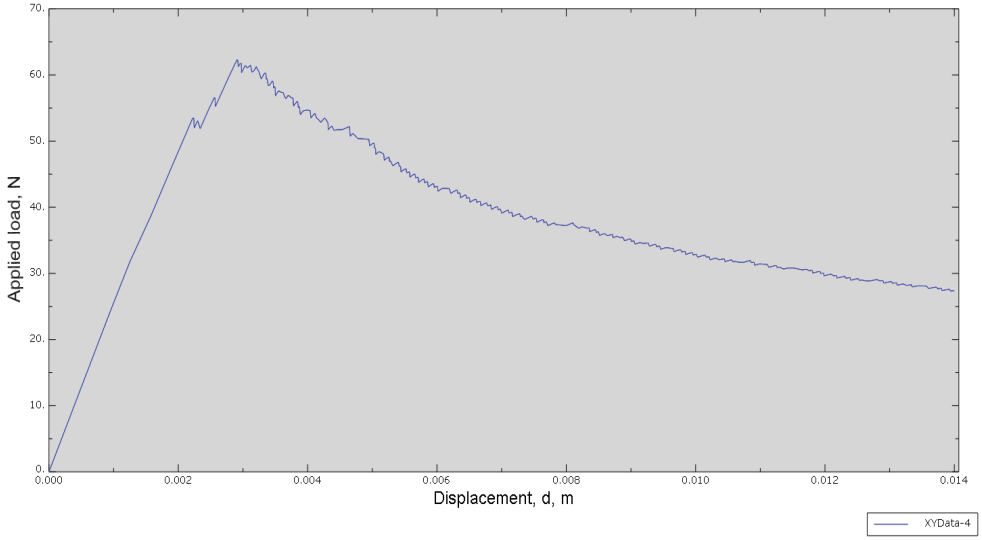

Fig. 6.9: Load-deflection response of DCB test.

6.3 End Notched Flexure (ENF)

6.3.1 ENF with isotropic material

The End Notched Flexure is a test for pure mode II. Geometry and dimensions of the specimen are the same of DCB test with isotropic material (Par 6.2.1). Figure 6.10 shows the loading and boundary conditions considered for the analysis. The mesh with 100 elements [Gonçalves et al., 1999] along the beam was considered in the simulation. Material properties and dimensions are shown in Tab. 6.1 and fig 6.1 respectively.

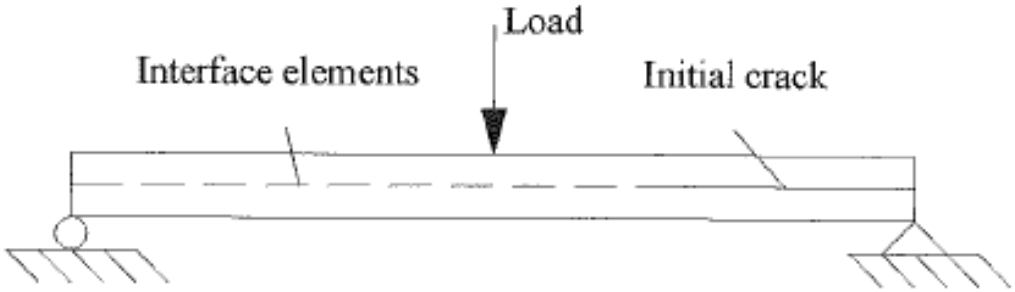

Fig. 6.10: Initial dimensions and configuration of the ENF.

The next figure 6.11 shows results obtained by the authors, where the numerical load/deflection curve is also compared with closed form solutions from [Mi and Crisfield, 1996] and [Mi et al. 1998].

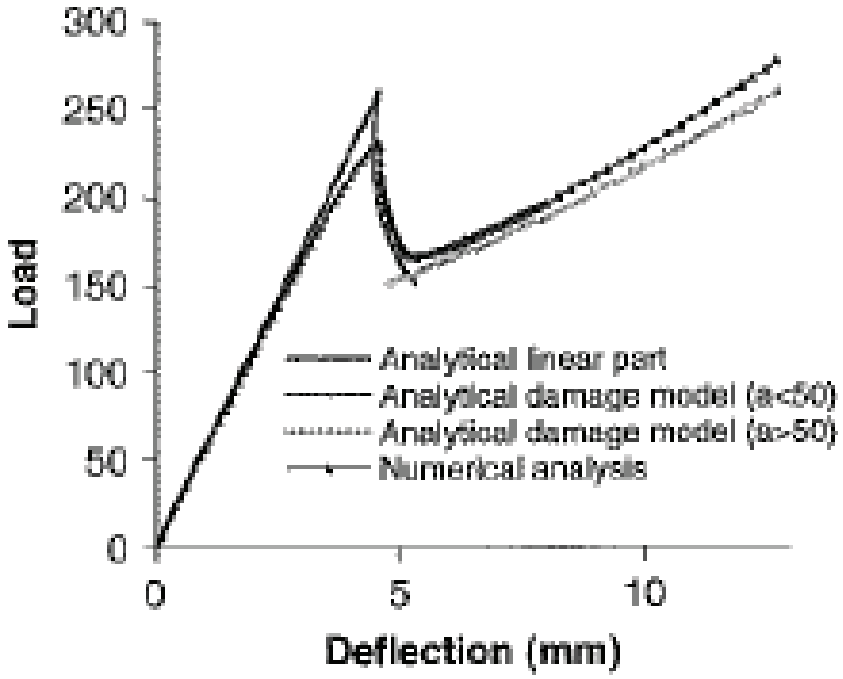

Fig. 6.11: Load/deflection at the end of the specimen for EBF model [Gonçalves]

Fig. 6.12 is the result of Abaqus model, whereas fig 6.13 shows the deformed model after total displacement. As we can see, Abaqus model is in good agreement with the authoress's model.

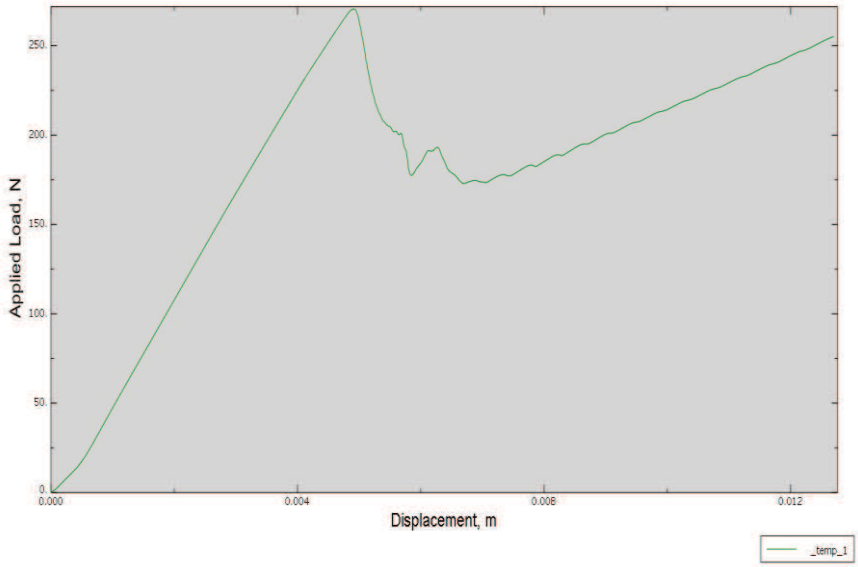

Fig. 6.12: Load/deflection at the end of the specimen for ENF Abaqus model

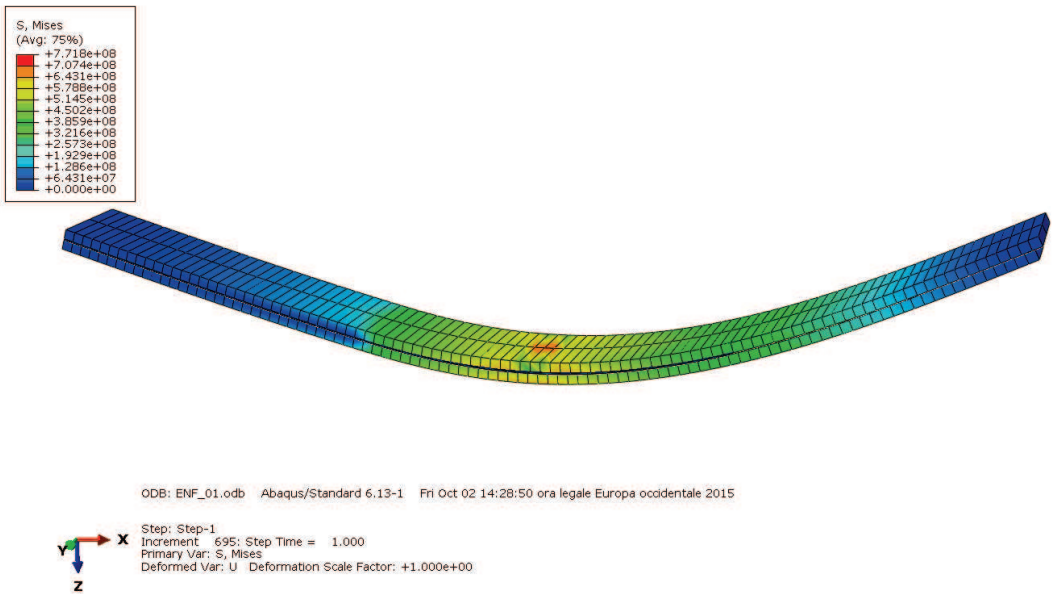

Fig. 6.13: Deformed model of ENF with Abaqus.

6.3.2 ENF with composite material

The previous cited paper [Gonçalves et al., 1999] analyses only isotropic material. Results were compared with closed form solutions [Mi and Crisfield, 1996 and Mi et al., 1998], and the authors stated that the finite element method is in close agreement with the analytical results (fig. 6.11). To confirm the goodness of the previous model, the next simulation shows

that it is possible to obtain some significant results for the composite material using the ENF model of par. 6.3.1. Fig. 6.14 shows that the displacement value at which the crack begins is more or less the same value of fig. 6.12. In fact, due to material properties of CFRP, a bigger value is expected, and that is what we can see in fig. 6.14. Nevertheless, the max load value at which the crack begins is lower, due to different stiffness of composite material vs isotropic one along the adhesive interfaces. Then, further investigations are needed to validate the behavior of ENF composite model through some experimental tests.

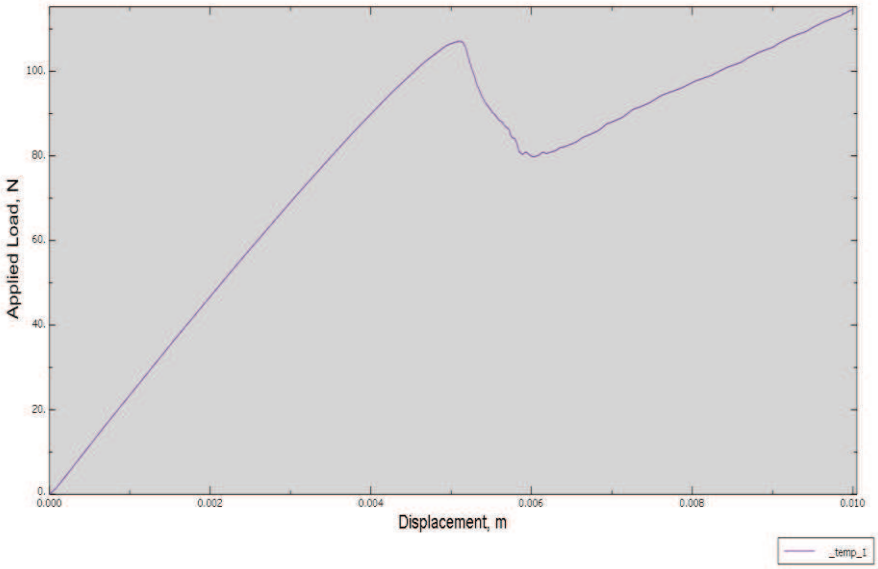

Fig. 6.14: Load/deflection at the end of the specimen for ENF composite model.

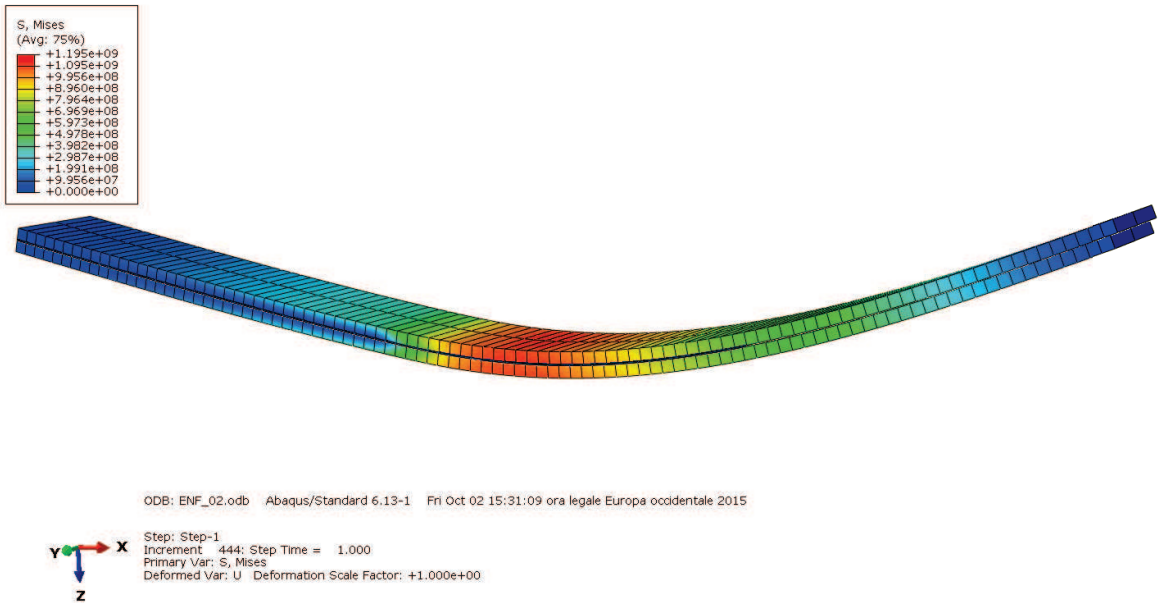

Fig. 6.15: End Notched Flexure Abaqus model.

CHAP. 7: An Innovative Model of Bonded Repair

7.1 Introduction

In this chapter, a numerical study of the tensile behaviour of three-dimensional carbon epoxy adhesively bonded single strap repair is analysed. Particularly, simulations, made with Abaqus®, are focused to understand the weak bond behaviour, as explained later in this chapter. The choice of the tensile stresses is due to the fuselage behaviour, which is subjected, in its operative life, to stresses known as fuselage hoop stresses. In this work, residual stresses of a single-strap bonded repair with a fixed displacement are calculated, and a correlation with different weak bond configurations is done.

Experimental curves are taken from an article written in 2009 by [Campilho et al.]. In this paper, the failure mode, elastic stiffness and strength were evaluated experimentally for different overlap lengths and patch thicknesses on the SS and DS repair configurations, allowing the authors to optimize the repair parameters. All the simulations are performed in Abaqus®, to obtain the elastic stiffness and the patch debonding load, and are used to understand the experimental mechanical behaviour of the repair. The adhesive layer is simulated with cohesive elements including a mixed-mode cohesive damage model with trapezoidal traction-separation laws in pure modes I and II. The choice of trapezoidal traction-separation cohesive laws between stresses and relative displacements is considered to accurately reproduce the behaviour of thin ductile adhesive layers in mode I and mode II. These laws are determined by an inverse method, which consists on obtaining the fracture energies (J_{iC}, $i=I, II$) from the double cantilever beam (DCB) and end-notched flexure (ENF) tests for the pure mode I and II laws, respectively, and estimating the remaining cohesive parameters fitting the experimental load-displacement $(P\text{-}\delta)$ curves of the respective fracture characterization test. The pure mode III cohesive law is equal to the pure mode II one. The authors have found that this numerical methodology is adequate to reproduce the experimentally observed behaviour of these repairs.

As written in chapter 1, repairs of primary aircraft structures are restored by means of mechanically fastened patches, which present some disadvantages, such as the weight penalty and, primarily, significant stress concentrations at localized regions of the composite structure, cause of local overloads and damage initiation. Adhesively bonded repairs overcome these limitations. The strap repair technique consists on executing a circular hole to remove the damaged material, followed by the adhesive bonding of circular patches on one side (single strap, SS) or both sides (double strap, DS) of the laminate.

To analyse the behaviour of bonded repairs, the Cohesive Zone Model technique is coupled to FEM models, simulating damage onset and growth in thin adhesive layers. The advantage of this methodology is its mesh independency, since damage growth is ruled by energetic criteria. The numerical analysis uses a plane-strain eight-node element, with a CZM to simulate damage initiation and growth. In his paper, Campilho focussed on the effect of the overlap length and the patch thickness on the stress distributions in the adhesive layer and the residual strength of the repairs. This work, otherwise, assumes as a start point, the best performance of the SS bonded repair, and analyses the correlations between a perfect bond and a weak bond. In effect, one of the most important conclusions of Campilho's article was related to the non-proportional strength improvement of the repair as a function of overlap length, i.e. above a determined patch diameter, the strength improvement was minimal. Results found a good correlation with experiments made by authors.

Experimental and numerical studies take into account the tensile behaviour of a three-dimensional CFRP adhesively bonded strap repairs of $[0_2, 90_2]_s$ lay-up laminate. The choice of the overlap length and the patch thickness falls, respectively, on $L_o = 5\ mm$ and $t_H = 1{,}2\ mm$ performed on a Single Strap repair (Fig. 7.2). The open-hole simulation was also evaluated for comparison. The adhesive parameters are taken from Araldite® 2015 (Huntsmann, Basel, SWITZERLAND) data sheet, and provide the cohesive parameters in pure mode I and II. Araldite® 2015 is also a good choice for its temperature strengthen ($25 \div 27\ MPa\ @ -60°C \div -40°C$), since aircrafts fly usually where temperature are very low, namely -50°C at 33000 ft [Araldite® 2015 datasheet]. Instead, the laminates and patches lamina mechanical properties are extracted from Hexcel® Texipreg HS 160 RM (SEAL®, Legnano, ITALY) data sheet.

7.2 Cohesive damage model

7.2.1 Model description

For the simulation of a 0,2 mm thickness ductile layer of Araldite® 2015, we consider a mixed-mode (I+II+III) cohesive damage model implemented within interface finite elements. Figure 7.1 shows the trapezoidal law between stresses (σ) and relative displacements (δ_r) through homologous points of the interface elements with zero thickness. The behaviour of thin ductile adhesive layers in mode I and mode II is accurately reproduced with these type of laws, as seen in chapter 4. Before damage onset, the constitutive relationship is:

$$\boldsymbol{\sigma = D\delta_r} \qquad 7.1$$

where **D** is a stiffness diagonal matrix. Observing figure 7.1, in the pure-mode model, the material softens progressively after $\delta_{1,i}$, wiz the material undergoes damage. The damage parameter varies from zero (undamaged) to one (complete loss of stiffness) as the material deteriorates.

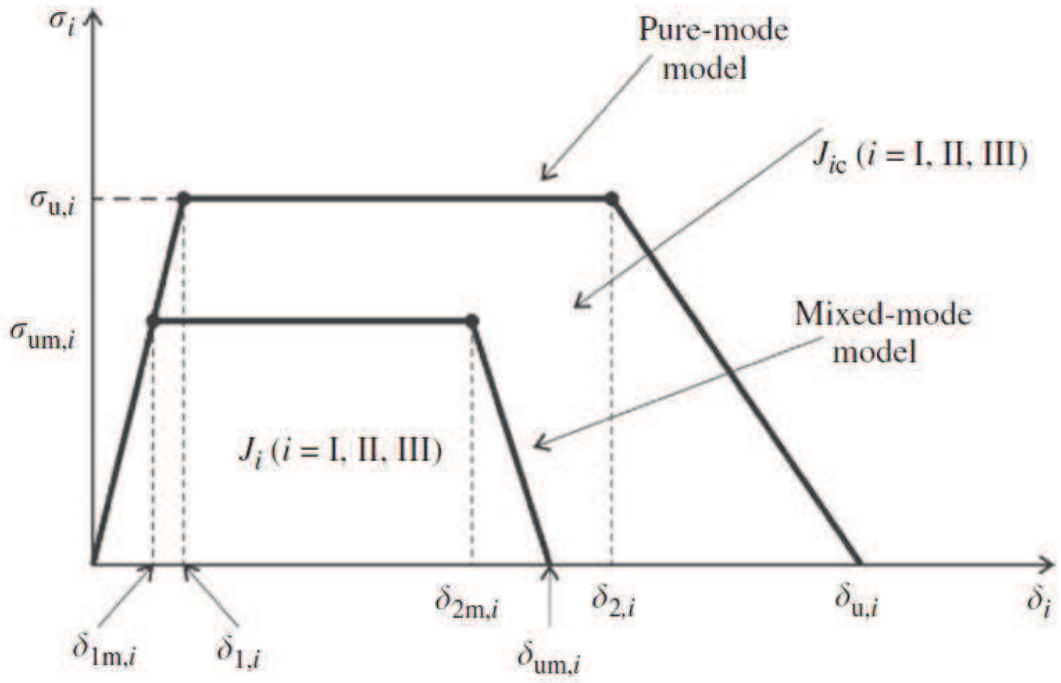

Fig. 7.1: Trapezoidal softening law for pure-mode and mixed-mode.

The softening relationship can be written as:

$$\boldsymbol{\sigma} = (\boldsymbol{I} - \boldsymbol{E})\boldsymbol{D}\boldsymbol{\delta_r} \tag{7.2}$$

where I is the identity matrix and E is a diagonal matrix the damage parameter e_i in the position corresponding to mode i (i = I, II, III). The damage parameter, in the plateau region, is defined as:

$$e_i = 1 - \frac{\delta_{1,i}}{\delta_i} \tag{7.3}$$

And in the stress softening part of the curve as:

$$e_i = 1 - \frac{\delta_{1,i}(\delta_{u,i} - \delta_i)}{\delta_i(\delta_{u,i} - \delta_{2,i})} \tag{7.4}$$

where δ_i is the current displacement and $\delta_{2,i}$ is the stress softening displacement in each mode. The maximum displacement $\delta_{u,i}$ is reached when the complete failure occurs, and is obtained equating the area under the softening curve to the fracture energy in each mode (J_{iC}). Then we have:

$$J_{i,C} = \frac{\sigma_{u,i}}{2}\left(\delta_{2,i} - \delta_{1,i} + \delta_{u,i}\right) \tag{7.5}$$

where $\sigma_{u,i}$ corresponds to the local strength in each pure mode.

On the other hand, structures are under mixed-mode load, and then the formulation includes a mixed-mode damage model, an extension of the pure-mode model seen in fig. 5.1. Recalling equation 4.15, here we use a damage onset predicted by the quadratic stress criterion:

$$\left(\frac{\sigma_I}{\sigma_{u,I}}\right)^2 + \left(\frac{\sigma_{II}}{\sigma_{u,II}}\right)^2 + \left(\frac{\sigma_{III}}{\sigma_{u,III}}\right)^2 = 1 \qquad if\ \sigma_I > 0$$

$$\left(\frac{\sigma_{II}}{\sigma_{u,II}}\right)^2 + \left(\frac{\sigma_{III}}{\sigma_{u,III}}\right)^2 = 1 \qquad if\ \sigma_I \leq 0 \tag{7.6}$$

where σ_i (i=I, II, III) are the stresses in each mode, assuming that normal compressive stresses do not include damage. Combining with equation 7.1, we have an equation as a function of the relative displacements:

$$\left(\frac{\delta_{1m,I}}{\delta_{1,I}}\right)^2 + \left(\frac{\delta_{1m,II}}{\delta_{1,II}}\right)^2 + \left(\frac{\delta_{1m,III}}{\delta_{1,III}}\right)^2 = 1 \tag{7.7}$$

where $\delta_{1m,i}$ (i=I, II, III) are the relative displacements corresponding to damage initiation. Using equation 4.18 to define an equivalent mixed-mode displacement [Camanho and Davila, 2002], we can write:

$$\delta_m = \sqrt{\delta_I^2 + \delta_{II}^2 + \delta_{III}^2} \tag{7.8}$$

and mixed-mode ratios (i = I, II, III):

$$\beta_i = \frac{\delta_i}{\delta_I} \tag{7.9}$$

Combining finally equations 7.7, 7.8, 7.9, we obtain the equivalent mixed-mode relative displacement at the onset of the softening process δ_{1m}:

$$\delta_{1m} = \sqrt{\frac{1+\beta_{II}^2+\beta_{III}^2}{\frac{1}{\delta_{1,I}^2}+\frac{\beta_{II}^2}{\delta_{1,II}^2}+\frac{\beta_{III}^2}{\delta_{1,III}^2}}} \tag{7.10}$$

A similar procedure is used to determine δ_{2m} with the same displacements criterion (7.7). The equivalent mixed-mode relative displacement at the onset of the softening process δ_{2m} is:

$$\delta_{2m} = \sqrt{\frac{1+\beta_{II}^2+\beta_{III}^2}{\frac{1}{\delta_{2,I}^2}+\frac{\beta_{II}^2}{\delta_{2,II}^2}+\frac{\beta_{III}^2}{\delta_{2,III}^2}}} \tag{7.11}$$

The simulation considers a linear fracture energetic criterion (equation 4.23) for the crack growth, written as:

$$\frac{J_I}{J_{IC}} + \frac{J_{II}}{J_{IIC}} + \frac{J_{III}}{J_{IIIC}} = 1 \tag{7.12}$$

When Eq. 7.12 is satisfied, damage growth occurs and stresses are completely released. The area of the minor trapezoid of figure 7.1 gives the energy released in each mode at complete failure, written as:

$$J_i = \frac{\sigma_{um,i}}{2}\left(\delta_{2m,i} - \delta_{1m,i} + \delta_{um,i}\right) \tag{7.13}$$

Combining Eqs. 7.8, 7.9, 7.12 and 7.13, we obtain:

$$\delta_{um} = \frac{2\left(1+\beta_{II}^2+\beta_{III}^2\right)J_{IC}J_{IIC}J_{IIIC} - \delta_{1m}(\delta_{2m}-\delta_{1m})\left(d_I J_{IIC}J_{IIIC} + d_{II}\beta_{II}^2 J_{IC}J_{IIIC} + d_{III}\beta_{III}^2 J_{IC}J_{IIC}\right)}{\delta_{1m}\left(d_I J_{IIC}J_{IIIC} + d_{II}\beta_{II}^2 J_{IC}J_{IIIC} + d_{III}\beta_{III}^2 J_{IC}J_{IIC}\right)} \tag{7.14}$$

which corresponds to the equivalent mixed-mode ultimate relative displacement. The parameters d_i *(i=I, II, III)* are the stiffness components of the diagonal matrix **D**. It is noteworthy that, when using a CZM to simulate damage initiation and growth, stresses at the concentration or singularity regions do not exceed the values of $\sigma_{u,i}$ (i = I, II, III, Fig. 7.1). Using this methodology, however, the strength prediction is not mesh sensitive if several points undergo the softening process in a given increment. When the quadratic stress criterion of Eq. 7.8 is satisfied at a given integration point (under mixed-mode loading), the softening process initiates, simulating material degradation and leading to a stress plateau at this point and consequent stress redistribution to the neighbouring integration points. It is desirable that at least 4 or 5 integration points are under softening, to ensure that a stable propagation occurs, thus promoting a smooth load redistribution (Fig. 7.1). This issue is fundamental to obtain mesh independent results and was guaranteed in all the numerical simulations.

7.2.2 Cohesive parameters

In the previous paragraph, the trapezoidal mixed-mode CZM presented was used in the numerical models to simulate a 0,2 mm thickness adhesive layer of the epoxy adhesive Araldite 2015. The thickness of the adhesive layer (t_A) is introduced in the stiffness matrix D. In fact, the stiffness components in pure modes I and II (d_I and d_{II}) are calculated from the ratio between the elastic modulus of the material in tension or shear (E or G, respectively) and t_A. In all the simulations, the pure mode III cohesive law is the same of the pure mode II one. Now, it is necessary to know the respective local strength $\sigma_{u,i}$, second inflexion point $\delta_{2,i}$ and fracture energy J_{ic} to fully characterize the cohesive laws in pure modes I and II. [Campilho et al., 2005, 2008] and [Gonçalves et al., 2003] published some works assuming adhesive bulk properties for these quantities. However, in these geometries, the strain constraining effect of the adherends and the respective typical mixed-mode crack propagation justify a known difference between the adhesive properties as a bulk or as a thin layer [Andersson et al., 2004, Leffler et al., 2007, Hogberg et al., 2006]. As written in 7.1, to account for this difference, the cohesive laws of the adhesive layer were determined using an inverse method. The detailed description of this methodology is presented in the work of [de Moura et al., 2008], and it consists on an initial determination of J_{Ic} or J_{IIc} from DCB or ENF tests, respectively, using a proper data reduction scheme. The value of J_{ic} is inputted in the corresponding pure mode cohesive law in the numerical DCB or ENF model, which presents the same dimensions of the specimen it is simulating. Typical values for the local strength $\sigma_{u,I}$ and second inflexion point $\delta_{2,i}$ are initially considered. These quantities are then

determined using a fitting procedure between the numerical and experimental load–displacement (P–δ) curves of the respective fracture characterization test. Table 7.1 presents the cohesive parameters of pure modes I and II laws used to simulate the adhesive layer. The elastic modulus of the adhesive layer in tension and shear were determined experimentally [Marques et al., 2008], with bulk tensile and thick adherend shear test (TAST) tests, respectively (E = 1850 MPa; G = 650 MPa).

	i	J_{ic} (N/mm)	$\sigma_{u,i}$ (MPa)	$\delta_{2,i}$ (mm)
Pure mode	I	0,43	23,0	0,0187
	II	4,70	22,8	0,1710

Table 7.1: Cohesive parameters in pure mode I and II of a 0,2 mm thickness adhesive layer of Araldite® 2015.

7.3 Experimental work

Simulations analysed in this thesis are based on experimental works from literature. In particular, experiments are extracted from [Campilho et al., 2009], and are based on geometry and dimensions of figure 7.2.

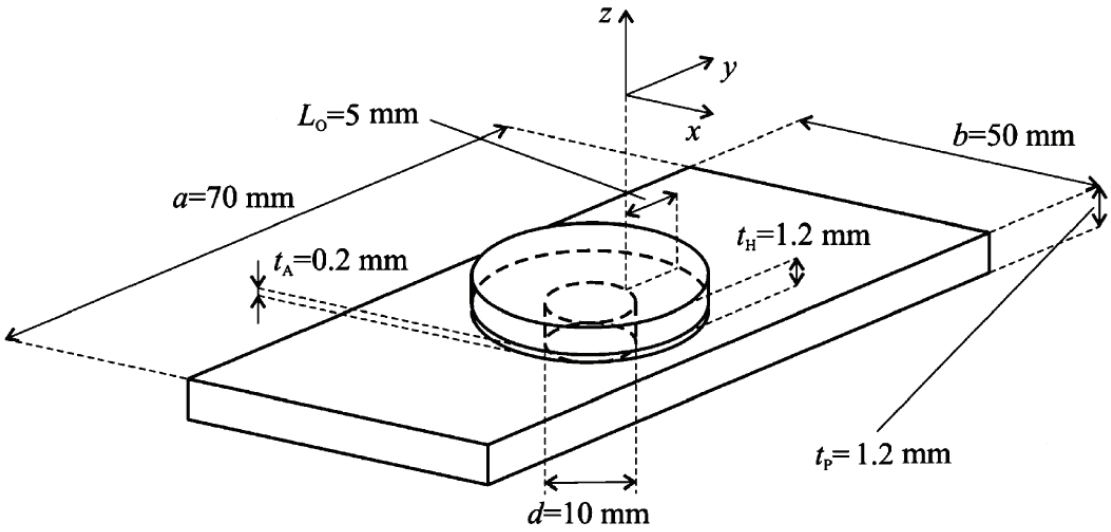

Fig. 7.2: SS repair geometry and initial dimensions.

In this figure, a is the specimen length between grips (the total length of the specimen, including edges clamped in the grips, is 150 mm), b is the width of the specimen, d is the hole diameter, t_A is the adhesive thickness. The patch is a circular cylinder of diameter L_o and thickness t_H. In Campilho's article, the influence of the overlap length L_o and the patch

thickness t_H on the adhesive stresses, failure mode, elastic stiffness and residual strength of the repairs was evaluated. Experiments include, for comparison, results from open-hole specimen, without patch. The lay-up selected for the laminates is $[0_2, 90_2]_s$. These laminates were manufactured using CFRP pre-preg (Texipreg HS 160 RM from SEAL®, Legnano, ITALY) with 0,15 mm of ply thickness. Mechanical properties of a unidirectional lamina are reported in table 7.2. Surfaces of specimens are prepared with 180 grit sandpaper and cleaned with acetone prior to bonding patches, in order to avoid adhesive failures. As mentioned in paragraph 7.2, the 0,2 mm adhesive layer is made of Araldite® 2015 (Huntsmann, Basel, SWITZERLAND). The specimens were tested under displacement control (0,5 mm/min) on an Instron® 8801 (Norwood, USA) hydraulic machine equipped with a 100 kN load cell. At least three valid tests for each geometry were always obtained.

E_1 = 1.09E+05 MPa	ν_{12} = 0.342	G_{12} = 4315 MPa
E_2 = 8819 MPa	ν_{13} = 0.342	G_{13} = 4315 MPa
E_3 = 8819 MPa	ν_{23} = 0.380	G_{23} = 3200 MPa

Table 7.2: Laminates and patches lamina mechanical properties.

Figure 7.3 shows results obtained with the specimen described above.

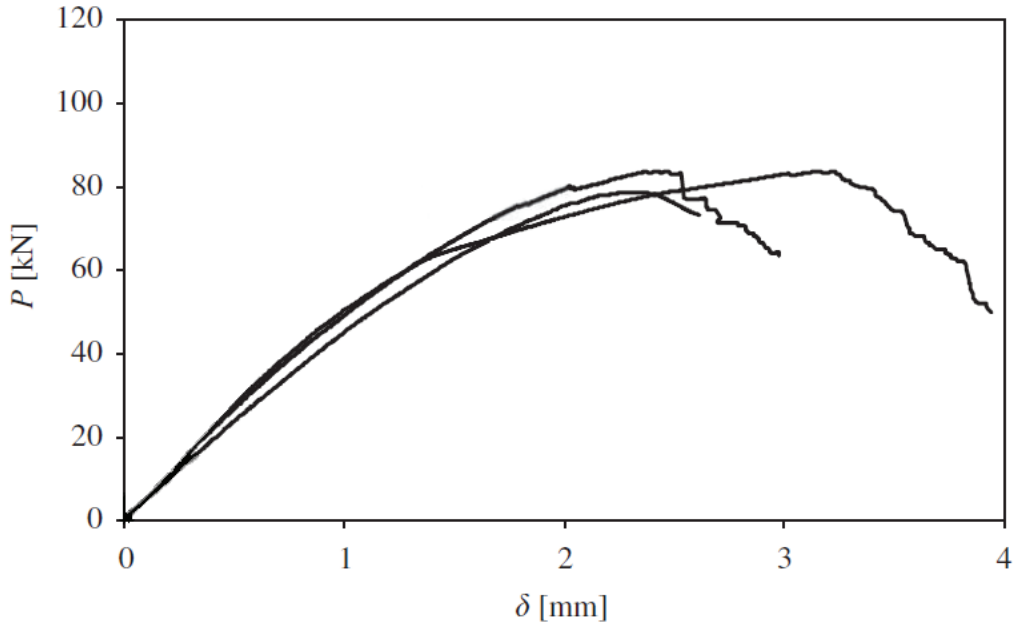

Fig. 7.3: Experimental P-δ curves comparison for the L_o = 5 mm SS repairs.

7.4 Finite Element Analysis

7.4.1 Model implementation

A geometrical and material non-linear numerical analysis was performed in ABAQUS® (from Dassault Systèmes, Suresnes, FRANCE), to simulate the behaviour of a single sided bonded repair, considering the specimen described in Figure 7.2, with fixed L_o = 5 mm and t_H = 1,2 mm. The numerical model was built using an 8-node linear brick element (C3D8I) with incompatible modes for the laminates and the patches, while the adhesive used an 8-node three-dimensional cohesive element (COH3D8). Damage was considered to occur only at the adhesive layer, simulated by the trapezoidal CZM presented in chapter 7.2. Figure 7.5 and 7.6 show a detail of the mesh refinement used in the models. Laminate and patch were modelled as orthotropic elastic materials, using one-element through thickness for each set of adjacent and equally oriented plies (Fig. 7.4). As written later in this chapter, laminate is a $[0_2, 90_2]_s$ made of 8 symmetric plies oriented as we can see in the figure below.

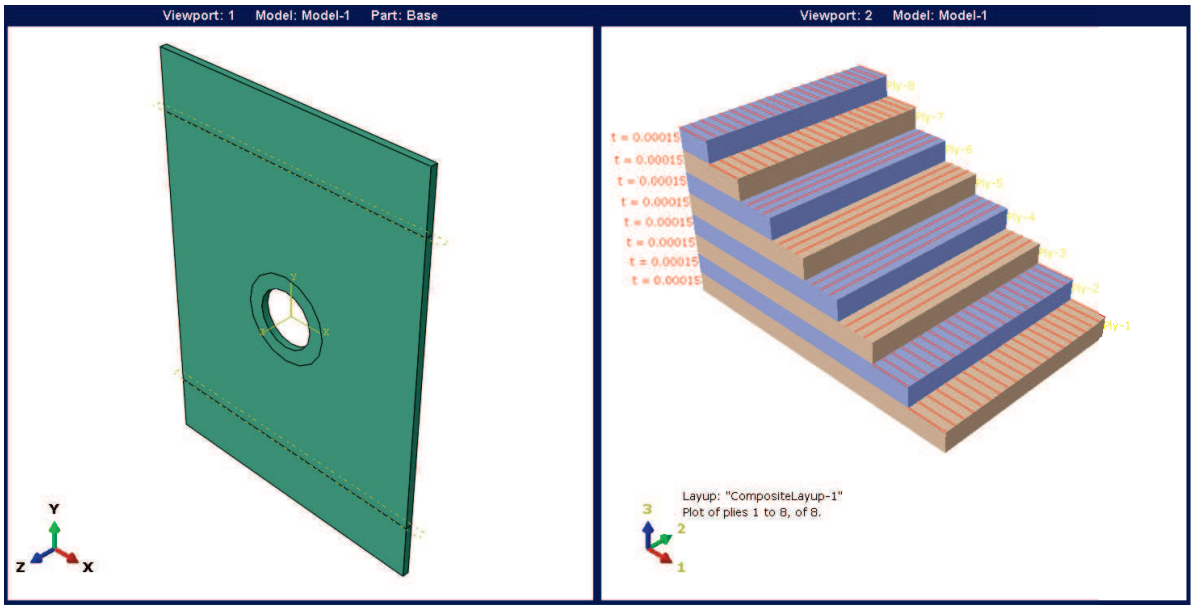

Fig. 7.4: Exploded drawing of the laminate.

Fig. 7.5 and 7.6 show the mesh used for the specimen. Particularly, the specimen without patch is made of 1234 linear hexahedral elements of type C3D8I, with a sweep technique, which uses a medial axis algorithm to minimize the mesh transition. Total number of nodes of this part of the model is 2628. The patch uses the same type of element and the same sweep technique, but here an advancing front algorithm is used for the mesh, with a mapped meshing where appropriate. Total number of elements is 455, whereas total number of nodes is 976. Adhesive mesh has the same specimen properties (sweep technique and medial axis algorithm) but has a different element type (COH3D8). The total number of elements here

is enhanced, because of the tie constraint between specimen and patch. Total number of elements is 5040 whereas number of nodes is 10584. As said in par. 4.5.4, adhesive mesh must be more fine respect to the tied parts, because of the different behaviour of the materials.

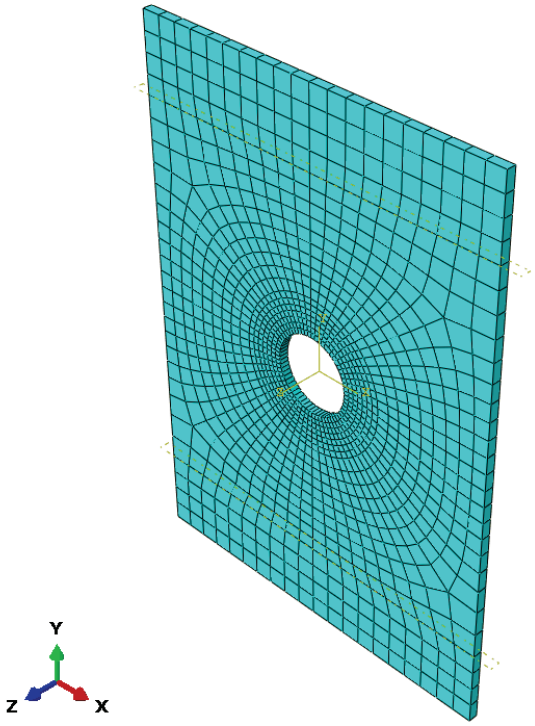

Fig. 7.5: Detail of the mesh of the specimen without patch.

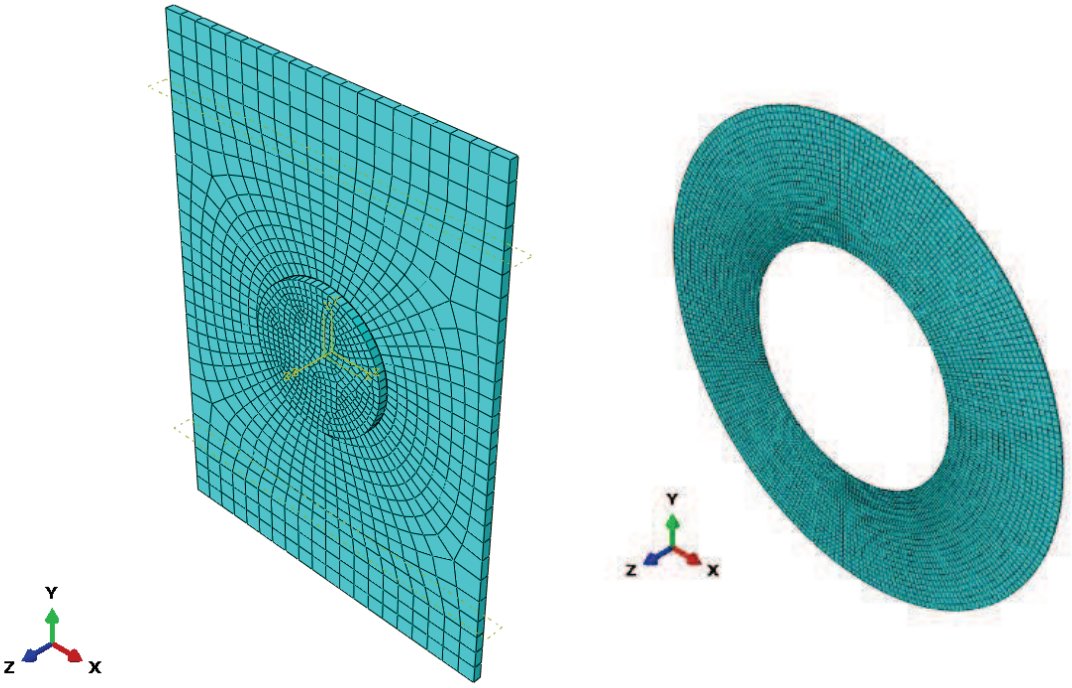

Fig. 7.6: Detail of the mesh of the specimen assembly on the left side, and of the adhesive layer on the right side.

Next figure 7.7 shows the application of the boundary conditions and loads. The model is encastred downside, i.e. U1=U2=U3=UR1=UR2=UR3=0. Upside, the displacement is fixed on 2 mm.

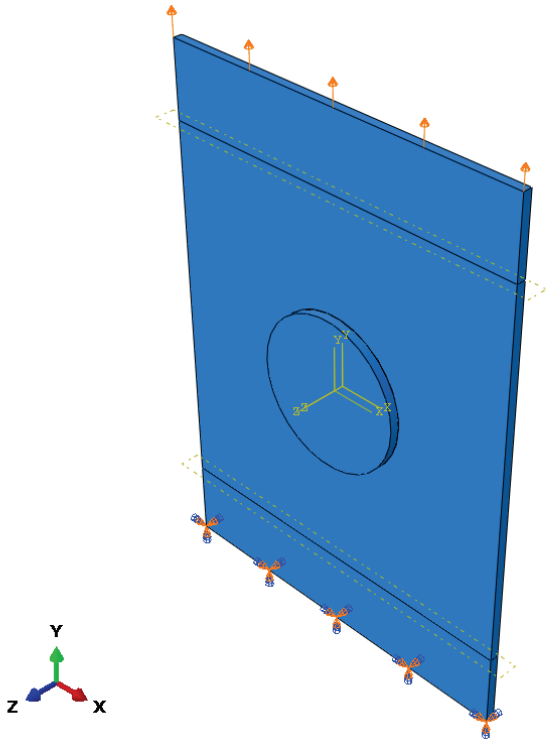

Fig. 7.7: Boundary conditions and loads.

7.4.2 Primary results

An elastic stress analysis in the adhesive layer was performed for the repair evaluated, to fit experimental P-δ curves (Fig. 7.3). Figure 7.8 presents a comparison between the experimental and numerical P-δ curves for the L_o = 5 mm SS repairs made by [Campilho et al. 2009], whereas fig. 7.9 shows results obtained in this work.

As we can see, while the paper result overestimates experimental value (Numerical grey line in fig. 7.8), in fig. 7.9 a better fit is obtained (Numerical red line in fig. 7.9) with the simulation, maybe due to a better tuning of cohesive parameters, i.e., increment step and viscosity of cohesive elements. Note that the viscosity of cohesive elements has not the same meaning as the aerodynamic viscosity, but stand for a numerical viscosity, used to release the numerical tie constraint of the different parts of the model during the simulations.

The same model could be used to simulate other geometries used by authors, with different overlaps and different radius patch but, as written before, this is not the aim of this thesis.

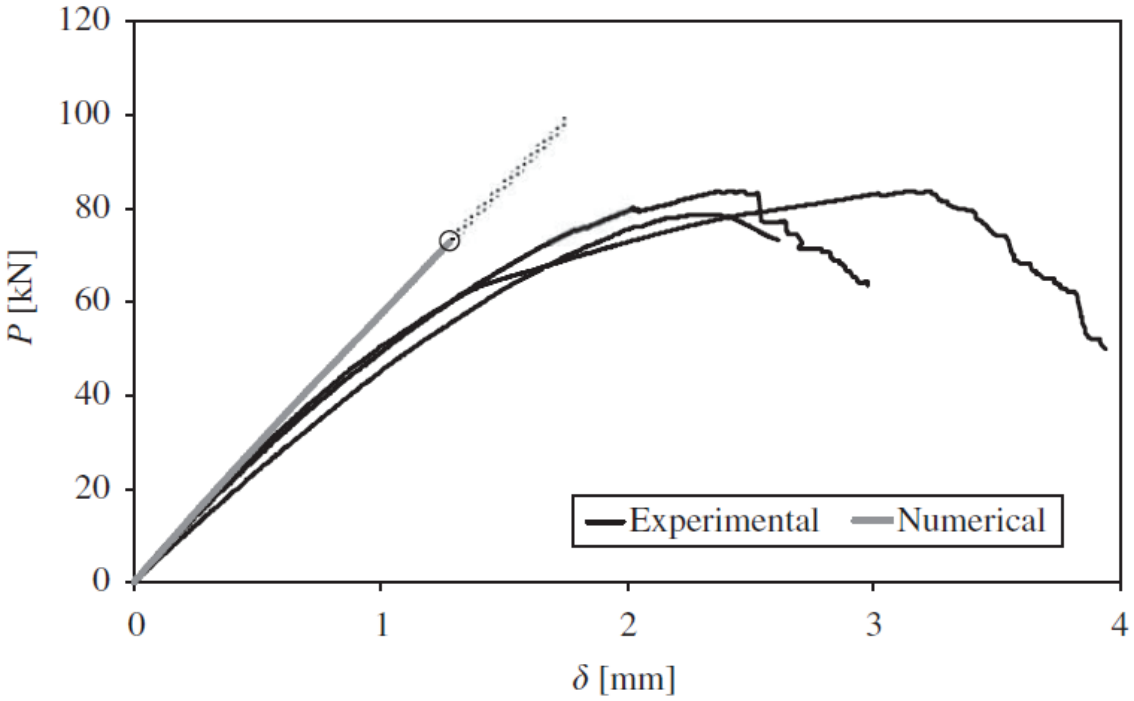

Fig. 7.8: Experimental and numerical P-δ curves comparison for the L_o = 5 mm SS repairs [Campilho et al., 2009]

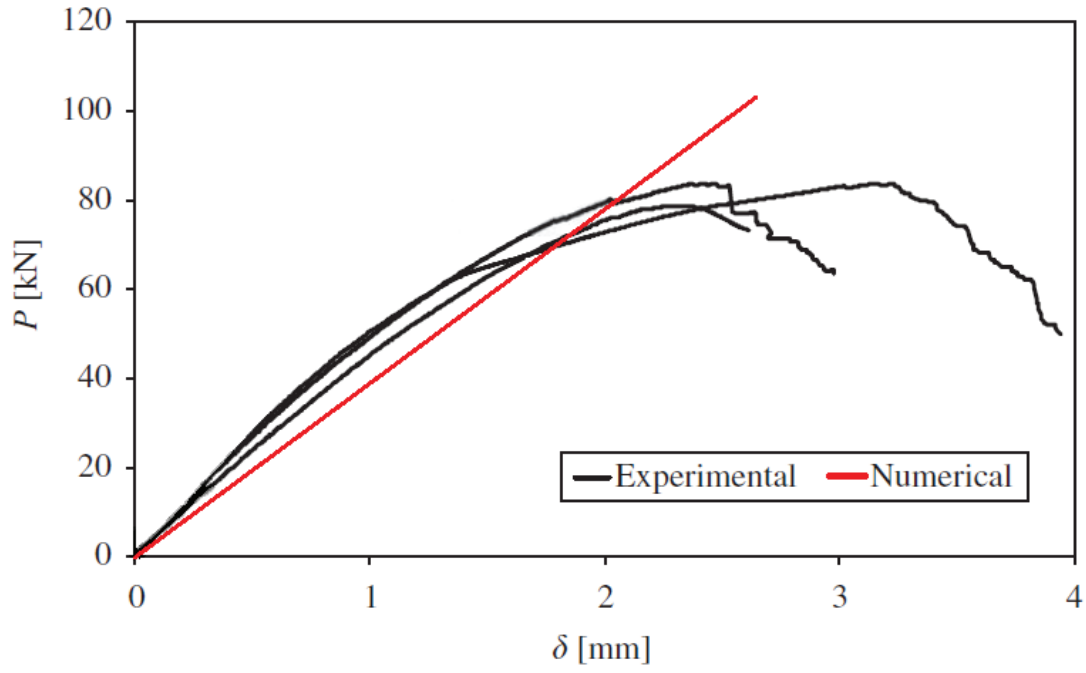

Fig. 7.9: Experimental and numerical P-δ curves comparison for the L_o = 5 mm SS repairs

7.4.3 Further model benchmarks

In addition to the last result of paragraph 7.4.2, the model was tested to have more data comparison. The next two figures 7.10 and 7.11 show graphs of applied load P [kN] vs displacement d [mm] respectively of the model with no hole and with hole but no patch. As we can see, the data are in agreement with the previous results, i.e. without hole, the model has the maximum strength; without bonded patch, the results are similar to the data extracted from Campilho's article (186,90 kN). In fact, the maximum applied load after a 2 mm displacement in Abaqus model is 99,102 kN, whereas in the model without patch we have 88,96 kN. That is, the model behaviour is what we expected. Another analysis was made to predict the crack initiation and growth of the model with no patch, using XFEM analysis possibility of Abaqus code, in agree with experimental works (Fig. 7.8. 7.9), but this is out of the aim of this work.

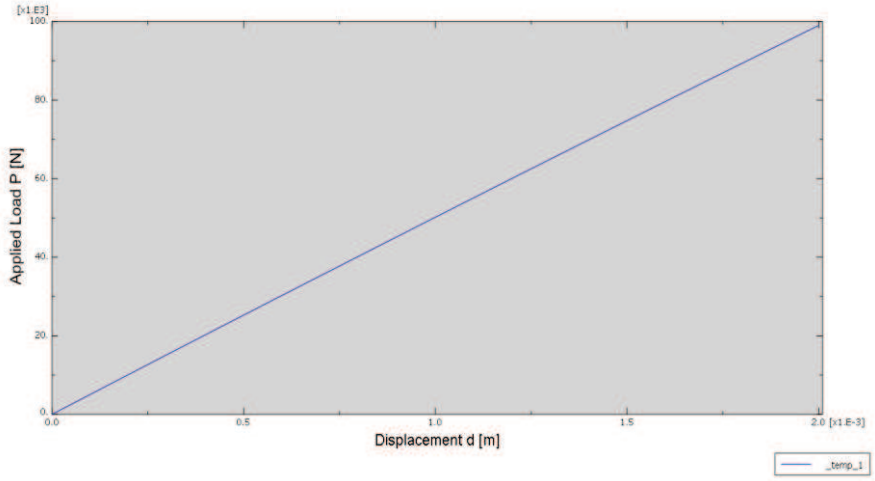

Fig. 7.10: Numerical P-δ curve of the model without hole.

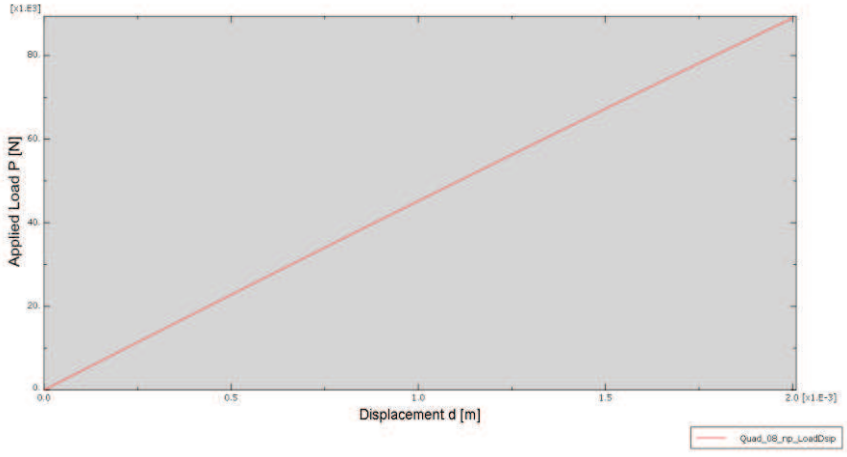

Fig. 7.11: Numerical P-δ curve of the model with hole without patch

7.5 Simulation of a weak bond

7.5.1 Why investigate on weak bond?

In all the simulations made so far, the working conditions were always ideal, because of the implementation of parameters, i.e., Abaqus, as other stress simulation codes, does not have any tricks to simulate the real environment like contamination of interfaces, environmental conditions during the bonding process and the surface treatments applied to the composite adherents. Furthermore, human operators make several mistakes like non-constant thickness of the adhesive, non-voluntary flaws, and others. In this paragraph two analysis were made, the first in order to calculate the correlation between thickness and applied load, i.e. to know the "thickness sensibility"; the second one is made to correlate flaws within the adhesive layer with the applied load. As we see later in this paragraph, flaws are simulated by different lacks of adhesive in specific directions, and the correlations are between the directions and the max applied load after a displacement of 2 mm, before the beginning of cracking, and the progressive lack of adhesive material.

7.5.2 Thickness sensibility

To overcome the thickness mistake of an operator, the repair process should be automatized. As reported in the introduction, state-of-the-art for a fully industrialized bonded repair technology (for primary structures) was only at TRL (Technology Readiness Level) stage 2. In fact, nowadays, no MRO (Maintenance, Repair & Overhaul) has its own automatized repair process for a bonded repair, and only human operators can do this kind of repair. Depending on the experience and knowledge of the maintainer, the bonded repair could differ from operator to operator, especially in the adhesive thickness between the patch and the damaged part.

The first analysis made here is to find a correlation between the adhesive thickness and the applied load of a specimen subjected to a tensile load. Model parameters, geometry, boundary conditions and loads (figs. 7.2, 7.4, 7.5, 7.6 and 7.7) are the same of paragraph 7.4.1, as well as adhesive and composite plate parameters (Tab. 7.1 and 7.2). The only variable parameter is, obviously, t_A, the thickness of the adhesive. In the different simulations, thickness varies from t_A = 0,05 mm to t_A =0,4 mm. Tab. 7.4 shows how the applied load changes varying the thickness, while fig. 7.12 represents the graph obtained with an Excel file, with a 4^{th} order polynomial trendline. As we can note from the graph, the best value for a good adhesive thickness is around 0,05 – 0,1 mm, as recommended in [Araldite® 2015 datasheet].

QUAD_8R	
t_A (mm)	P [kN]
0,05	89,1411
0,1	89,1412
0,15	89,1414
0,2	89,1415
0,25	89,1404
0,3	89,1394
0,35	89,1389
0,4	89,1387

Tab. 7.4: Adhesive thickness values vs applied load

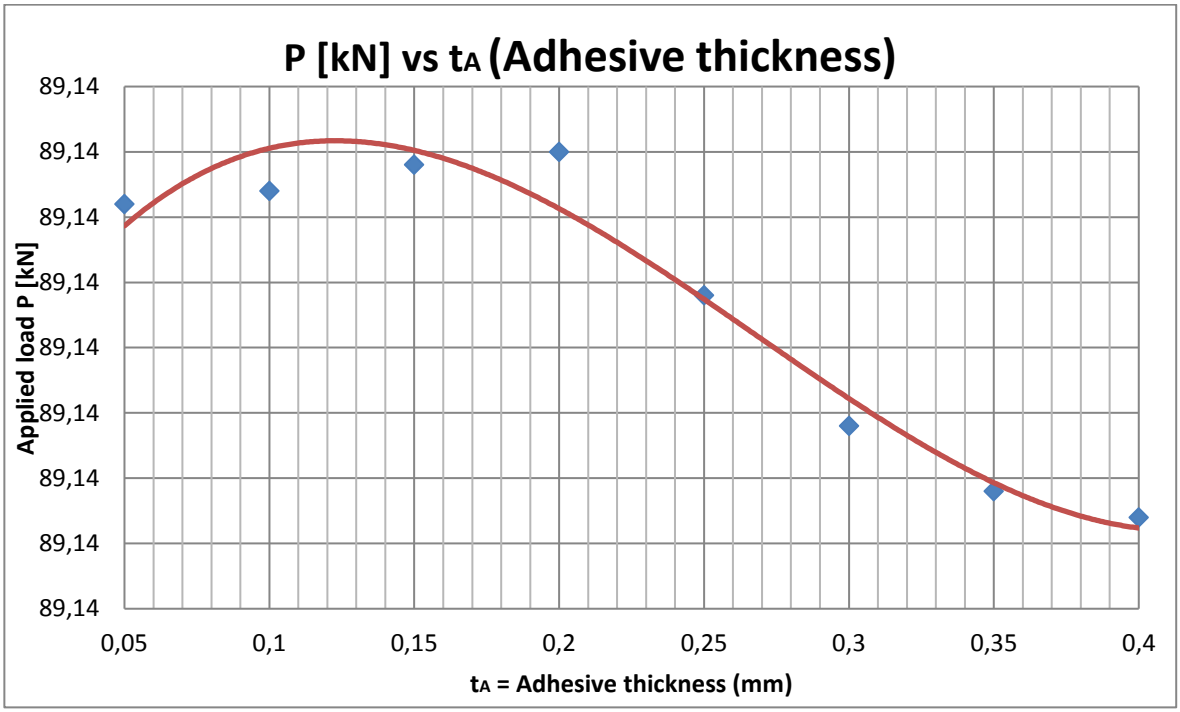

Fig. 7.12: Excel graph of adhesive thickness vs applied load

From the graph analysis, we can also deduce that, nevertheless adhesive thickness varies from 0,05 to 0,4 mm, applied load varies only from 89,1411 to 89,1387 (-1,0 %). That is, a mistake on adhesive thickness does not lead to great variations in the applied load.

7.5.3 Flaws insertion

Next step is to insert, in some manner, flaws in adhesive layer. As written before, it is well-nigh impossible to set a perfect adhesive layer between composite elements, without including some imperceptible gaps that could weaken the repair. To simulate these gaps, the model takes into account some cuts, in different directions, as described below. Cuts

simulate the lack of adhesive layer, and weaken the bonded repair. All parameters are the same of par. 7.4.1.

7.5.3.1 Asymmetric horizontal cut

Fig. 7.13 shows what we mean for asymmetric horizontal cut, gap distance varies from 1 mm to 5 mm. Table 7.5 summarizes applied loads corresponding to the different gaps, while fig. 7.14 shows the relative curve.

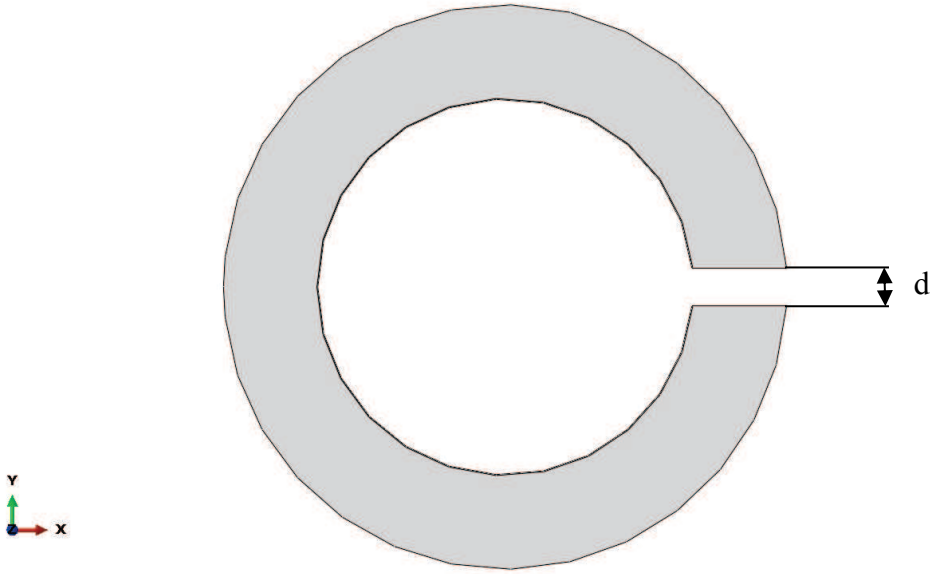

Fig. 7.13: Asymmetric horizontal cut.

QUAD_9R	
d (mm)	AHC
1	89,1341
2	89,1225
3	89,1121
4	89,1039
5	89,0931

Tab. 7.5: Gap distance d (mm) vs applied load (kN) in asymmetric horizontal cut.

As we can deduct from fig. 7.14, nevertheless adhesive gap distance of the asymmetric horizontal cut varies from 1 to 5 mm, applied load varies only from 89,0876 to 88,9598 (-0,14%), practically the adhesive lack in an asymmetric horizontal cut manner doesn't affect the bonding stiffness.

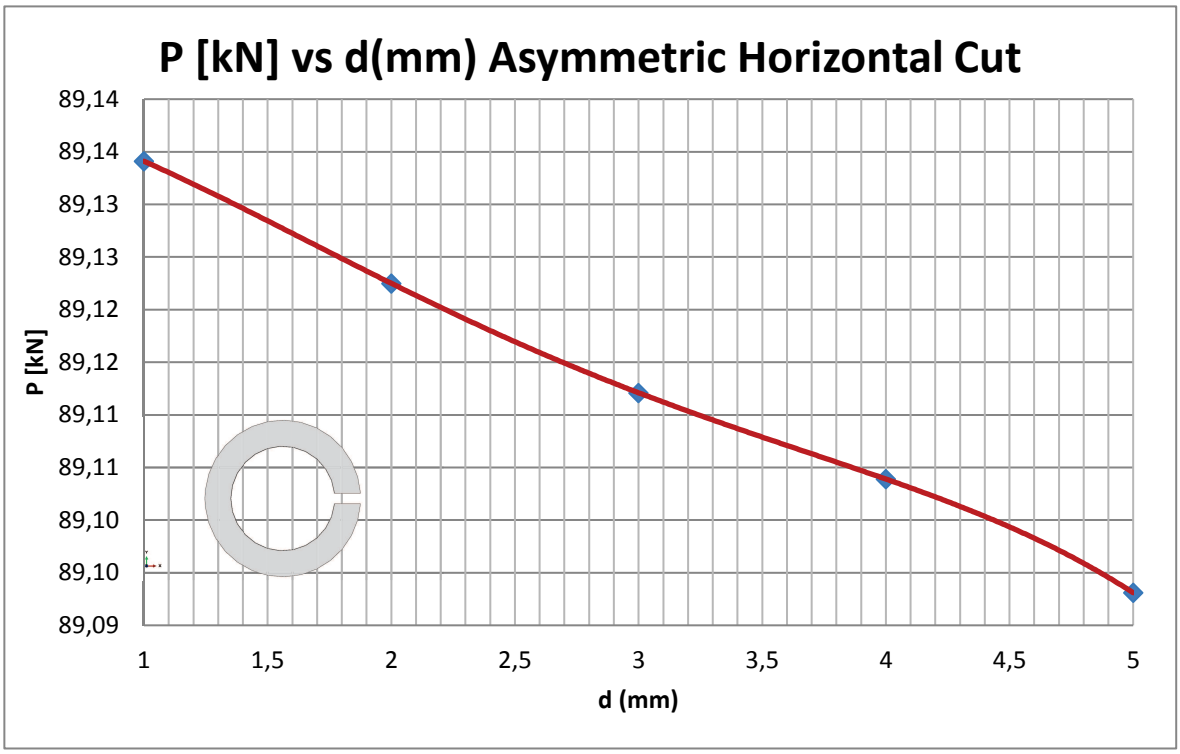

Fig. 7.14: Excel graph of gap distance of asymmetric horizontal cut vs applied load.

7.5.3.2 Symmetric horizontal cut

Fig. 7.15 shows a symmetric horizontal cut, gap distance varies from 1 mm to 5 mm. Table 7.6 summarizes applied loads corresponding to the different gaps, while fig. 7.16 shows the relative curve.

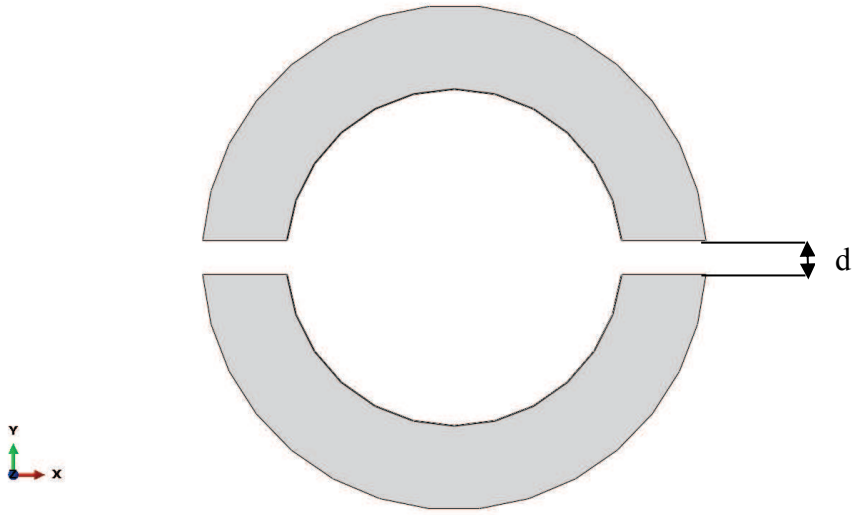

Fig. 7.15: Symmetric Horizontal Cut.

QUAD_10R	
d (mm)	SHC
1	89,1314
2	89,1139
3	89,0965
4	89,0930
5	89,0852

Tab. 7.6: Gap distance d (mm) vs applied load (kN) in symmetric horizontal cut.

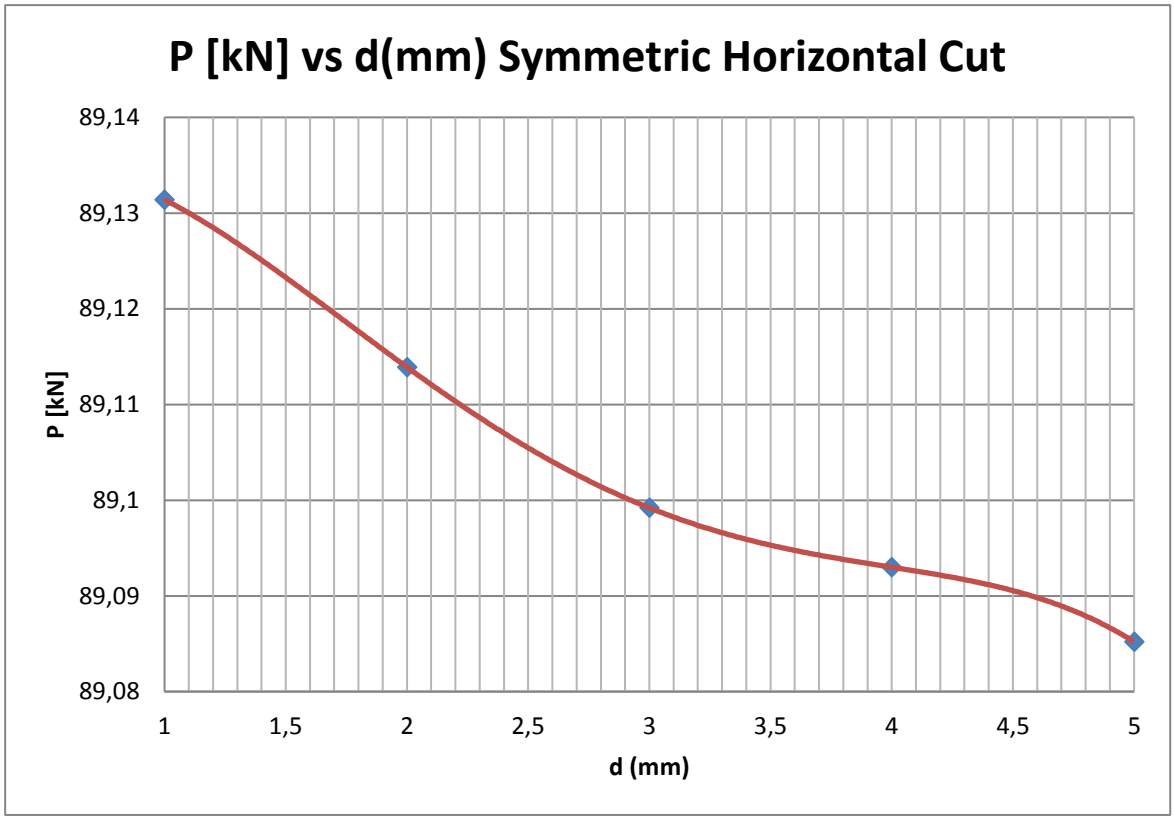

Fig. 7.16: Excel graph of gap distance of symmetric horizontal cut vs applied load.

Also in this case, as we can see from fig. 7.16, nevertheless adhesive gap distance of the symmetric horizontal cut varies from 1 to 5 mm, applied load varies only from 89,1314 to 89,0852 (-0,05%). Practically the adhesive lack in a symmetric horizontal cut manner does not affect the bonding stiffness.

7.5.3.3 Asymmetric vertical cut

Asymmetric vertical cut is visible in fig. 7.17. Gap distance of the cut varies from 1 mm to 5 mm. Table 7.7 summarizes applied loads corresponding to the different gaps, while fig. 7.18 shows the relative curve.

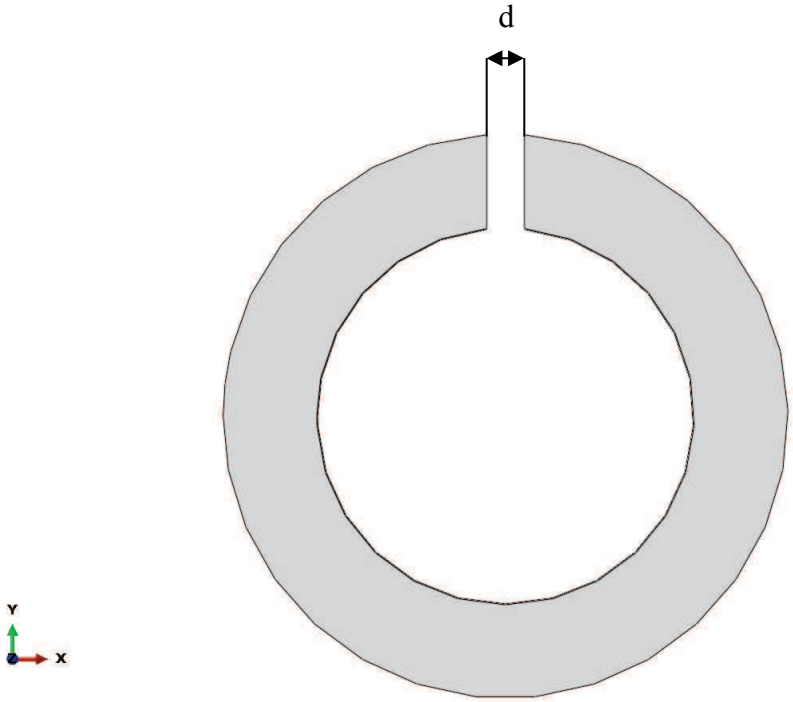

Fig. 7.17: Asymmetric vertical cut.

QUAD_11R	
d (mm)	AVC
1	89.1438
2	89,1432
3	89,1428
4	89,1428
5	89,1428

Tab. 7.7: Gap distance d (mm) vs applied load (kN) in asymmetrical vertical cut.

Now, even though applied loads have a little bigger range, the percentage variation in applied loads relative to the same gap distance increment of previous simulations is only -1,66%. Even in this case, we can assert that the stiffness bonding is not affected by the adhesive lack. Note that applied load values are bigger than in Horizontal cuts, as expected, because of stress concentrations.

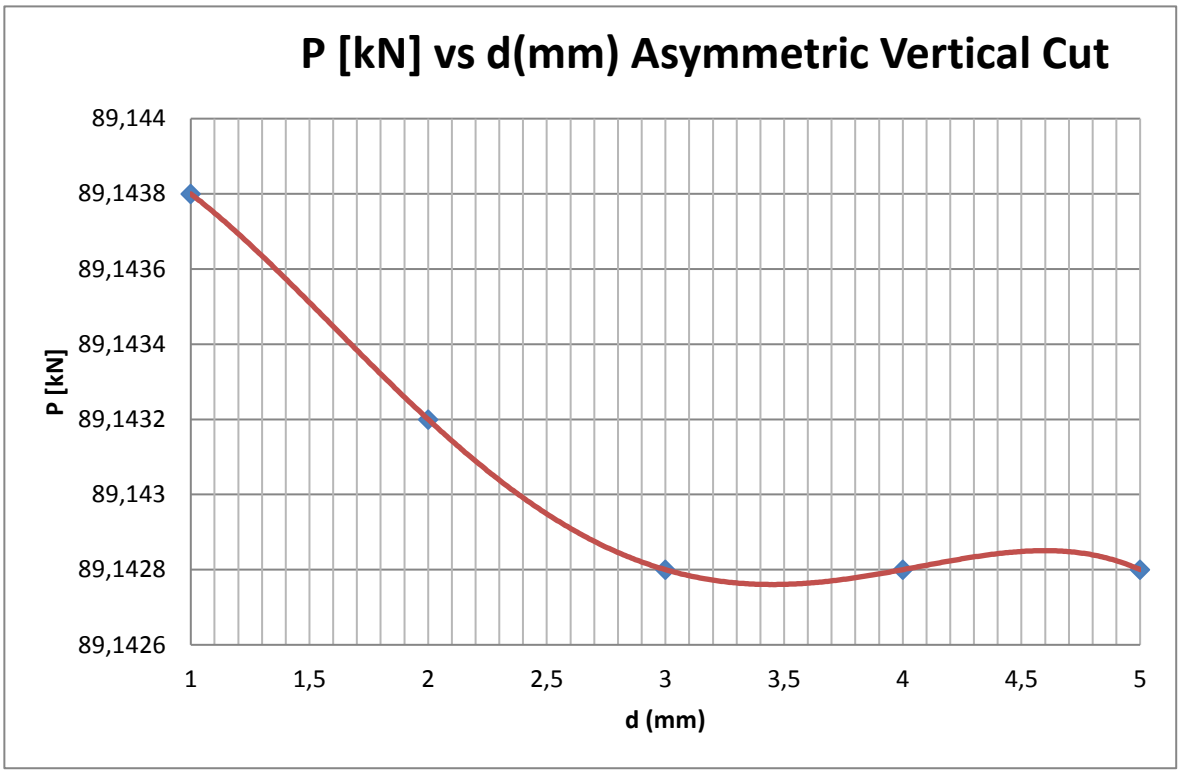

Fig. 7.18: Excel graph of gap distance of asymmetric vertical cut vs applied load.

7.5.3.4 Symmetric vertical cut

As for symmetric horizontal cut, fig. 7.19 shows the symmetric vertical cut with varying gap distance. Table 7.8 summarizes applied loads corresponding to the different gaps, while fig. 7.20 shows the relative curve. As in previous cases, we can say that applied load variation has no significant excursion (-2,72%).

QUAD_12R	
d (mm)	SVC
1	89,1435
2	89,1434
3	89,1433
4	89,1432
5	89,1431

Tab. 7.8: Gap distance d (mm) vs applied load (kN) in symmetric vertical cut.

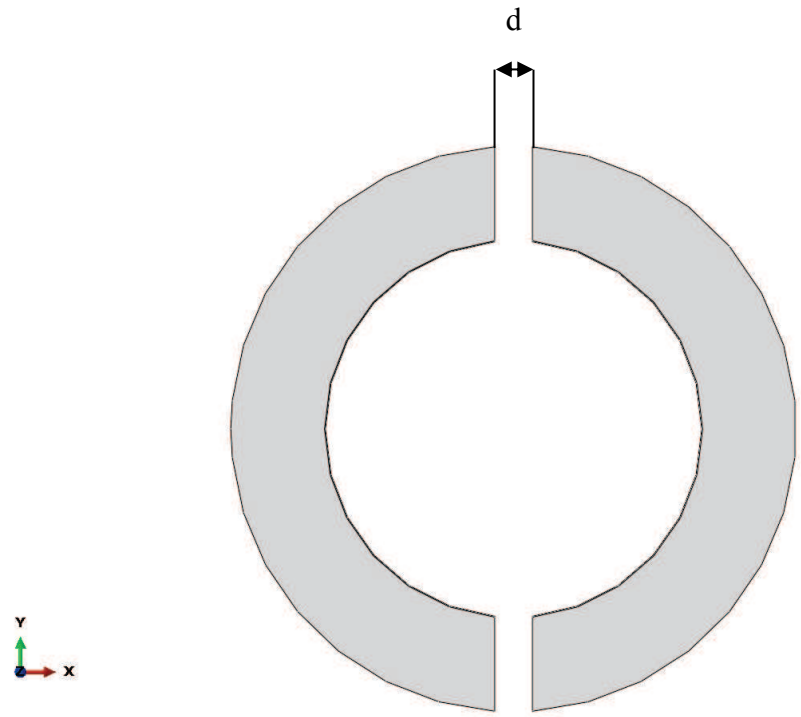

Fig. 7.19: Symmetric vertical cut.

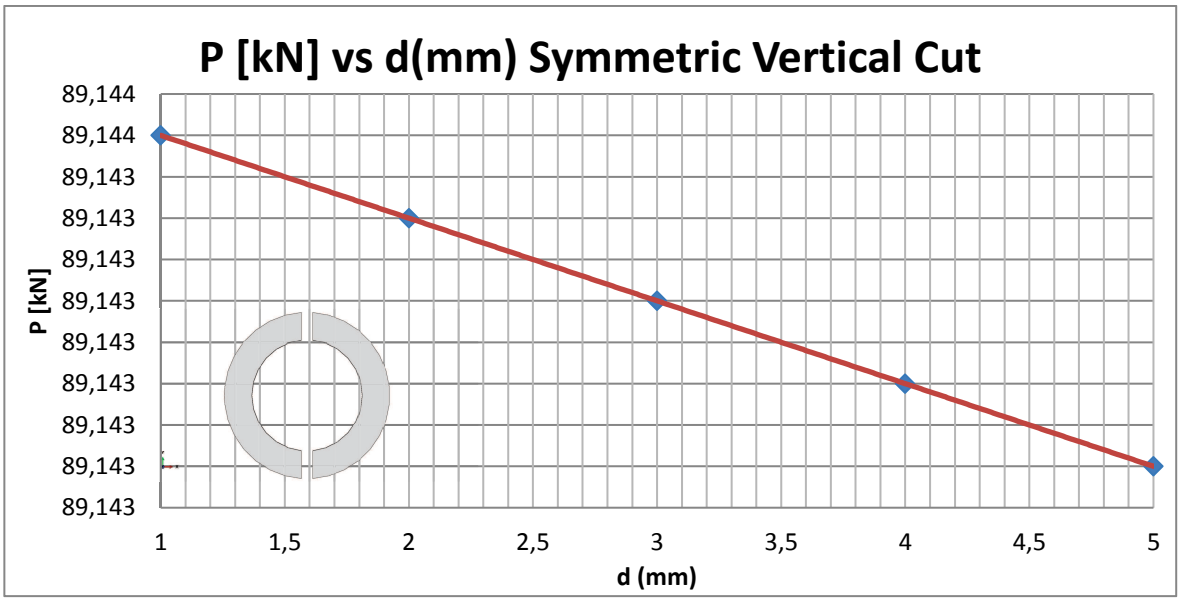

Fig. 7.20: Excel graph of gap distance of symmetric vertical cut vs applied load

7.5.3.5 Asymmetric right cut on 45°

Analysis continues with cut on +45° to respect y-axis. Fig. 7.21 shows the geometry adopted for this simulation. Details below in Tab. 7.9 and fig. 7.22. Even in these cases, applied loads have no significant variations.

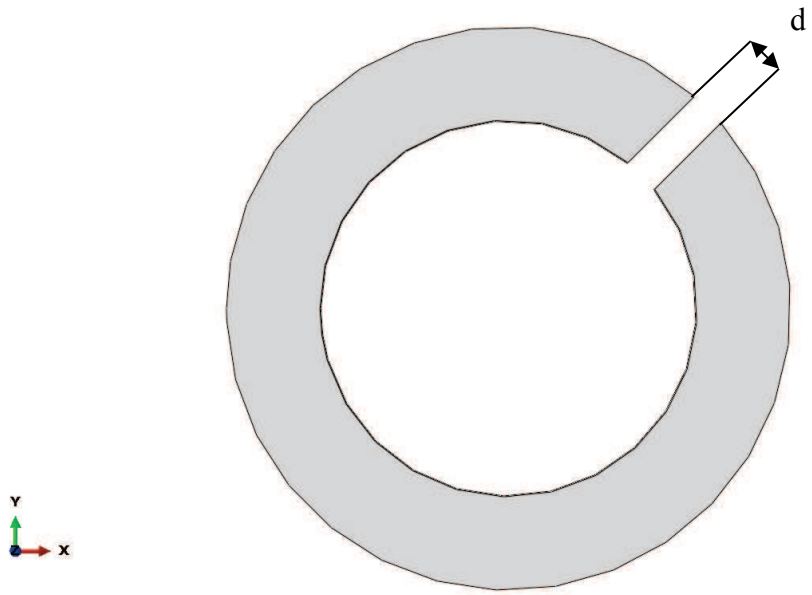

Fig. 7.21: +45° asymmetric cut.

QUAD_13R	
d (mm)	45°ASC
1	89,1397
2	89,1364
3	89,1339
4	89,1308
5	89,1265

Tab. 7.9: Gap distance d (mm) vs applied load (kN) in 45° asymmetric cut.

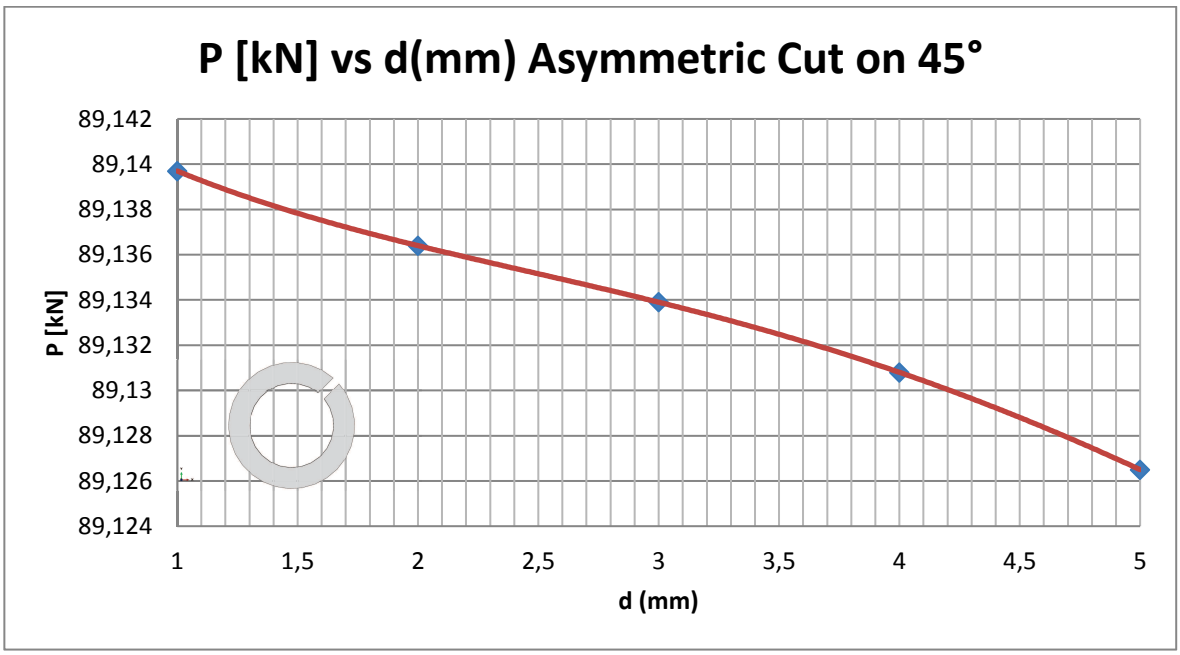

Fig. 7.22: Excel graph of gap distance of 45° asymmetric cut vs applied load.

7.5.3.6 Symmetric cut on 45°

The next simulation recovers the previous cases done with horizontal and vertical cuts. Then, cuts are symmetrically placed on +45° and +225°, as we can see in fig. 7.23. Tab. 7.10 and fig. 7.24 reports usual information.

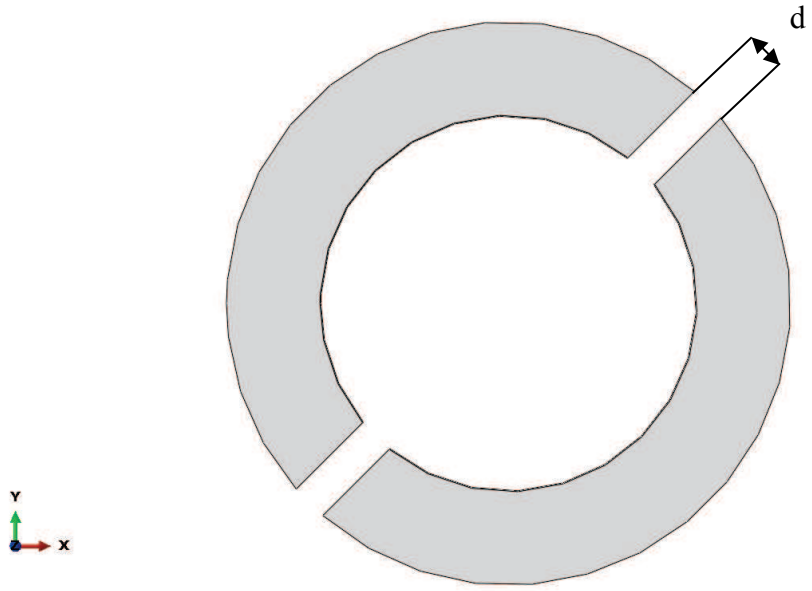

Fig. 7.23: +45° symmetric cut.

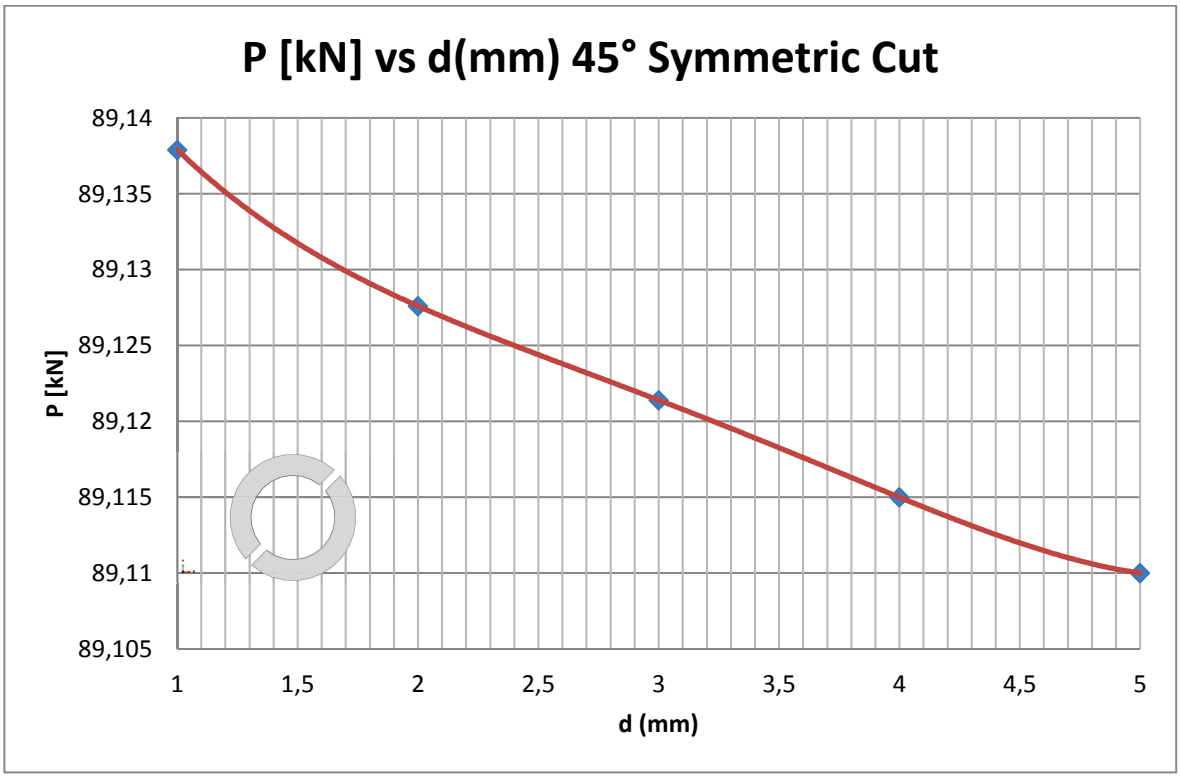

Fig. 7.24: Excel graph of gap distance vs applied load of 45° symmetric cut.

QUAD_14R	
d (mm)	45°SC
1	89,1379
2	89,1276
3	89,1214
4	89,1150
5	89,1100

Tab. 7.10: Gap distance d (mm) vs applied load (kN) in 45° symmetric cut.

7.5.3.7 Symmetric cut on + 45° and – 45°

For completeness, analysis takes into account other two cases, as described in figs. 7.25 and 7.27. Tab. 7.11 and 7.12 report results of ±45° asymmetric cuts and ±45° symmetric cuts respectively. Relative graphs are drawn in figs. 7.26 and 7.28.

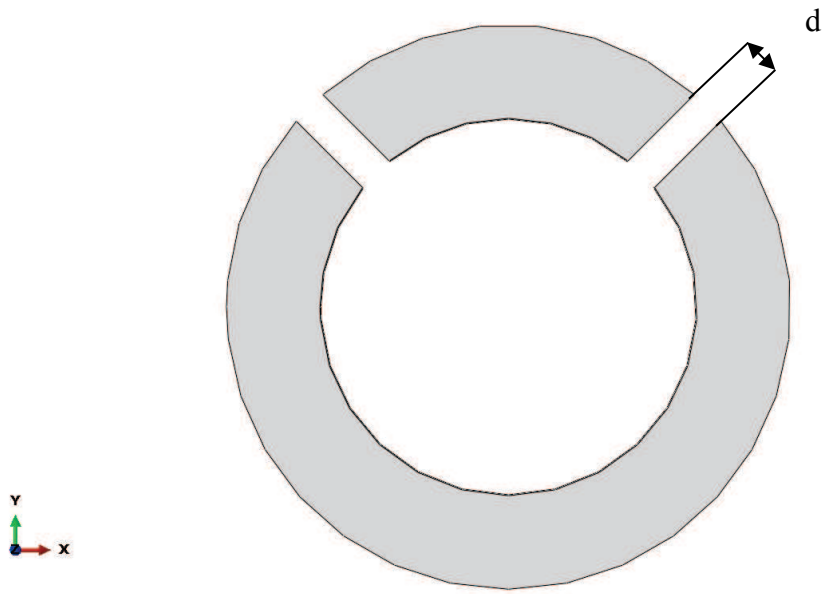

Fig. 7.25: ±45° asymmetric cuts.

QUAD_15R	
d (mm)	±45°ASC
1	89,1309
2	89,1263
3	89,1230
4	89,1189
5	89,1151

Tab. 7.11: ±45° asymmetric cuts.

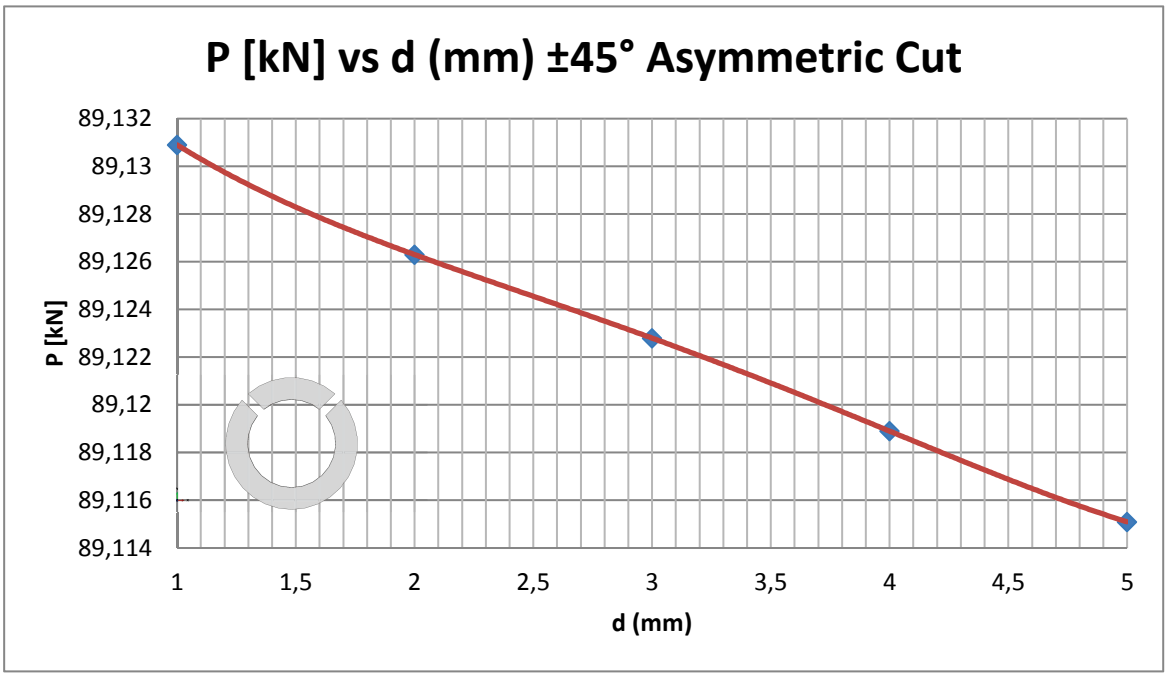

Fig. 7.26: Excel graph of applied load vs gap distance of ±45° asymmetric cuts.

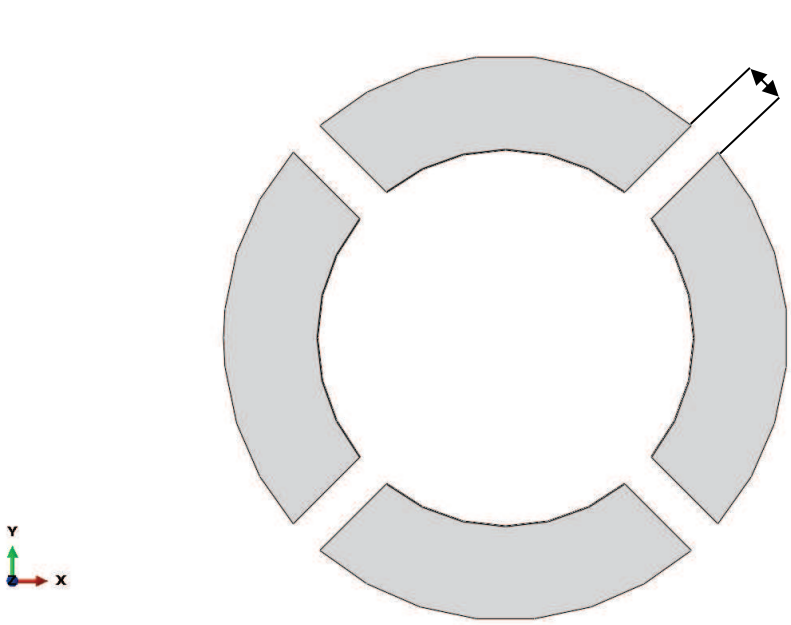

Fig. 7.27: ±45° symmetric cuts.

QUAD_16R	
d (mm)	±45°SC
1	89,1237
2	89,1049
3	89,0900
4	89,0764
5	89,0633

Tab. 7.12: ±45° symmetric cuts.

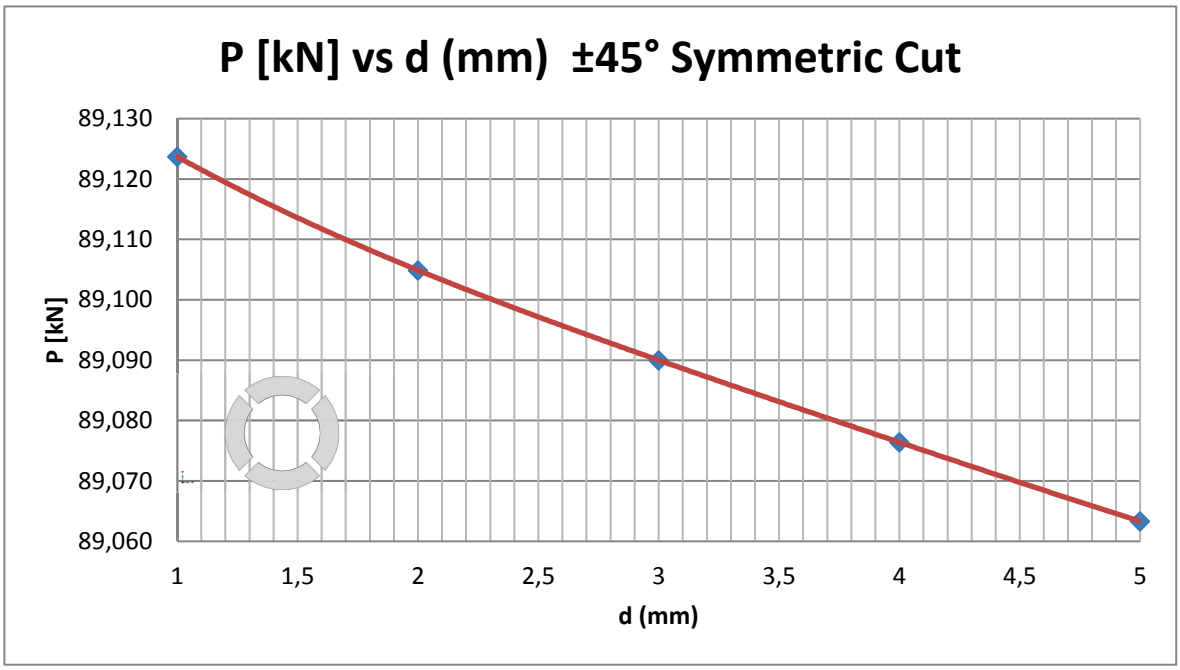

Fig. 7.28: Excel graph of applied load vs gap distance of ±45° symmetric cuts.

To have an overview of all the simulations, a diagram that reports all the curves is shown in fig. 7.29. In this graph, we have two lecture keys:

1. In an horizontal manner, from left to right, all the values decrease, that is, bigger the lack of adhesive layer, smaller the applied load values;

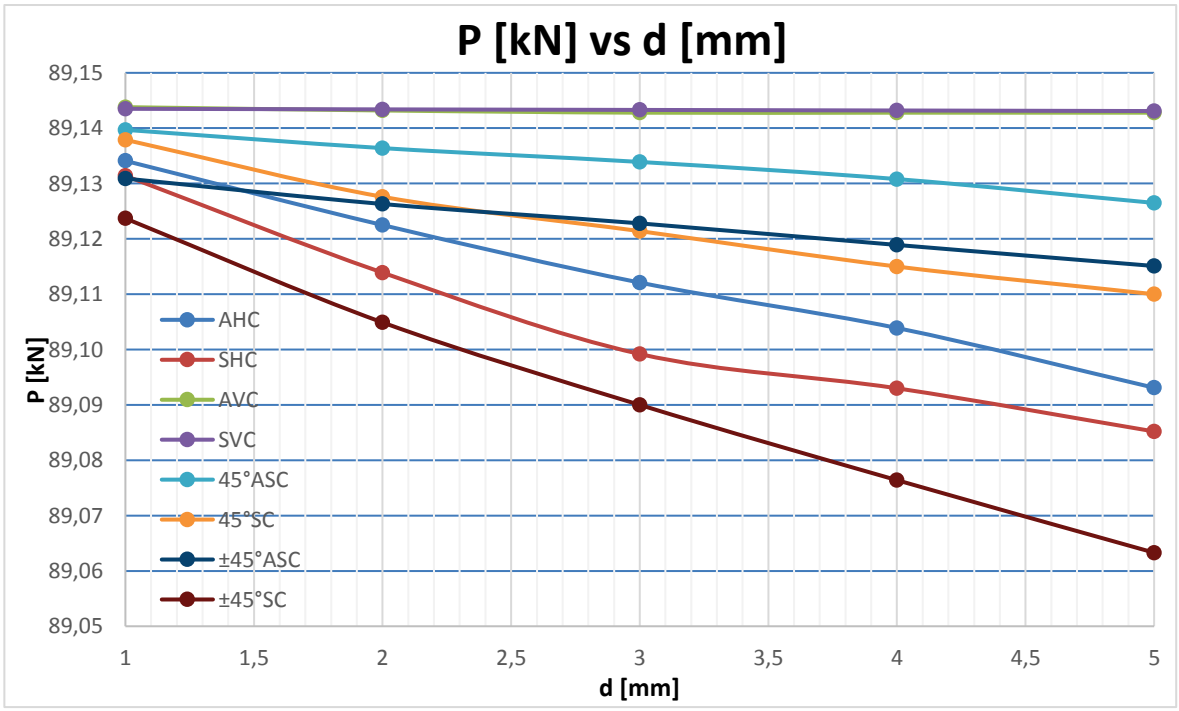

Fig. 7.29: Excel graph of all the made tests.

2. In a vertical manner, from up to down, the best case done by a symmetric vertical cuts, the worst case by $\pm 45°$ symmetric cuts.

However, the main information we can deduce is that the variations in applied loads, in all analysed cases, are very small, from about 89,145 kN to 89,06 kN. Obviously, compared with the specimen without hole, values of the SS bond repair are significantly smaller (approximately, - 10%), but compared with a specimen with an hole and without patch, we have a good increment in residual strength of bonded repair (about +2,55%).

CHAP. 8: Concluding Remarks and Future Applications

The aim of this thesis has been to investigate the behaviour and the mechanical properties of bonded repairs of composite material. Particularly, attention was focused on weak bond. A weak bond is defined as a bond that provides intimate contact without providing adhesive strength.

Several steps were made to understand how to model and implement a repair of a primary aircraft structure. First, we searched for the material used in the industries. Materials used to build primary aircraft structures is a prepreg manufactured by Hexcel®, the Texipreg HS 160 RM (SEAL®, Legnano, ITALY). For adhesive material, investigations from literature lead to a structural adhesive, Araldite® 2015 (Huntsmann, Basel, SWITZERLAND).

After a deep analysis on the Finite Element Method and on mathematical and physical concepts beyond the Composite Fiber Reinforced Polymer, some studies and benchmarking were implemented on the Abaqus® code, the software used for our research, which permits application of Cohesive Zone Model, a model based on energetic criteria.

Different analysis were carried out to validate use and comprehension of the code, from simple traction and bending laminate tests to some applications like the Double Cantilever Beam and the End Notched Flexure, used later to define cohesive parameters.

From literature, we found a paper written by [Campilho et al. 2009] where an experimental and numerical study of the tensile behaviour of three-dimensional carbon-epoxy adhesively bonded strap repairs is presented. In this study, the failure mode, elastic stiffness and strength were evaluated for different overlap lengths and patch thicknesses experimentally. The numerical simulations, performed in Abaqus®, allowed obtaining the elastic stiffness and the patch debonding load, used to understand the repairs behaviour. The adhesive layer was simulated with cohesive elements including a mixed-mode cohesive damage model with trapezoidal traction-separation laws in pure modes I and II, to account for the ductile behaviour of the adhesive used. These laws were determined by an inverse method, which consists on the estimation of the cohesive parameters with a fitting procedure of the experimental and numerical load–displacement curves of the respective fracture characterization test. The pure mode III cohesive law was equalled to the pure mode II one. This numerical methodology was found adequate to reproduce the experimentally observed behaviour of these repairs.

The model of bonded single strap repair of Campilho's article was first implemented with the same cohesive damage law, to reproduce and benchmark the results obtained experimentally.

Then the investigation continues to assess the thickness sensibility (fig. 7.12), which agree with the adhesive data sheet advice. At last, the research has tested the weak bond, simulating the weakness of the adhesive with an innovative method: some cuts were made in different directions, through the material to obtain correlation diagrams between the tensile applied load and the displacement of the model.

In the fig. 8.1, the first correlation curve was found between the applied load relative to the max displacement of the specimen before cracking initiation and the thickness of the adhesive. For every thickness value from t_A=0,005 mm with increments of 0,005 mm to 0,4 mm, the corresponding applied load values were reported. Data sheet of the manufacturer recommends a thickness from 0,05 to 0,1 mm to have a better shear behaviour. In the diagram the max values were found in a range of 0,2 mm, exactly from 0,05 to 0,2 mm, in agree with the manufacturer advice. However, we can extract another information from the diagram. In fact, even though adhesive thickness varies from 0,05 to 0,4 mm, applied load varies only from 89,1411 to 89,1387 kN. In other words, different adhesive thicknesses do not lead to great variations in the applied load.

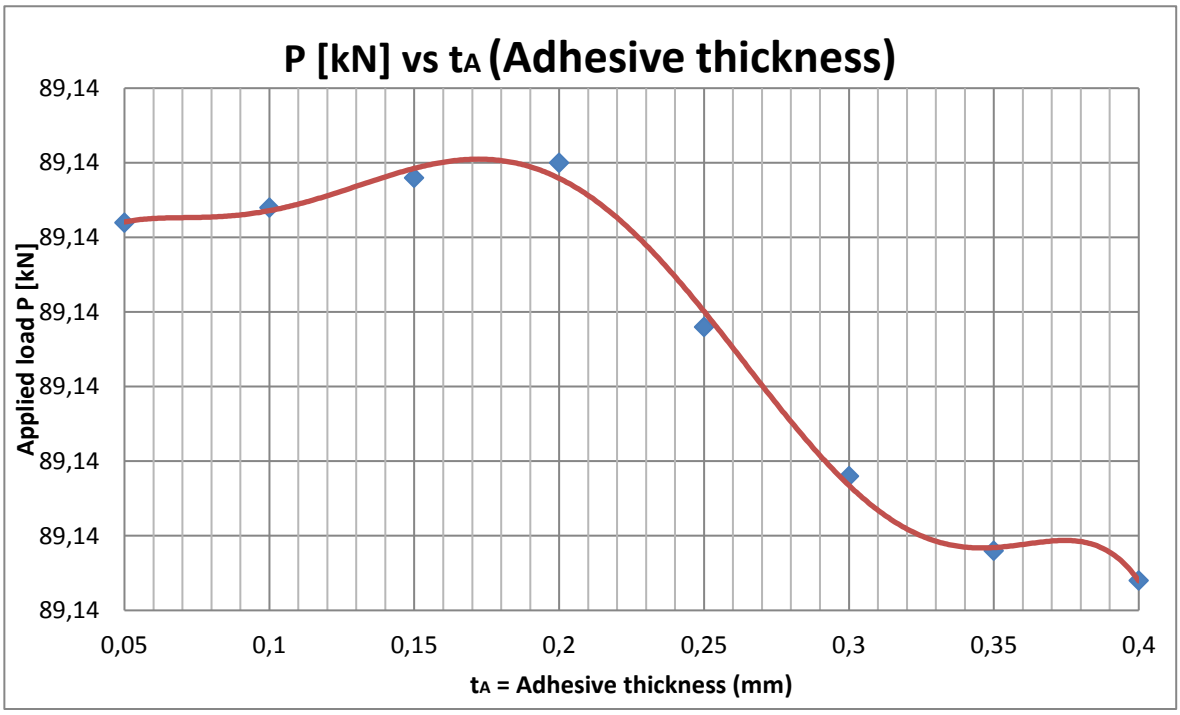

Fig. 8.1: Excel graph of adhesive thickness vs applied load

As written before, further investigations are made to understand the behaviour of a weak bond. A weak bond is a bonded repair where the energy required to disbond the repair is

substantially less than the energy required for a strong bond. To simulate a weak bond, different lack of adhesive material, in different directions, were investigated.

In par. 7.5.3, adhesive material was made weak with varying linear cuts, throughout some directions. The direction cuts are:

- Asymmetric Horizontal Cut (AHC) (fig. 7.13 and 7.14);
- Symmetric Horizontal Cut (SHC) (figs 7.15 and 7.16);
- Asymmetric Vertical Cut (AVC) (figs 7.17 and 7.18);
- Symmetric Vertical Cut (SVC) (figs 7.19 and 7.20);
- 45° Asymmetric Cut (45°ASC) (figs 7.21 and 7.22);
- 45° Symmetric Cut (45°SC) (figs 7.23 and 7.24);
- $\pm$45°Asymmetric Cuts ($\pm$45°ASC) (figs 7.25 and 7.27);
- $\pm$45° Symmetric Cuts ($\pm$45°SC) (figs 7.27 and 7.28).

In every diagram, the correlation was found between the applied load and the progressive gap of the cut at the crack initiation. The gaps vary from d = 1 mm to 5 mm.
As expected, more the gap, less the applied load found. Figure 8.2 reports all the simulations made. Note that Asymmetric Vertical Cut (AVC) and Symmetric Vertical Cut (SVC) give the best performance whereas Symmetric Horizontal Cut (SHC) and $\pm$45° Symmetric Cuts ($\pm$45°SC) results are the worst cases.
As in the thickness case, we can extract another information from the diagram. Even if the gap distance varies from 1 to 5 mm, all the curves underline that applied loads fluctuate between -0.06% and -2.72%. That is, the applied load variation is not so big as we can expect from a weak bonded single strap repair.
Furthermore, all the simulation results, compared to the specimen without hole and with hole but without patch, are in agree. That is, values of the Single strap bond repair vs specimen without hole are significantly smaller, approximately, - 10%. Moreover, compared with a specimen with an hole and without patch, we have a good increment in residual strength of bonded repair (about +2,55%).

The model presented in this thesis lends to a multitude of future applications. Here are some next investigation possibilities:

- **Validation of the model:** First, the model presented in this thesis, even if based on experimental data found in literature, has to be validated with specific tests that reproduce the different correlations obtained in this work. In fact, the cutting method used here was not yet investigated with experimental tests, as well as the thickness sensivity;

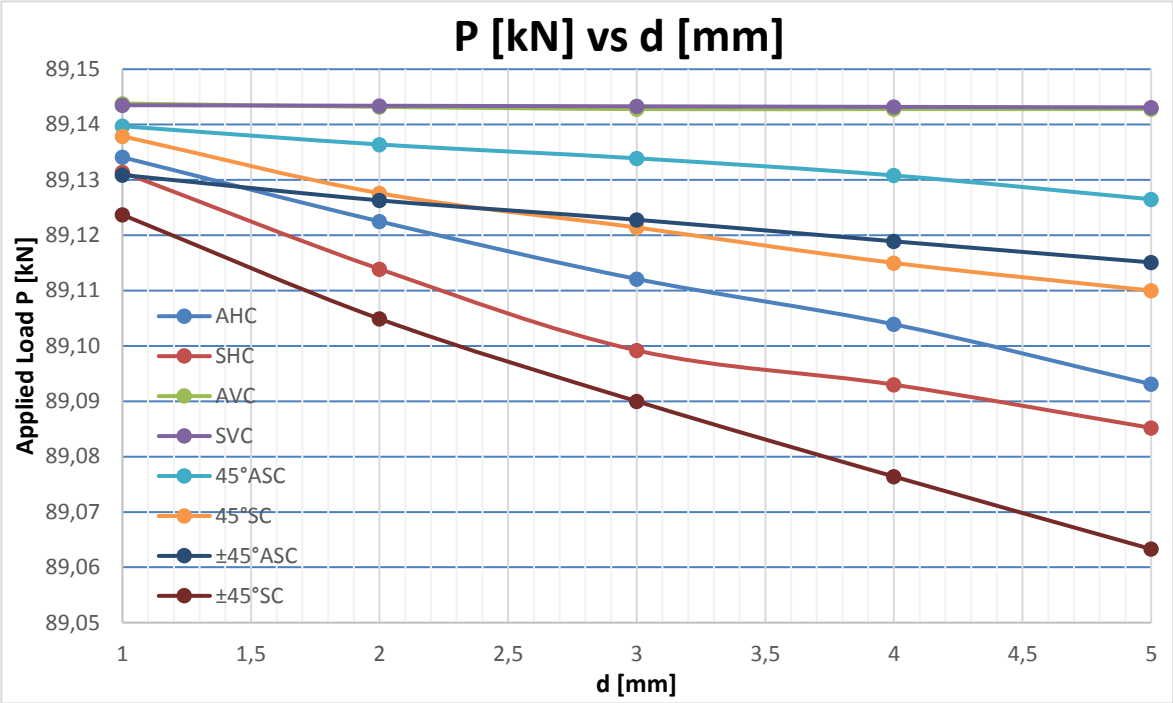

Fig. 8.2: Excel graph with all analysed cases.

- **Simulation of the surface preparation:** the adhesive used the cohesive elements. A possible technique to simulate the different grip of the surface is to pauperize the elements nodes, in order to progressively diminish the contact between the surfaces. A correlation curve can be traced to analyse the weakness of the strap bonded repair due to poor strengthen of the adhesive;
- **Environmental conditions:** the temperature room and the relative humidity are two editable parameters of Abaqus code. It is then possible to analyse the behaviour of the strap bonded repair as a function of these parameters;
- **Crack initiation and growth:** another useful Abaqus feature is the possibility to work with XFEM (Extended Finite Element Method). Abaqus permits the study of the onset and propagation of cracking in quasi-static problems using the extended finite element method. XFEM can study crack growth along an arbitrary, solution-dependent path without needing to remesh the model. XFEM is available only for three-dimensional solid, as the model of this thesis. XFEM can be used to study a crack in parts containing geometry, orphan mesh elements, or a combination of the two. It is possible to choose to study a crack that grows arbitrarily through the model or a stationary crack. Abaqus can determine the location of the crack during the analysis based on the value of the maximum principal stress or strain calculated in the crack domain;

- **Multimodal tensile stresses:** as explained throughout the thesis, the fuselage is subjected to a hoop stress. That is, another numerical analysis can be made in order to understand the multimodal tensile stresses behaviour respect to a weak bond;
- **Fatigue stress:** the model can also be used to simulate fatigue stress. In this case, a different cohesive law is necessary, and further studies are needed to understand the behaviour of fatigue stress on composite material.

Bibliography

Abaqus/CAE 6.13 Documentation, (http://129.97.46.200:2080/v6.13/)

Andersson T, Stigh U. The stress-elongation relation for an adhesive layer loaded in peel using equilibrium of energetic forces. Int J Solids Struct 2004; 41:413–34.

Araldite® 2015 datasheet, Huntsmann, Basel, SWITZERLAND

Barbero Ever J., Finite Element Analysis of Composite Materials using Abaqus™, CRC Press, 2013,

Barenblatt, G.I.: The mathematical theory of equilibrium cracks in brittle fracture. Adv. Appl. Mech. 7, 55–129 (1962)

Bazant, Z.P.: Concrete fracture models: testing and practice. Eng. Fract. Mech. 69, 165–205 - 2002

Blohowiak K. et al., Efficient Certification of Bonded Primary Structures, 2013 SAMPE

Camacho, G.T., Ortiz, M.: Computational modelling of impact damage in brittle materials. Int. J. Solids Struct. 33, 2899–2938 (1996)

Campilho RDSG, de Moura MFSF, Domingues JJMS, Morais JJL., Tensile behaviour of three-dimensional carbon-epoxy adhesively bonded single- and double-strap repairs, International Journal of Adhesion & Adhesives 29; 2009; 678–686

Campilho RDSG, de Moura MFSF, Domingues JJMS. Modelling single and double-lap repairs on composite materials. Compos Sci Technol 2005; 65: 1948–58.

Campilho RDSG, de Moura MFSF, Domingues JJMS. Using a cohesive damage model to predict the tensile behaviour of CFRP single-strap repairs. Int J Solids Struct 2008; 45:1497–512.

Cornec A. et al. / Engineering Fracture Mechanics 70 (2003) 1963–1987

Dàvila C.G., Camanho P.P., de Moura M.F., Mixed-Mode Decohesion Elements for Analyses of Progressive Delamination, 42nd AIAA/ASME/ASCE/AHS/ASC Structures, Structural Dynamics and Materials Conference Seattle, Washington, 2001

de Moura MFSF, Gonçalves JPM, Chousal JAG, Campilho RDSG. Cohesive and continuum mixed-mode damage models applied to the simulation of the mechanical behaviour of bonded joints. Int J Adhes 2008; 28:419-26.

Dugdale DS., Yielding of steel sheets containing slits, J Mech Phys Solids 1960; 8:100–4

Gibson Ronald F., Principles of composite material mechanics, 3°ed, CRC Press, 2012

Gonçalves JPM, de Moura MFSF, Magalhaes AG, de Castro PMST. Application of interface finite elements to three-dimensional progressive failure analysis of adhesive joints. Fatigue Fract Eng M 2003; 26:479–86.

Gonçalves, J.P.M., de Moura, M.F.S.F., de Castro, P.M.S.T., and Marques, A.T., "Interface Element Including Point-to-Surface Constraints for Three-Dimensional Problems with Damage Propagation," Engineering Computations, Vol. 17, No. 1, 2000, pp. 28-47.

Hillerborg A,Modeer M, Petersson PE. Analysis of crack formation and crack growth in concrete by means of fracture mechanics and finite elements. Cem Conr Res 1976;6:773–82.

Hillerborg, A., Modeér, M., Petersson, P.E.: Analysis of crack formation and crack growth in concrete by means of fracture mechanics and finite elements. Cem. Concr. Res. 6, 773–782 (1976)

Hogberg J L, Stigh U. Specimen proposals for mixed mode testing ofa dhesive layer. Eng Fract Mech 2006; 73:2541–56.

Hyer M. W., Stress Analysis of Fiber-reinforced Composite Materials, DEStech Publications, Inc, 1998

Leffler K, Alfredsson K S, Stigh U. Shear behaviour of adhesive layers. Int J Solids Struct 2007; 44:530–45.

Mi, Y., and Crisfield, M.A., "Analytical Derivation of Load/Displacement Relationships for Mixed-Mode Delamination and Comparison with Finite Element Results," Imperial College, Department of Aeronautics, London, 1996.

Mi, Y., Crisfield, M.A., Davies, G.A.O., and B., H.H., "Progressive Delamination Using Interface Elements," Journal of Composite Materials, Vol. 32, 1998, pp. 1246-1273.

Morais, A.B., Marques, A.T., and de Castro, P.T., Estudo Da Aplicação De Ensaios De Fractura Interlaminar De Modo I a Laminados Compósitos Multidireccionais, Proceedings of the 7as Jornadas De Fractura, Sociedade Portuguesa de Materiais, Portugal, 2000, pp. 90-95

Needleman A. A continuum model for void nucleation by inclusion debonding. J Appl Mech 1987; 54:25–531

Needleman, A.: An analysis of decohesion along an imperfect interface. Int. J. Fract. 42, 21–40 (1990)

Reddy J. N., An Introduction to the Finite Element Method, McGraw-Hill Mechanical Engineering, 3°ed, 2005

Scheider, I., Brocks, W.: Simulation of cup-cone fracture using the cohesive model. Eng. Fract. Mech. 70, 1943–1962 (2003)

Schwalbe K-H et al., Guidelines for Applying Cohesive Models to the Damage Behaviour of Engineering Materials and Structures, Springer Briefs in Applied Sciences and Technology, DOI: 10.1007/978-3-642-29494-5_2, The Author(s) 2013

Tvergaard V, Hutchinson JW. Effect of T -stress on mode I crack growth resistance in a ductile solid. Int J Solids Struct, 1994; 31:823–33

Tvergaard V, Hutchinson JW. The relation between crack growth resistance and fracture process parameters in elastic–plastic solids. J Mech Phys Solids, 1992;40:1377–97

Tvergaard V, Hutchinson JW. Toughness of an interface along a thin ductile layer joining elastic solids. Philos Mag A, 1994; 70:641–56.

Tvergaard V. Resistance curves for mixed mode interface crack growth between dissimilar elastic–plastic solids. J Mech Phys Solids 2001; 49:2689–703

Tvergaard, V., Hutchinson, J.W.: The relation between crack growth resistance and fracture process parameters in elastic-plastic solids. J. Mech. Phys. Solids 40, 1377–1397 (1992)

Walter, R., Olesen, J.F.: Cohesive mixed mode fracture modelling and experiments. subm. to Eng. Fract. Mech. 75, 5163–5176 (2008)

Yuan, H., Lin, G., Cornec, A.: Verification of a cohesive zone model for ductile fracture. J. Eng. Mater. Technol. 118, 192–200 (1996)

Web Sites

[1] http://www.boeing.com/commercial/787/#/gallery

[1] www.boeing.com

[2] http://www.airbus.com/galleries/photo-gallery/photo-browse/9/photo-count/100/filter/a350-xwb-family/#open=galleries/photo-gallery/dg/idp/48724-a350xwb-msn2-take-off4/?backURL=galleries/photo-gallery/photo-browse/9/photo-count/100/filter/a350-xwb-family/

[2] www.airbus.com

[3] http://winncad.blogspot.it/2010/12/airbus-starts-fabricating-first.html

[4] https://www.easa.europa.eu/system/files/dfu/Annex%20II%20-%20AMC%2020-29.pdf

[5] https://www.easa.europa.eu/system/files/dfu/ws_prod-g-doc-Events-2009-jan-090128-AMC20-29-Revision-Intent---Introduction.pdf

[6] https://www.easa.europa.eu/

[7] http://spacenews.com/vega-prime-contractor-avio-expects-to-find-strategic-owner-this-year/

[8] http://composites.usc.edu/projects/automated-defect-evaluation-software-for-ultrasonic-ndi.htm

[9] http://www.tudelft.nl/en/

[10] http://www.nlr.org/

[11] http://www.epicos.com/EPCompanyProfileWeb/GeneralInformation.aspx?id=15644

[12] https://www.corrosionpedia.com

[13] http://www.a350xwb.com/

[14] http://aviation.stackexchange.com/questions/12958/what-materials-make-up-most-of-the-weight-of-an-aircraft

[15] http://www.compositesworld.com

[16] http://www.dtic.mil/dtic/tr/fulltext/u2/a476134.pdf

[17] http://project.nlr.nl/bopacs/

[18] http://www.lockheedmartin.com/us/aeronautics.html

[19] http://www.hexcel.com/Resources/DataSheets/Prepreg-Data-Sheets/M21_global.pdf

[20] http://www.hexcel.com/resources/datasheets/carbon-fiber-data-sheets/IMA.pdf

[21] http://www.hexcel.com/resources/datasheets/brochure-data-sheets/prepreg_technology.pdf
[22] http://www.hexcel.com/products/aerospace/aprepregs
[23] http://www.hexcel.com:82/pdf/Product%20Selector%20Guides/Aerospace_SelectorGuide/index.html#?page=2
[24] www.Hexcel.com
[25] http://www.compositesworld.com/articles/panelized-option-attested-early-on
[26] http://www.hexcel.com/Resources/DataSheets/Prepreg-Data-Sheets/3501-6_eu.pdf